MICROCOPY RESOLUTION TEST CHART

LEVEL

AFOSR-TR- **AFOSR-TR- 81-0307**

MULTINOZZLE PLUME FLOWFIELDS

Final Report for Period 1 October 1975 - 15 October 1980

Author: Stanley Rudman

Prepared by
Research Department
Grumman Aerospace Corporation
Bethpage, New York 11714
RE - 618

Under Contract No. F44620-76-C-0021

Approved for Public Release Distribution Unlimited

Prepared for
AIR FORCE OFFICE OF SCIENTIFIC RESEARCH (AFSC)
Bolling Air Force Base
Washington, D.C. 20332

REPORT DOCUMENTATION PAGE	READ INSTRUCTIONS BEFORE COMPLETING FORM

1. REPORT NUMBER	2. GOVT ACCESSION NO.	3. RECIPIENT'S CATALOG NUMBER
AFOSR TR-81-0307	AD-A097 244	

4. TITLE (and Subtitle)	5. TYPE OF REPORT & PERIOD COVERED
MULTINOZZLE PLUME FLOWFIELDS.	FINAL rept. 1 Oct 75 — 15 Oct 80
	6. PERFORMING ORG. REPORT NUMBER

7. AUTHOR(s)	8. CONTRACT OR GRANT NUMBER(s)
STANLEY RUDMAN	F44620-76-C-0021

9. PERFORMING ORGANIZATION NAME AND ADDRESS	10. PROGRAM ELEMENT, PROJECT, TASK AREA & WORK UNIT NUMBERS
GRUMMAN AEROSPACE CORPORATION BETHPAGE, NY 11714	61102F 2308/A1

11. CONTROLLING OFFICE NAME AND ADDRESS	12. REPORT DATE
AIR FORCE OFFICE OF SCIENTIFIC RESEARCH/NA BOLLING AFB, DC 20332	1981
	13. NUMBER OF PAGES
	174

14. MONITORING AGENCY NAME & ADDRESS(if different from Controlling Office)	15. SECURITY CLASS. (of this report)
	UNCLASSIFIED
	15a. DECLASSIFICATION DOWNGRADING SCHEDULE

16. DISTRIBUTION STATEMENT (of this Report)

Approved for public release; distribution unlimited

17. DISTRIBUTION STATEMENT (of the abstract entered in Block 20, if different from Report)

18. SUPPLEMENTARY NOTES

19. KEY WORDS (Continue on reverse side if necessary and identify by block number)

FLUID MECHANICS	NUMERICAL TECHNIQUES
SUPERSONIC FLOWS	MACH DISC
SHOCK WAVES	
THREE DIMENSIONAL FLOWS	
EXHAUST PLUMES	

20. ABSTRACT (Continue on reverse side if necessary and identify by block number)

The a priori prediction of multinozzle rocket exhaust flow fields is addressed in detail. The requirements for accurate prediction of plume signature are derived and new quantitative relationships between optical signal and plume properties are derived. It is shown that, among a variety of requirements, plume models must include an accurate detailed description of the three dimensional near field of the multinozzle plume self impingement to achieve accuracy and reliability. The qualitative structure of these complex three dimensional flow fields is discussed. Several of the regulating flow process

DD FORM 1 JAN 73 1473

thus identified are three dimensional in nature and have no counterparts in classical two dimensional supersonic flow theory. One such process, the intersection of two three dimensional shock surfaces, is analyzed in detail and a qualitative account of the developing pattern is given. A three dimensional "floating fitted shock" numerical technique was devised for the first time. The computer code employs discrete discontinuities including plume boundary, shock surface and a complex singularity all which propagate through a fixed computational grid. The code was used successfully for the computation of the impingement of two uniform rectangular jets. A new analysis for the Mach disc flow field in an axisymmetric plume was derived. The basic interaction equation is solved numerically by the novel approach of first locating the sonic throat position and then integrating upstream. Test cases are presented which include viscous mixing for the first time. This new method provides the only calculation procedure capable of computing the subsonic streamtube downstream through and past the sonic singularity.

Accession For		
NTIS GRA&I	X	
DTIC TAB	☐	
Unannounced	☐	
Justification		
By		
Distribution/		
Availability Codes		
Dist	Avail and/or Special	
A		

AFOSR-TR-

MULTINOZZLE PLUME FLOWFIELDS

Final Report for Period 1 October 1975 - 15 October 1980

Author: Stanley Rudman

Prepared by
Research Department
Grumman Aerospace Corporation
Bethpage, New York 11714
RE - 618

Under Contract No. F44620-76-C-0021

Approved for Public Release Distribution Unlimited

Prepared for
AIR FORCE OFFICE OF SCIENTIFIC RESEARCH (AFSC)
Bolling Air Force Base
Washington, D.C. 20332

DTIC
ELECTED
S
D

D
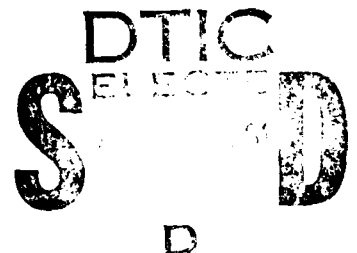
Approved by: Richard A. Scheuing
Director of Research

ACKNOWLEDGMENT

TABLE OF CONTENTS

SECTION 1
SUMMARY

The a priori prediction of multinozzle rocket exhaust flow fields is addressed in detail. The fundamental requirements for accurate prediction of plume IR signature are derived and new quantitative relationships between optical signal and plume properties are derived. It is shown that, among a variety of requirements, plume models must include an accurate detailed description of the three dimensional near field of the multinozzle plume self impingement to achieve the accuracy and reliabilty of the optical predictions, over the desired altitude range. The qualitative structure of these complex three dimensional flow fields is explained for the first time. Several of the regulating flow processes thus identified are three dimensional in nature and have no counterparts in classical two dimensional supersonic flow theory. One such process, the intersection of two three dimensional shock surfaces, is discussed in detail and a qualitative account of the developing pattern is given. A numerical procedure, "the floating fitted shock" technique, fit the requirements of accuracy and generality necessary for the computation of the multinozzle plume flow fields. This method is conceded to be the mosi desirable, albeit most complex, for the solution of supersonic flows. A computer code was devised which contained discrete discontinuities including slip surfaces, a shock surface and a complex sonic shock/centered expansion singular point based on a boundary point calculation which properly accounts for the three dimensional propagation of characteristics. The code was successful for simplified geometries but could not be increased in generality to handle the complete flow pattern. An analysis for the Mach disc flow field in an axisymmetric plume was derived which leads to a basic interaction equation. A numerical procedure for solving this equation along with the other governing one dimensional equation uses the novel approach of first locating the sonic throat position and then integrating the equations upstream. Several test cases are presented which include viscous mixing for the first time. This method should provide more reliable calculation procedure for these flow fields than now exists.

SECTION 2

INTRODUCTION

Detailed understanding of jet and rocket engine exhaust flow fields is required in a wide variety of Air Force space and missile programs. Predictions of infrared signature, radar cross section, electromagnetic wave attenuation, and production and dispersion of noxious pollutants are examples of the exhaust system properties which are fundamental in both conceptual systems studies and actual design and development programs. These exhaust properties are the subject of a broad area of study known as plume phenomology- a multidisciplinary study encompassing the sciences of fluid mechanics, chemical kinetics and optical radiative transport theory. Often system design requirements and programmatic study definitions require state of the art or perhaps beyond predictive capabilities in each of these disciplines to provide the desired information and definitions. This research program was aimed at extending the state of the art of fluid mechanical prediction techniques while keeping in mind how these advances would fit in the broader overall plume phenomology program.

Plume fluid mechanics is the underlying physical science in plume phenomology as the spatial distribution of thermochemical properties it defines provides the structure upon which chemical kinetics and subsequently radiative transport are predicted. The main area of interest was the fluid dynamics of multiple nozzle exhaust systems. This study was aimed at the inviscid structure of this flow as it forms the "skeleton" upon which is built the complete flow field including the turbulent (reacting) mixing layer and

viscous far field. This portion of the effort was therefore the study of inviscid three dimensional supersonic flow fields containing complex shock systems. Plume flow fields can contain Mach discs and hence regions of subsonic flow. Understanding and modelling of these phenomena was a second area of study.

The flow field created by the exhaust of a multiple nozzle exhaust system is a complex three dimensional flow. The inviscid flow defines the shock wave structure of a plume which is of prime importance in predicting plume observables. The shock waves are responsible for both local sharp increases in temperature and pressure and far field temperature increments. The far field effect is a product of the entropy rise (total pressure loss), associated with the shock waves, which persists downstream showing up there as an increment in temperature above the isentropic far field temperature. Both optical radiation and chemical kinetic processes are governed by equations all of which contain "Arrhenius" type exponential factors [$\exp(-B/T)$]. In the case of optical radiation B is the second radiation constant divided by the wavelength. The "characteristic" temperature B of these processes is generally high so that chemical activity and radiative source terms are most prominant in regions of high temperature. In cases where B is much larger than the maximum temperature the regions of high chemical reaction or radiative emission reduce to extremely thin sheets. Thus the shock wave structure which is the primary factor in determining both local and far field temperature levels is a central determining factor in chemical activity and optical radiation. For example, it is clear from many axisymmetric flow field studies (c.f. Ref. 2-1) that shock structure and peaks in plume IR station radiation are highly correlated. In Ref. 2-2 the central role of far field

temperature on plume radiation was demonstrated clearly. It is for these reasons that detailed predictive capabilities of the three dimensional flow and shock structure were sought for the multiple nozzle flows.

The pursuit of solutions to the three dimensional plume flow fields requires the numerical solution of the Euler Equations. For supersonic flows these are a set of hyperbolic partial differential equations which forms an initial value problem. These problems are suited (in theory) to straight forward marching numerical solution techniques. Experimental evidence (Ref. 2-3) showed that there were at least three and most probably more shock wave configurations possible for twin nozzle flow fields. The specific configuation being determined by individual nozzle exit properties, nozzle spacing and background pressure and flow properties. The full diversity of flow configurations possible may be very broad and include many configurations not yet observed. For two reasons it was deemed desirable to seek numerical solutions of these flow fields in which the shock waves were "fitted". That is, in the calculation procedure the shock wave surfaces are considered to be discrete discontinuous surfaces which are tracked as part of the solution. The first reason derives from the discussion in the previous paragraph. Optical and radiative transport equations are extemely sensitive to temperature so that the most accurate temperature predictions are desireable. Secondly, the alternative approach "shock capturing" produces a shock wave in a two dimensional flow that is portrayed in the solution as a dispersed compression spread over three to five mesh intervals. There are generally overshoots and undershoots involved in the flow quantities and the solution in

the neighborhood of the shock wave is therefore unreliable and contains order unity inaccuracy. The multinozzle plume is a three dimensional flow containing shock intersections which would likewise have five by five mesh regions of questionable accuracy. Therefore it appears that with the complex shock structure that exists in the subject flow "shock capturing" would produce results that either (1) had an inordinate percentage of mesh points inaccurate because of nearby shocks or shock intersections or (2) required an inordinate number of mesh points to cirmcumvent this problem.

The only previous complex three dimensional calculations (Ref. 2-4) employing fitted shock waves was for space shuttle type configurations in which the general shape and topology of the shock pattern is known. In that case very elegant and precise mapping techniques were brought to bear on the problem to simplify the computer program logic. Since the shock wave surface configurations for the multinozzle plume flow fields is not known precisely and can take on any one of a number of general configurations a more general numerical technique was pursued. This is referred to as the floating "fitted" shock wave technique and, in fact, employed floating discontinuties and singularities more general than shock waves. In this method (cf. Moretti Ref. 2-5) the shock wave surfaces are not mapped to the boundaries of computational domains, rather they are permitted to traverse a relatively stationary computational grid. In theory the scheme does not require a priori knowledge of the shock wave configuration and so would be ideal for the problem at hand. The price for this generality is very heavy and two fold. First the computer logic is extremely complex as it must anticipate a large number of geometrical configurations and combination of configurations. And,

secondly, the details of the three dimensional phenomenon must be understood so that local solutions can be incorporated into the flow field. For example, in this "fitted singularity" approach the exact local solution for the shock intersection with the plume boundary was incorporated in the solution. The exact details of the reflected Prandtl Meyer expansion wave and sonic nature of the impinging shock are employed in a special cell calculation. This singular point was free to traverse the computational mesh as the solution progressed and pass from one cell to the next. In this way the calculation procedure is similar to finite element methods with the added feature that the cell containing this singularity changes automatically as the shock moves and the calculation proceeds. Unfortunately there are several other singularities which are not presently understood that must be modelled to accurately predict the three dimensional flow fields. One of these occurs when two three dimensional shock surfaces intersect and subsequently develop into an irregular reflection. This problem was studied theoretically and a qualitative description of the flow field development was derived employing hodograph techiques.

The solution of plume flow fields with Mach discs open up an entirely new set of requirements for numerical calculations and theoretical assessment. The exhaust gas flow fields, aside from regions downstream of Mach discs, are supersonic and as such are governed by hyperbolic partial differential equations. These equations have solutions which at any point can be expressed solely on the basis of flow properties upstream of that point. Therefore, the numerical solution of these equations proceeds, at least in principle, by a step by step or marching procedure. The flow downstream of Mach discs on the

other hand is subsonic and as such is governed by elliptic partial differential equations. The solution to these equations at any point depends on the solution at all neighboring points both upstream and downstream. Thus the solution at any specific point is related to all the boundary values of the flow properties surrounding the subsonic region. The plume containing a Mach disc is thus a mixed type flow containing regions of both subsonic and supersonic flow that is similar in many ways to more familiar transonic flows. These flows are computed numerically by overall relaxation schemes (cf. Ref. 2-6.).

The Mach disc flow field has a critical property that was exploited by Abbett (Ref. 2-7) to explain the determining factor for the shock triple point location. He observed that the flow which passes through the normal shock portion of the Mach disc is subsequently accelerated downstream to supersonic velocities. This subsonic/supersonic stream tube is analogous to a De Laval nozzle with a choking or saddle point singularity condition at the throat. The location of the Mach disc itself is determined as that position which is compatible with a smooth acceleration through the sonic singularity. An important approximation which greatly simplifies the solution of plumes with Mach discs was given by Abbett (Ref. 2-7) and later employed by Salas (Ref 2-8). The subsonic portion of the flow field is approximated using one dimensional flow analysis. The location of the Mach disc is estimated and the subsequent supersonic outer flow and subsonic one dimensional flow is calculated. The unique solution is determined by finding the location of the Mach disc which results in sonic velocity occurring at the same point as the minimum area. Several possible Mach disc locations are employed to iterate

2-6

and determine a bracket for the possible location of the Mach disc. This method has been used (Salas Ref.2-8) with success in the past to determine a range of plume flow fields with Mach discs. However, the method has several drawbacks. It does not provide any theoretical explanation of the relationship of the solution to overall flow properties, it does not include viscous effects, and it has questionable numerical reliability.

The forward integration of the subsonic equations is a tricky procedure at best and is questionable. The set of equations governing the subsonic streamtube has a positive eigenvalue. Thus it possesses exponentially growing solutions (unstable). Compounding this fact, the exponential factor is proportional to $(1 - M^2)^{-1}$ so that as the sonic singularity is approached forward marching numerical procedures become useless. In view of the rapid changes in the solution near the throat a compromise must be struck between accuracy and the ability to generate solutions at all. In the present work a solution procedure is developed which resolves this dilemma. In the inviscid case the sonic throat location is determined first and then the equations are solved by integration in the upstream direction.

The analysis which is developed leads to a central governing interaction equation. This equation coupled with the familiar one dimensional flow equations and the supersonic flow equations for the outer plume stream help to delineate the underlying processes driving the solution. The strong interaction between the subsonic flow which passed through the normal shock portion of the Mach disc and the supersonic flow which passed through the oblique shock is evident through a term which is related to the Reimann invariant on the downward running characteristics. Thus the explicit effect

of the plume outer boundary properties on the Mach disc solution is made clear for the first time. In addition viscous mixing between the two streams is incorporated into the analysis via a simple one dimensional analysis. In the inviscid case determination of the exact location of the sonic throat is possible based on an estimated supersonic flow and an assumed location of the shock triple point. In the viscous case a further iteration is necessary.

In the following section a qualitative analysis of the multinozzle plume flow field is discussed. The various three dimensional features of the flow are pointed out in the context of the overall flow structure. Section 4 reviews the relationship between the plume fluid/thermochemical distributions and the resulting IR signature. The mathematical relationship between optical emission and flow properties is derived. In Section 5 the floating fitted shock numerical technique is outlined and the three dimensional boundary point calculation is described. A sample calculation for a simplified geometry is presented. Section 6 presents the study of the intersection of two three dimensional shock surfaces. Section 7 briefly describes an alternate new method for finite difference calculations which might reduce the enormous logic load on the fitted discontinuity programs. Section 8 contains the discussion, analysis and numerical computations for the Mach disc flow.

REFERENCES

2-1   Slack, M., Del Guidice, P., Ambruso, R., Reed, R., Ludwig, C., Malkmus W., Freeman G.M., "Plume Data Analysis of Advanced Propellants, Final Report ".Grumman Research Dept., RE-580 Oct. 1979.

2-2   Sukanek, P.G., "Matched Pressure Properties of Low Altitude Plumes," AIAA Journal, December 1977.

2-3   Wurster, W.H. and Murrone, P.V., Calspan Corp., private communication.

2-4   Marconi, F., Salas, M., Yaejer, L., "Development of a Computer Code for Calculating the Steady Super/Hypersonic Inviscid Flow Around Real Configurations," NASA CR-2675, April 1976.

2-5   Moretti, G., "Floating Shock Fitting Technique for Imbedded Shocks in Unsteady Multidimensional Flow," Proceedings of the 1974 Heat Transfer and Fluid Mechanics Institute, Stanford University Press, 1974.

2-6   Jameson, A., "Numerical Computation of Transonic Flows with Shock Waves", *Symposium Transsonicum II*, Gottingen , Sept. 1975, Springer Verlag, 1976, pp. 384-414.

2-7   Abbett, M. "The Mach Disc in Underexpanded Exhaust Plumes, " AIAA Paper No. 70-231, Jan 1970.

2-8   Salas, M., "The Numerical Calculation of Inviscid Plume Flow Fields," AIAA 7th Fluid and Plasma Dynamics Conference, AIAA Paper No. 74-212, June 17-19, 1974.

SECTION 3

STRUCTURE OF MULTINOZZLE PLUME FLOW FIELDS

The structure of the multinozzle plume flow is dominated by complex three dimensional flow phenomenon. These processes are not simply the extension of familiar two dimensional supersonic flow situations into a third dimension. Rather they are new and peculiar to three dimensional flows and as such are basically unknown to analysts. Therefore the ability to accurately model and devise numerical schemes and their associated computer codes rests heavily on first developing some understanding in these areas. There are two basic situations that can be identified. The first and most striking is the problem of the intersection of three dimensional shock wave surfaces. The multinozzle plume flow field contains several shock wave surfaces and these invariably intersect. The subsequent development of the shock pattern is complex and will be discussed in detail in a later section. Another situation peculiar to three dimensional flows occurs when there is an abrupt change in geometry or topology in the flow (i.e. transition of a shock reflection from a regular reflection to a Mach reflection). This brings about an initialization problem which is analogous to the flow at the leading edge of a wedge or the point of a cone. These latter two are well known two dimensional supersonic flow situations which have cataloged solutions. We call on our knowledge of these catalogs to initialize or reinitialize two dimensional (or axisymmetric) flow fields when there is an abrupt change in geometry (wall angle). These catalogs do not exist in three dimensional flows. Beyond that the nature of the solution is not known in any of these situations.

In order to study the structure of the multinozzle plume flow field the structure of the individual undisturbed exhaust plumes is first examined. Each exhaust plume is axisymmetric and underexpanded. Figure 3-1 is a schematic of one of these plumes. Supersonic exhaust flow leaves the rocket nozzle at the exhaust plane. The ambient pressure at the exit plane is lower than the exhaust plane pressure and the exhaust flow expands at the nozzle lip so that the pressures of exhaust and ambient gases are matched along the plume interface. The barrel shock forms in the single nozzle plume because expansion waves (upward running characteristics) in the flow reflect from the (near) constant pressure plume interface resulting in reflected compression waves. These eventually focus to start shock system (B1)(see Fig. 3-1(a)). The expansion waves which start this process can arise in the conical like source flow leaving the nozzle, however, even a uniform parallel exit flow nozzle will produce the same result. The upward running characteristics leaving the exit plane become expansion waves as they cross the Prandtl Meyer expansion fan at the nozzle lip because the flow is axisymmetric and spreading laterally. The axisymmetric nature of the flow causes the wave strength of the B1 shock, Figure 3-1(b), to increase as it progresses downstream and approaches the axis of the plume. A Mach disc and reflected shock system (B2) develop downstream of the original barrel shock B1. The flow behind the Mach disc is subsonic so that the location of the disc depends on the pressure distribution and mixing processes downstream of it. Section 7 will discuss this portion of the flow field in detail. This is in distinction to the remainder of the flow which is supersonic and where there is no upstream influence. This inviscid flow pattern is well understood and several computer

BARREL SHOCK

- - - - UPWARD RUNNING CHARACTERISTICS

—— DOWNWARD RUNNING CHARACTERISTICS

p_a

p_e

$p_e > p_a$

(A) DETAILS NEAR NOZZLE EXIT

REFLECTED COMPRESSION WAVE

PLUME BOUNDARY

EXPANSION WAVE

B1

B2

SUBSONIC CORE

NOZZLE EXIT
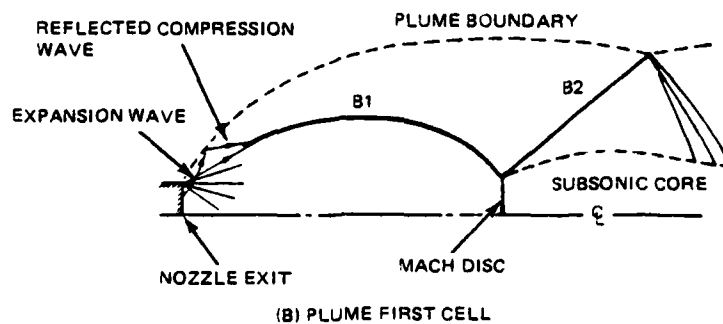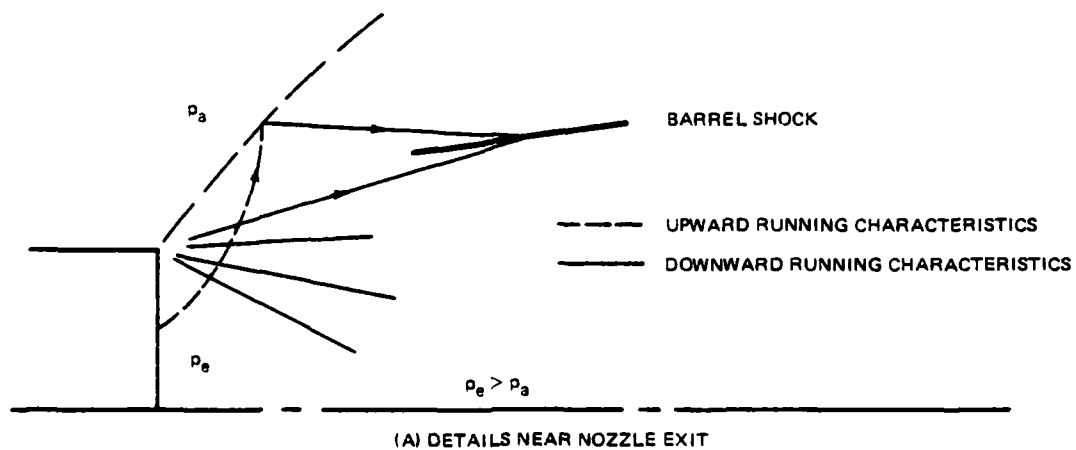
MACH DISC

(B) PLUME FIRST CELL

2193-001D

Fig. 3-1 Single Axisymmetric Plume Flow Field

codes are available (in varying degrees of approximation) to predict it (Ref. 3-1, 3-2).

It is quite informative to investigate the nature of the impingement of two uniform jets before considering the complete problem of the impingement of two underexpanded plumes. This flow pattern, outlined schematically in Figure 3-2 is expected to have two shock wave systems. The impingement shock (I) and the recompression shock R. In the side view the I shock appears basically as expected from a two dimensional pattern. The impingement shock turns the oncoming flow parallel to the symmetry plane. A complex process takes place at the intersection of the plume boundary and the I shock. Based on work by Hunt and coworkers (Ref. 3-3, 3-4, 3-5) the discontinuous boundary pattern sketched in Fig. 3-2 is expected. These references deal with normal impingement of uniform jets; however, the interaction of the I shock and the plume boundary is locally equivalent to that when viewed in a coordinate system parallel to the shock/boundary intersection. The flow field is projected onto a plane perpendicular to the intersection line (Fig. 3-2(b)). The component of velocity parallel to the intersection line is constant in the neighborhood of the intersection line because (a) it is parallel to the shock wave and is hence unaltered by it and (b) is locally parallel to the plume boundary both upstream and downstream of the impingement shock. The pressure at points A and D are matched. Downstream of the impingement shock the pressure at B is greater than at A and therefore greater than at D. Therefore, an expansion fan emanates from the plume boundary at the point of impingement to cancel the pressure rise due to the I shock wave (Station 1, Figure 3-2(a)). The required pressure match downstream of the shock demands
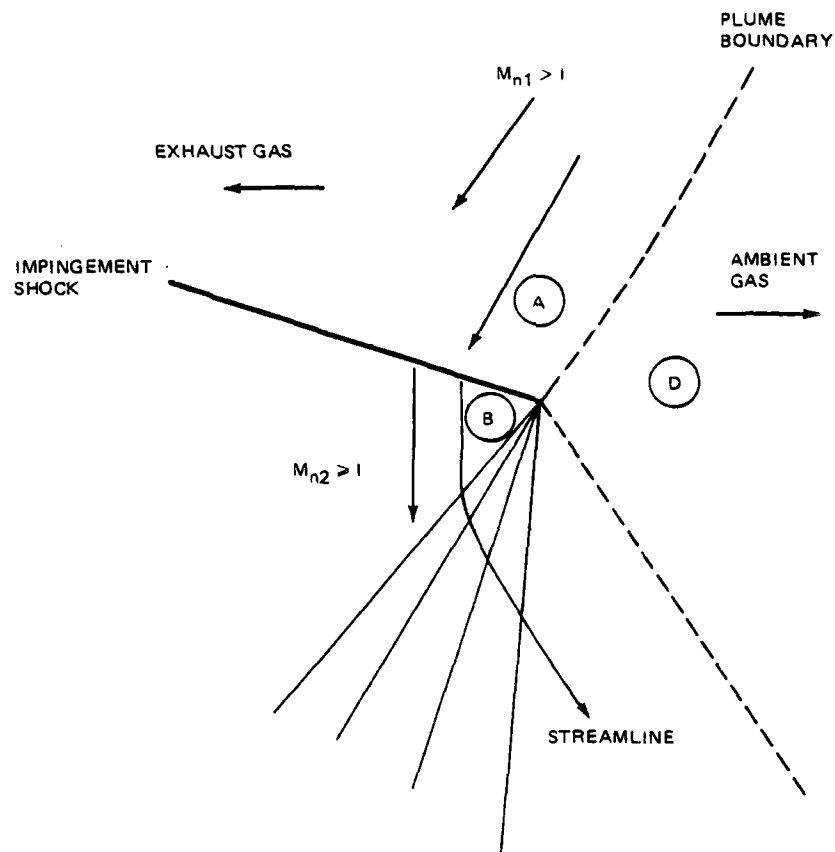
3-4

CROSS-SECTIONS

$M > 1$

R

SYMMETRY PLANE

0 1 2 3 4 5

SIDE VIEW
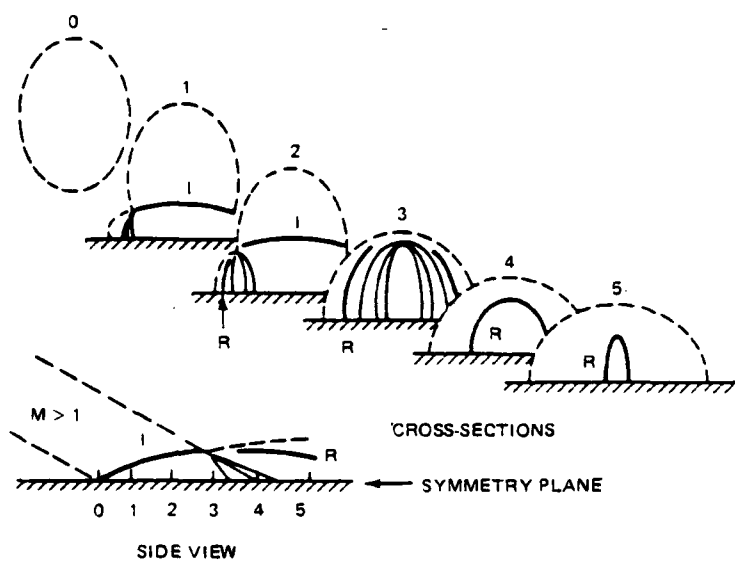
(A) ISOMETRIC AND SIZE VIEW OF OVERALL FLOW

2193-002D(1/3)

Fig. 3-2 Schematic Flow Field for the Impingement of Two Uniform Plumes (Sheet 1 of 3)

BOUNDARY

PLUME
BOUNDARY

$M_{n1} > 1$

EXHAUST GAS

IMPINGEMENT
SHOCK

AMBIENT
GAS

A

D

B

$M_{n2} > 1$

STREAMLINE

PROJECTION OF PLUME FLOW FIELD IN A PLANE PERPENDICULAR
TO THE INTERSECTION LINE

(B) DETAIL OF THE FLOW PATTERN AT THE INTERSECTION OF THE
IMPINGEMENT SHOCK AND PLUME

2193-002D(2/3)

Fig. 3-2 Schematic Flow Field for the Impingement of Two Uniform Plumes (Sheet 2 of 3)

that at the point of impingement there is at least sonic velocity, relative to the intersection line, to support a Prandtl Meyer fan. At Station 2, a new feature develops in the flow-expansion wave fronts stretching in three dimensions interact with the constant pressure boundary giving rise to inward moving compression wave surfaces that coalesce to form a recompression (R) shock system. A schematic of this detail is shown in Fig. 3-2 (c). This coalescence is completely analogous to the formation of the barrel shock (B) system in the axisymmetric case. Subsequently, (Station 3-5) the R shock system shrinks in size and grows in strength as it approaches the plume center. Another way of viewing the overall impingement process is to consider that the impingement shock by elevating the pressure of a perfectly matched plume creates an underexpanded jet which subsequently expands laterally giving rise to the shock pattern familiar to underexpanded plumes.

The flow pattern associated with the impingement of two underexpanded plumes, in general, contains all three shock systems: the barrel shock, the impingement shock and the recompression shock. These shock surfaces propagate across the plume flow fields, interact and give rise to subsequent generations of shock surfaces. It becomes harder and harder to identify each shock specifically in succeeding generations. Many shock configurations are possible depending on the relative strengths of the three systems and the order in which they intersect. Three observed configurations will be discussed. Each flow schematic is followed by a corresponding glow photograph (Ref. 3-6).

In the weakest type interaction (Fig. 3-3) the flow pattern is initially that of two individual plumes. At distances less than the first Mach discs
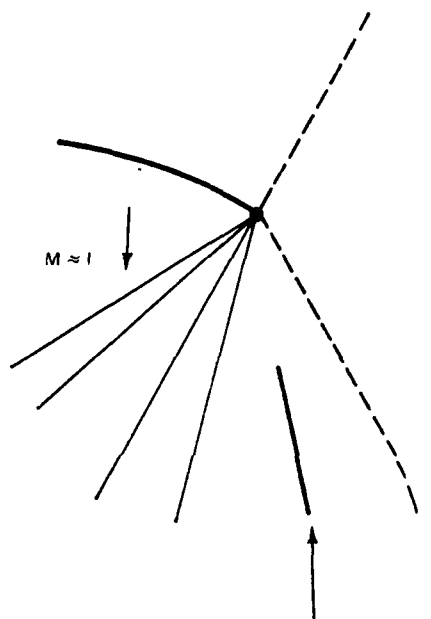
RECOMPRESSION SHOCK

PROJECTION OF PLUME FLOW FIELD ON PLANE PERPENDICULAR
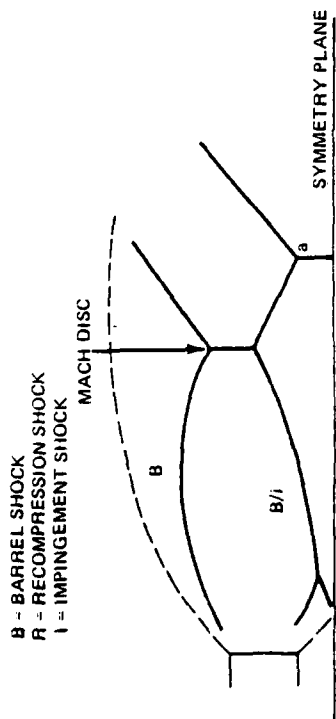TO INTERSECTION LINE
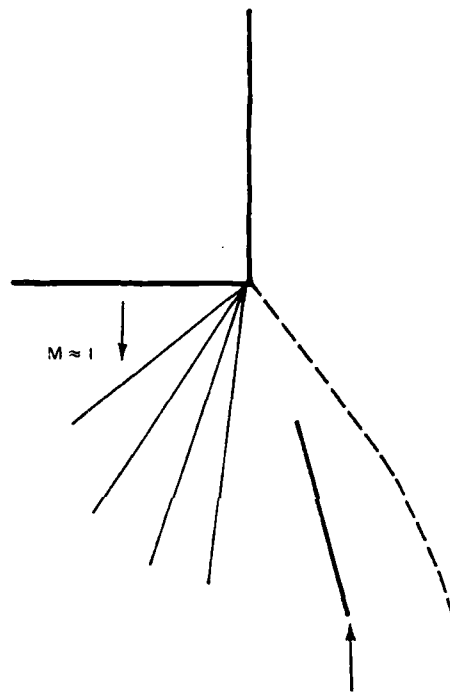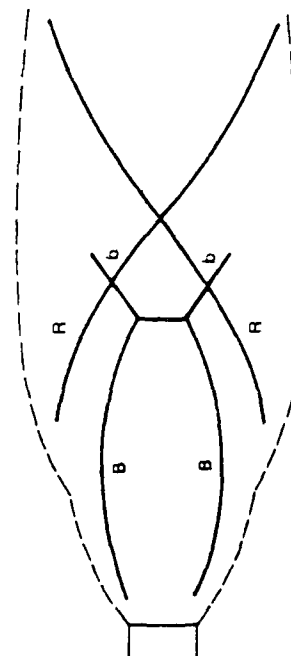
BARREL SHOCK

EQUIVALENT NOZZLE EXHAUST FLOW

(C) DETAIL SHOWING THE FORMATION OF THE RECOMPRESSION SHOCK

2193-002D(3/3)

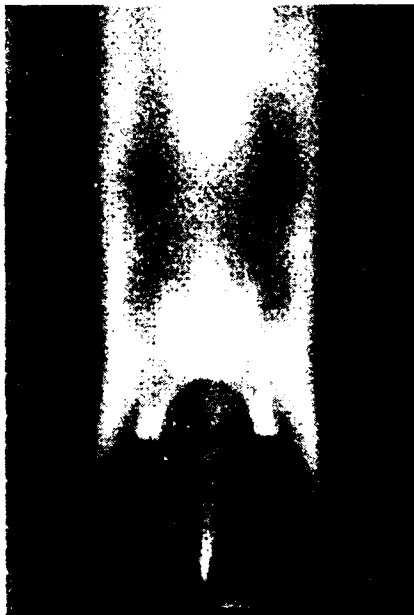Fig. 3-2 Schematic Flow Field for the Impingement of Two Uniform Plumes (Sheet 3 of 3)
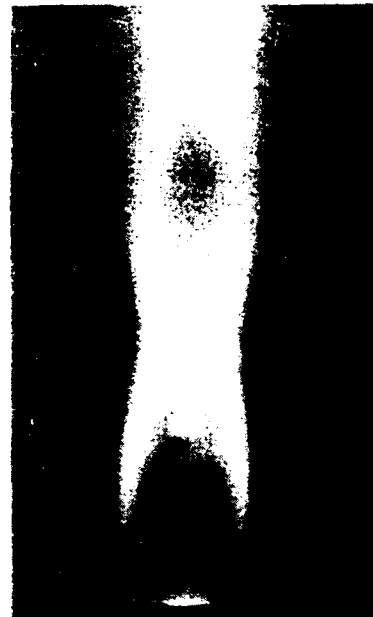
TOP VIEW

SIDE VIEW

B) GLOW PHOTOGRAPHS

B – BARREL SHOCK
R – RECOMPRESSION SHOCK
I – IMPINGEMENT SHOCK

SYMMETRY PLANE

MACH DISC

B

B/i

a

TOP VIEW

R

R

b

b

B

B

SIDE VIEW

A) SCHEMATIC

2193-003D
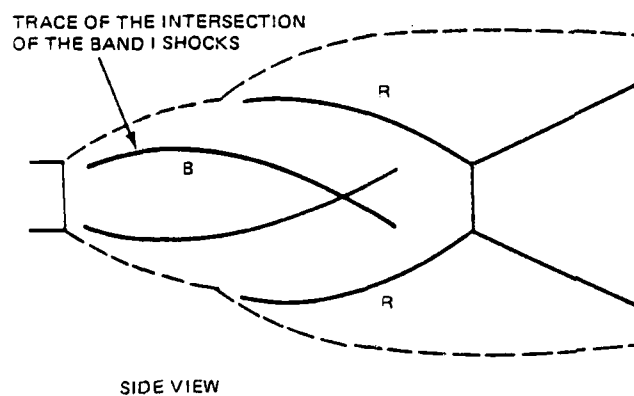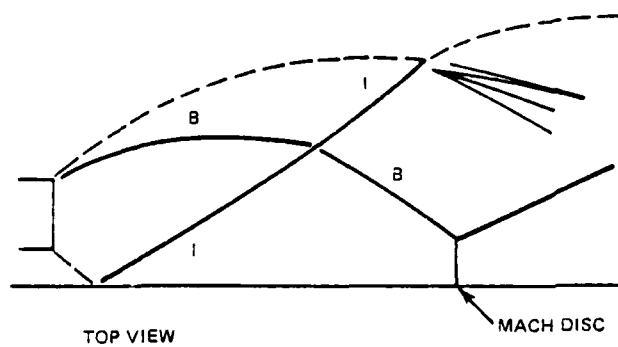
Fig. 3-3 Flow Pattern Underexpanded Twin Plumes, Weak Interaction

the plumes appear almost as two individual plumes in the top view. The first Mach cell is only slightly distorted by the I shock (see top view). In the top view the impingement shock seems to merge with the barrel shock and deflect so that the Mach discs are not quite normal to the nozzle centerline. The next major shock pattern occurs downstream of the Mach discs in the central portion of the flow between the exit of the two nozzles. The R shocks (side view, Fig. 3-3) from the upper and lower portion of the flow intersect to form a wedge shaped shock pattern in the flow. The leading edge of this system is cut off (point a in top view of Figure 3-3) as it is intersected by the reflected barrel shock downstream of the Mach disc. The small features adjacent to this central pattern (see top view of glow photograph Figure 3-3) seems to be created at the intersection of the reflected barrel shock and the recompression shock at point b shown in the side view of Figure 3-3.

At lower background pressures the initial expansion at the nozzle lip is greater and the plumes impinge at higher angles increasing the strength of the impingement shock. Figure 3-4 is an example of a moderate interaction where the impingement shock strength is increased to the point where it cuts off the barrel shock system before the formation of the Mach disc associated purely with the barrel shock. In this case downstream of the B/R intersection (top view) the R and transmitted B shock intersect in such a way as to create a normal shock (Mach disc) in the center of the flow. In the strong interaction case (Fig. 3-5) the impingement shock rapidly traverses the plume and diverts the B shock sharply toward the symmetry plane. This transmitted B shock reaches the symmetry plane (top view) at point a while the R shock (side view) is still out near the plume boundary. As the B shock system reflects from the

TOP VIEW

MACH DISC

TOP VIEW

TRACE OF THE INTERSECTION
OF THE BAND I SHOCKS

SIDE VIEW

SIDE VIEW
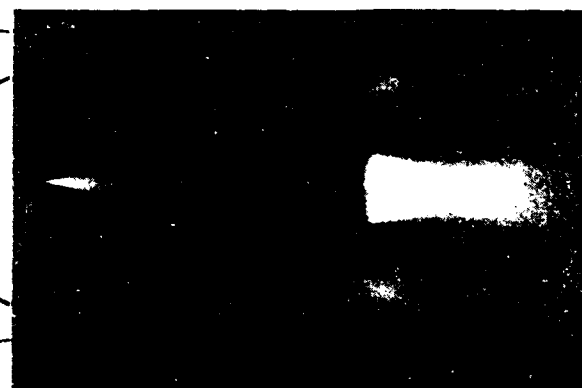
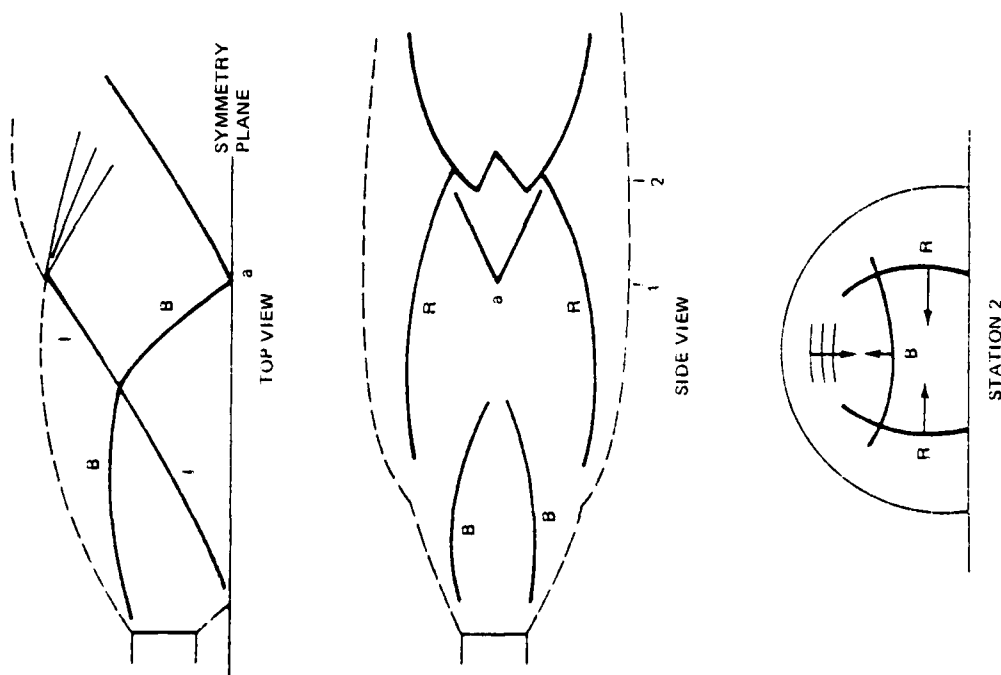A) SCHEMATIC
2193-004D

B) GLOW PHOTOGRAPHS

Fig. 3-4 Flow Pattern of Underexpanded Twin Plumes, Intermediate Interaction

TOP VIEW

SIDE VIEW

B) GLOW PHOTOGRAPHS

SYMMETRY PLANE

TOP VIEW

SIDE VIEW

STATION 2
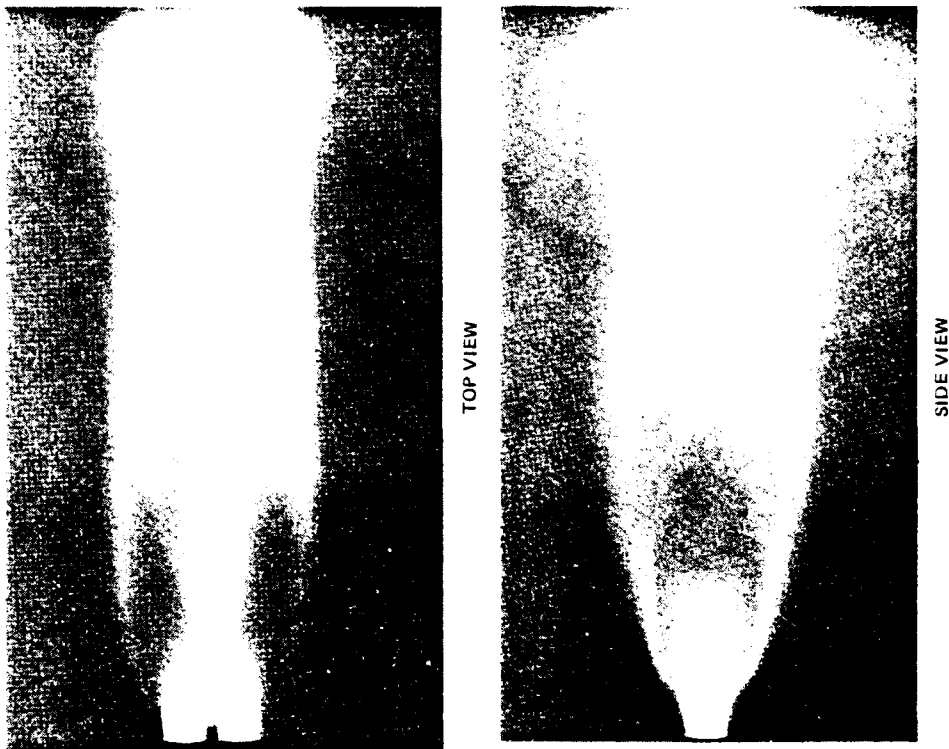
a) SCHEMATIC

2193-005D

Fig. 3-5 Flow Pattern Underexpanded Twin Plumes, Strong Interaction

symmetry plane a V shaped trace is created in the side view (Fig. 3-5). Subsequently this reflected B shock intersects with the R shock surfaces producing an irregularly shaped leading edge because both these shock surfaces are not planar (Fig. 3-5, station 2).

The three basic flow patterns described most probably represent only a fraction of the possible flow configurations. There are likely many variations of these patterns and others not yet observed. For this reason any computational scheme chosen to pursue solutions of these flow fields cannot be of the type that is constrained by geometrical and/or topological limitations. The scheme must allow for a wide variety of geometrical patterns and must be flexible enough to include as yet unknown and unanticipated configurations. A computational technique satisfying this constraint is discussed in the Section 5. The method produces accuracy and maintains efficiency by incorporating detailed local flow solutions wherever possible. Thus shock waves and slip surfaces are portrayed as discontinuties which are tracked individually and locally satisfy the appropriate jump conditions. There are other three dimensional flow features in these plumes that must likewise be modelled in the small by their local solutions. Two such solutions required for the multinozzle plume flow field have not been analyzed in the past. A discussion of the nature of the lift off of the impingement shock and the transition of the regular reflection to a Mach reflection process in the intersection of two three dimensional shock surfaces is presented in Section 6.

REFERENCES

3-1   Salas, M., "The Numerical Calculation of Inviscid Plume Flow Fields," AIAA 7th Fluid and Plasma Dynamics Conference, AIAA Paper No. 74-323, June 17-19, 1974.

3-2   Abbett, M., "The Mach Disc in Underexpanded Exhaust Plumes," AIAA Paper No. 70-231, Jan. 1970.

3-3   Hunt, B.L., "Waves Near a Sonic Line in Nonhomentropic Flow," Aeronautical Quarterly, February, 1972.

3-4   Gummer, J.H. and Hunt, B.L., "The Impingement of a Uniform, Axisymmetric, Supersonic Jet on a Perpendicular Flat Plate," Aeronautical Quarterly, November, 1971.

3-5   Carling J.C. and Hunt, B.L., "The Near Wall Jet of a Normally Impinging Uniform, Axisymmetric, Supersonic Jet," Journal of of Fluid Mechanics, Vol. 66, Part 1, 1974.

3-6   Wurster, W.H. and Murrone, P.V., Calspan Corp., private communication.

SECTION 4

## RELATIONSHIP OF IR SIGNATURE TO PLUME PROPERTIES

There is a variety of programs which require knowledge of rocket plume flow fields. Detailed spatial maps of exhaust temperatures, pressures and chemical species concentrations are required as input in electromagnetic attenuation codes, aircraft or spacecraft impingement analysis and IR emission codes for both heat transfer and optical signature evaluations. These calculations are often so expensive to perform that parametric analysis or calculation of a large member of data sets is out of reach. For that reason it is difficult to answer questions pertaining to the variation of plume IR signature as a result of systematically changing the many input parameters. Normal system design procedures become extremely costly or have to be bypassed. The main concern in this section of the study was the effect of multinozzle plume flow fields on the IR signature of a missile. The results were presented in detail in Ref. 4-1 and will be reviewed briefly here. Analytic formulas were derived which relate IR signals to various plume properties thus alleviating to some extent the problems in parametric analysis. These relationships point out the allowable errors or uncertainties in plume models that lead to desired levels of accuracy in overall IR predictions. It was determined that there are several other processes besides multinozzle plume impingement that must be properly accounted for if accurate IR predictions are to be achieved over the entire altitude range . The analysis is best suited for optically thin plumes, however, as in other situations the conclusions will probably have a much broader range of applicability.

The underlying source term in all optical radiation calculations is the Planck Black Body Function. The radiant emission from elemental gaseous sources is proportional to the product of that function and the absorption coefficient of the IR active molecule. The magnitude of the Planck function is sensitive to temperature and becomes increasingly so as the temperature decreases. This sensitivity is greater the shorter the wavelength as shown in Fig. 4-1 where the logarithm (base 10) of the Planck function multiplied by λ^5 is plotted versus temperature. Temperature sensitivity is graphically depicted in Fig. 4-2 where the temperature increment necessary to produce an increase in the Planck function by a ratio of 2.71, 1.65, and 1.28 (e, $e^{1/2}$, $e^{1/4}$) is shown for the range 400-2000 K. In Fig. 4-2a, for example, for 2.7 microns at 1000 K, a temperature increment of 100 K produces an increase in the Planck function by a factor 1.65; at 2000 K, the same increase requires a temperature increment of 380 K. In fact, the same accuracy at 800 K requires a temperature accuracy of 60 K. Figures 4-2b and 4-2c show the temperature sensitivity for shorter and longer wavelengths, and, as before, the decreasing sensitivity with increasing wavelength is shown. Below the abscissa in Fig. 4-2a there is an approximate altitude corresponding to the temperature axis. This correspondence is approximate but serves as a reasonable guide. It is interesting to note that uncertainties, errors in calculation or variations in any plume parameter that lead to temperature increments have much less of an effect at low altitudes. Thus a change in temperature at sea level of 400 K (all other quantities fixed) would only produce a change of the Planck function by a factor of 1.65. On the other hand at 50 km altitude there is a factor of 2.71 for only 150 K variation. This critical temperature dependence

4-2
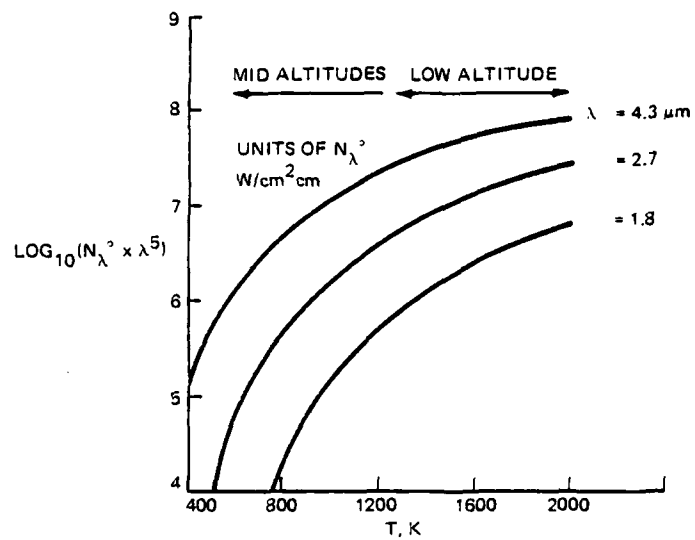
Fig. 4-1 Planck Black Body Function Variation with Temperature
for Several IR Wave-lengths

2193-006D
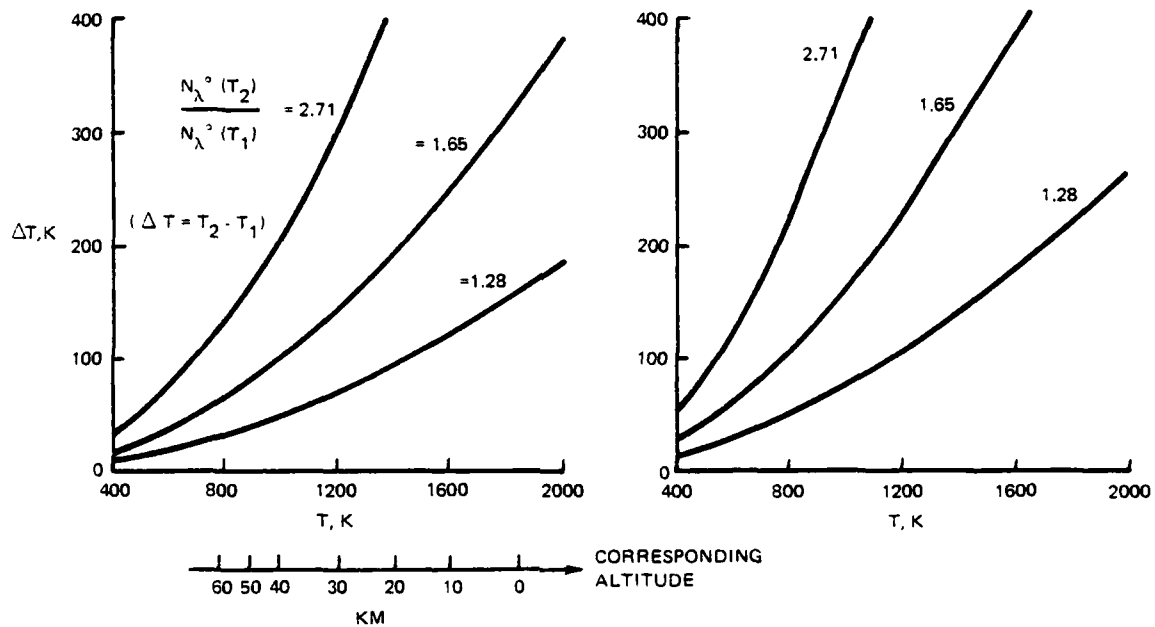
(a) $\lambda = 2.7\ \mu m$

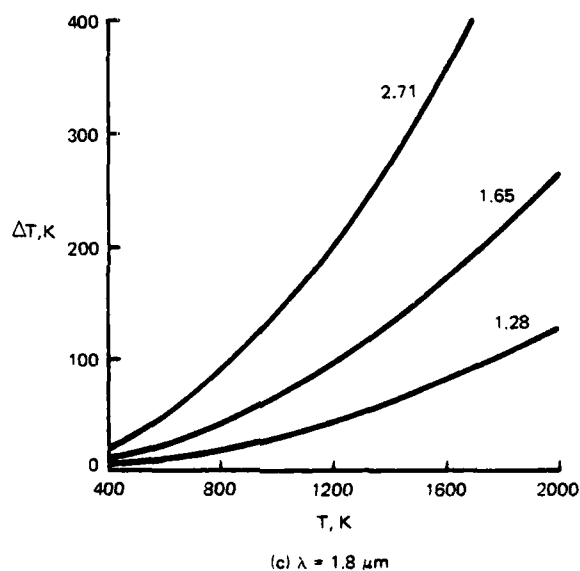(b) $\lambda = 4.3\ \mu m$

(c) $\lambda = 1.8\ \mu m$

Fig. 4-2. Temperature Increment Necessary to Produce an Increase in the Planck Function of 2.71, 1.65, 1.28 as a Function of Temperature

requires plume models to have very tight controls on the approximations involved in the prediction of plume temperature levels in order to achieve accuracy over the entire altitude range.

A variety of processes control the temperature levels in the plume gases; expansion to background pressure, turbulent mixing of the exhaust and ambient gases, and afterburning chemistry in the mixing between the exhaust gas and ambient stream. The mixing process is of direct concern because it: adds a temperature increment due to viscous dissipation and controls the geometric size of the radiating region. At low altitudes, an equally important contribution to the radiation levels is the afterburning chemistry, which not only adds a temperature increment, but can also be responsible for the consumption or production of a radiating species. The influence of both mixing and afterburning has been the target of other studies and will not be focussed on here. The inviscid expansion process of the exhaust gas to the ambient pressure levels becomes more and more significant as altitude increases. There are two principle processes that cause major changes to the temperature that would be achieved via an isentropic inviscid expansion from the nozzle exit to the background pressure. The primary deviation is due to shock waves in the plume flow which cause large entropy increases that persist into the plume far field. These shock waves result from the adjustment of the underexpanded nozzle flow to the local pressure of the surrounding fluid and the impingement of individual exhaust plumes on each other in the case where the vehicle has more than a single engine. The former case is well understood because it is an axisymmetric flow, while the latter is a complex three-dimensional flow that was the object of this research program.

In order to properly account for large pressure ratio expansions in multinozzle plumes all flow processes beyond shock heating that influence the temperature field should be examined. The role of nonideal thermodynamic properties of the fluid in the inviscid expansion has to be properly addressed in any plume model. The temperature difference between ideal and nonideal expansion increases with overall pressure ratio and hence altitude. The nonideal expansion process reduces the plume core temperature and therefore further compounds temperature sensitivity. Two common assumptions that must be reviewed are: (1) the exhaust medium is calorically perfect and (2) the exhaust composition is frozen. Exhaust gases can contain substantial mole fractions of water vapor and/or carbon dioxide that exhibit changing values of specific heat over the entire temperature range (500-2000 K). Other triatomic molecules can exhibit similar specific heat temperature dependence over these temperature ranges. This results in a substantial temperature decrease due to the difference between a frozen composition and the more widely employed constant γ expansion. In addition all finite rate chemical reactions cannot be considered frozen. Thus changing composition must be examined.

Assessment of the gross effects of multiple nozzle self impingement and the real gas expansion process on the plume IR signature was achieved via an analytic analysis derived and described in detail in Ref. 4-1. The analyses is for optically thin conditions and as such does not account for self absorption of the outer cooler regions of the plume. The mathematical analysis for the far field is based on standard methods which take advantage

of the exponential nature of the Planck function. The results of the analysis
was tested against computer generated plume signatures. Two model plumes were
generated and the resulting station radiation was computed using GRUMPLUME
(Ref 4-2). These results were used to show that the computed station
radiation was proportional to the derived formulas.

A schematic of the model plume flow field is shown in Fig. 4-3. The near
field multinozzle impingement and the subsequent expansion to ambient pressure
are assumed to have taken place upstream. The model studied here is a far
field model and does not address the emission from the regions near the exit
plane. The initial impingement region is highly nonuniform and requires a
much more complex formulation that would not be expected to yield simple
relationships. Two plumes were investigated corresponding to altitudes of 50
and 60 km with start line temperatures of 383 K and 745 K respectively and
water vapor mole fractions of .33 and .32. The computed centerline
properties from GRUMPLUME are shown in Fig. 4-4.

The station radiation predicted for these two test cases is shown
plotted in a normalized form in Fig. 4-5. The striking feature of the result
is that in the initial region of the far field the station radiation is a
linear function of distance. The results of the analysis are as follows. In
the initial region of the far field the initial value of the station radiation
at $z = 0$ is proportional to the product of the Planck function at the
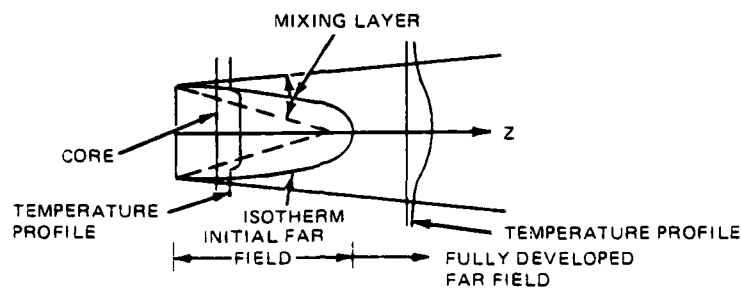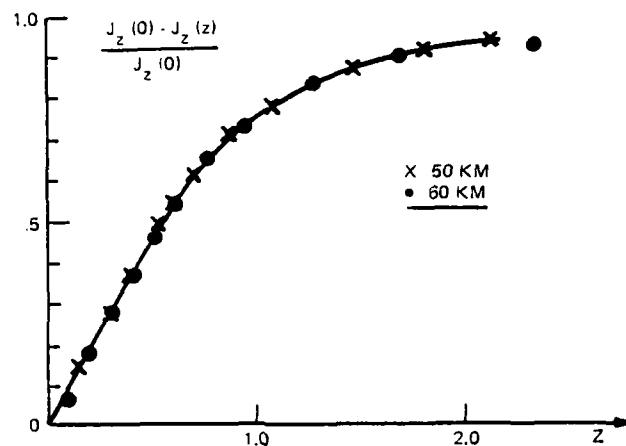
2193-008D

Fig. 4-3 Schematic of Model Plume Flow Field
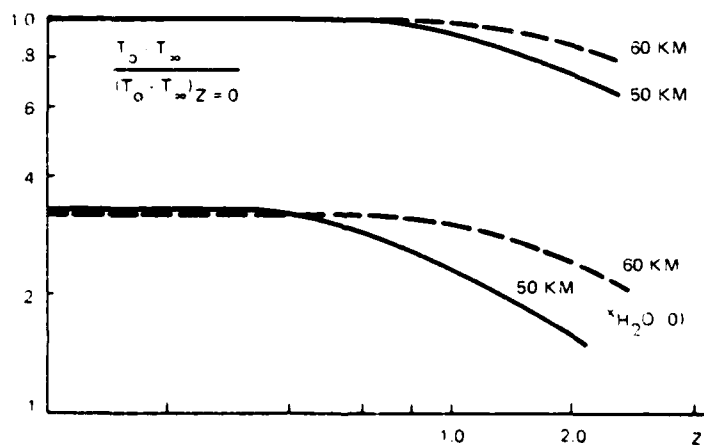
2193-009D

Fig. 4-4 Centerline Temperature and Water Vapor Mole Fraction
for Model Plumes

4-8

R-2-0051-010(T)

Fig. 4-5 Normalized Station Radiation for the Two Model Plumes
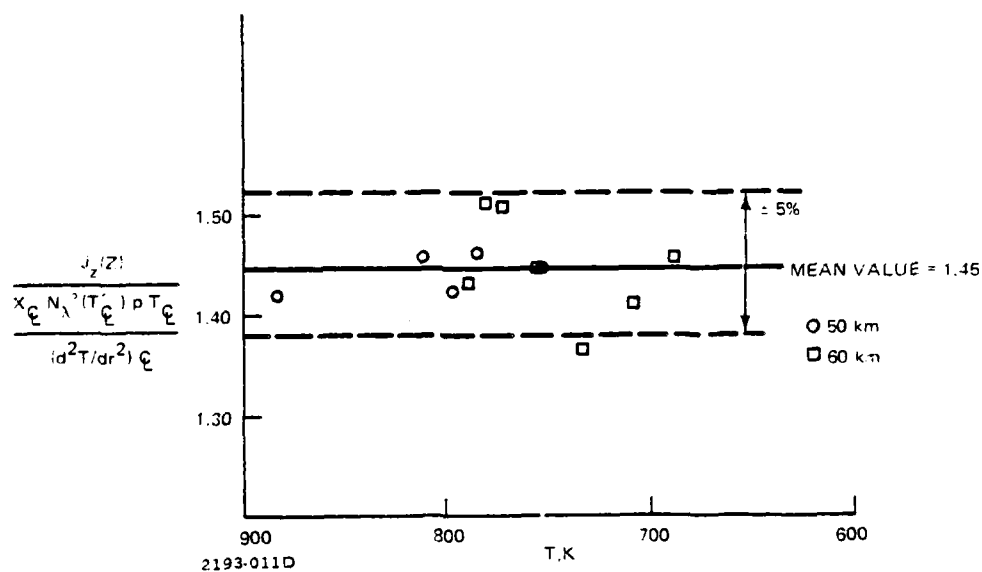

2193-011D

Fig. 4-6 Correlation of Far Field Station Radiation

initial temperature and the initial value of the mole fraction of water vapor
(the radiating species) . This formula correlated the results very well as
shown in the table below.

h	$J_z(0)$	$\dfrac{J_z(0)}{x_{H_2O}(0)\ N_\lambda{}^o(0)}$
50	2.678	3390
60	.828	3310
(all units arbitrary)		

The result is only strictly applicable for the distribution given by the model
plume. In a more accurate fluid dynamic model of the plume the initial
temperature profile would not be constant resulting in a more complex
relationship. In the plume far field, where the centerline temperature and
species mole fraction of water vapor decay both axially and radially the
results are (see Ref. 4-1 for details of the derivation)

$$J_z \quad \alpha \quad x_{H_2O}(\mathcal{C})\ N_\lambda{}^o(T_{\mathcal{C}})\ pT_{\mathcal{C}}/(d^2T/dr^2)_{\mathcal{C}}$$

The station radiation is proportional to the product of mole fraction of
radiating species, Planck function, static pressure and temperature and
divided by the second derivative of temperature all evaluated at centerline
conditions. The validity of this correlation is demonstrated in Fig. 4-6
where the entire series of points in the far field of both plumes are plotted
versus centerline temperature. All the points fall within approximately 5% of
the value 1.45.

Two plumes are sketched in Fig. 4-7: a single engine axisymmetric plume and a multiple engine three-dimensional plume. The shock heating in the axisymmetric case gives rise to a very highly peaked temperature profile because the initial shock strength is weak and increases rapidly as it nears the axis. The fraction of plume mass flow the shock intercepts when it is strong is quite low because the streamlines are continuously diverging from the axis in the plume core. In the multiple engine case, a strong shock caused by the plume impingement intercepts a large fraction of the exhaust flow near the exit plane. Therefore, the temperature profile downstream will have a flat shape and a larger fraction of the exhaust mass flow will be heated to high temperatures. In the analysis presented the effect of percentage mass flow affected by shock heating was not explicitly addressed, however, the station radiation will be proportional to that percentage. In the previous discussions it has been established that the station radiation is directly proportional to the Planck function based on the peak temperature. Figure 4-8 demonstrates what can be expected to be the variation of Planck function due to shock heating. The ordinate is the ratio of Planck function at shock heated temperature to Planck function at the isentropic expansion temperature. The abscissa is the isentropic temperature achieved by an expansion from 2000 K. Below this is an additional scale showing the corresponding altitude. Figure 4-8 includes a series of curves for an entire range of total pressure losses. The greater the total pressure loss the higher the temperature and hence the higher the ordinate. Notice the size of

SINGLE ENGINE   TOTAL
                 PRESSURE   TEMPERATURE

MULTIENGINE   TOTAL PRESSURE   TEMPERATURE
               PROFILES   PROFILES
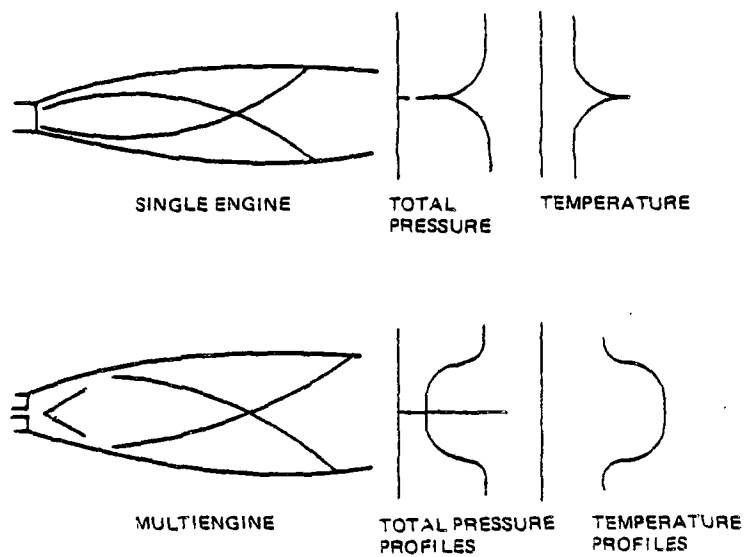
2193-012D

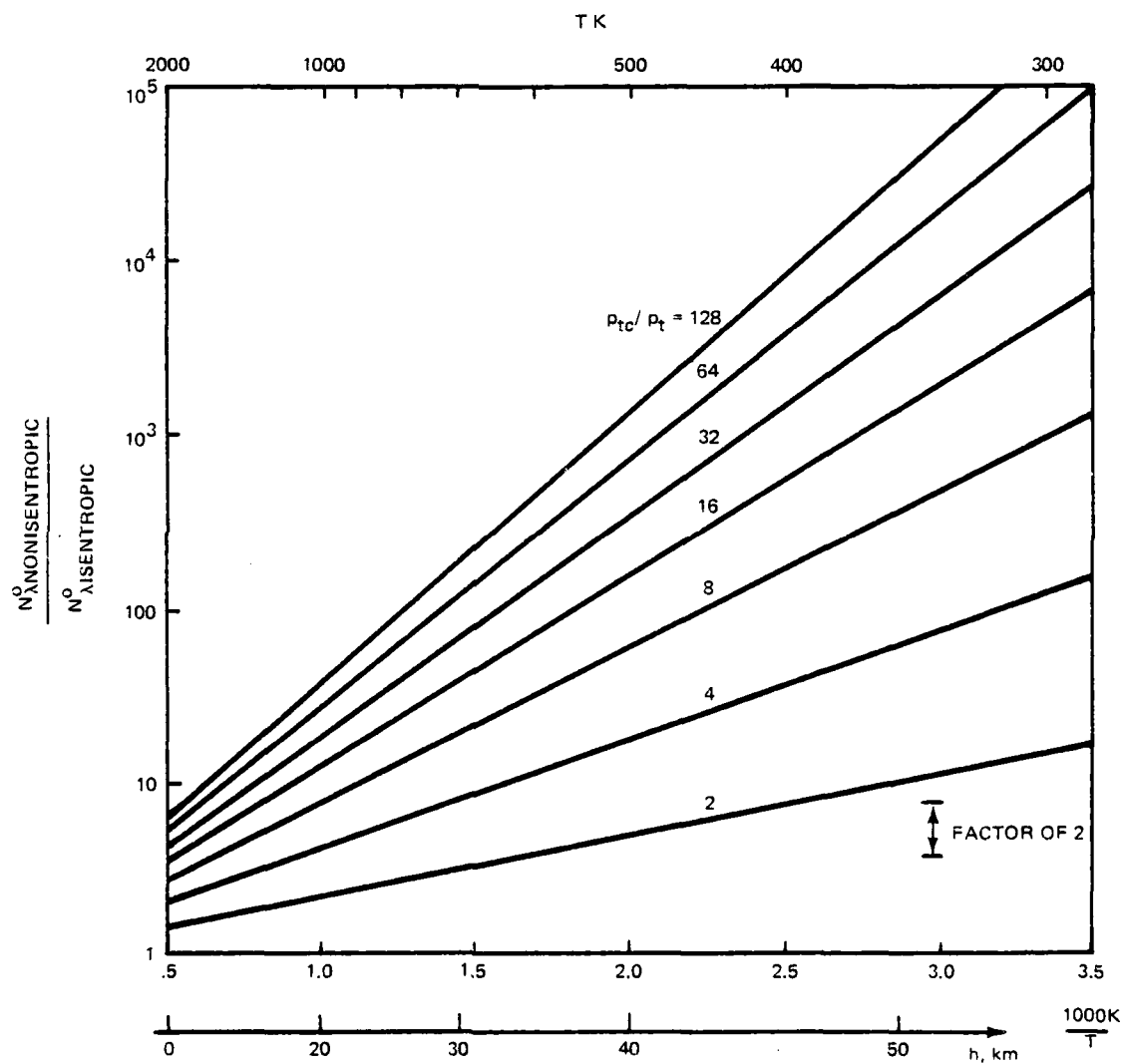Fig. 4-7 Schematic of Single Engine & Multiengine Exhaust Plumes

4-12

Fig. 4-8 Planck Function Variation with Total Pressure Loss as a
Function of Isentropic Temperature

2193-013D

a factor of 2 shown on the chart. It is clear from this chart that multiple

nozzle impingement effects become progressively more influential as altitude

increases. At low altitidues, below say 10-20 km, the individual plumes

interact only weakly so that there is little additional shock heating

developed and Fig. 4-8 shows that shock heating has diminishing influence at

those altitudes in any case.

The sensitivity of the Planck function to temperature variations

requires tight controls on all processes both numerical and physical that lead

to error beyond the shock heating caused by multiple nozzle self impingement.

There are a variety of considerations that are discussed in some detail in

Ref. 4-1. To complete the discussion in this section the role of nonideal

thermochemical properties will be examined. In Fig. 4-9 the temperature

achieved by expansion of a typical exhaust gas composition to ambient pressure

is plotted. Three isentropic expansions are shown. Two are for ideal gases

with $\gamma = 1.22$ and $\gamma = 1.3$ (γ is the isentropic exponent C_p/C_v) and one for

frozen composition. The nozzle exit plane value of γ is 1.22. It is evident

from Fig. 4-9 that above an altitude of about 20 km the assumption of a

constant value of γ will overpredict exhaust gas temperatures. The frozen

composition expansion passes smoothly between the bounds provided by the two

constant γ expansions. The frozen chemical composition expansion process is,

therefore, a more desirable feature to employ in an accurate plume model. The

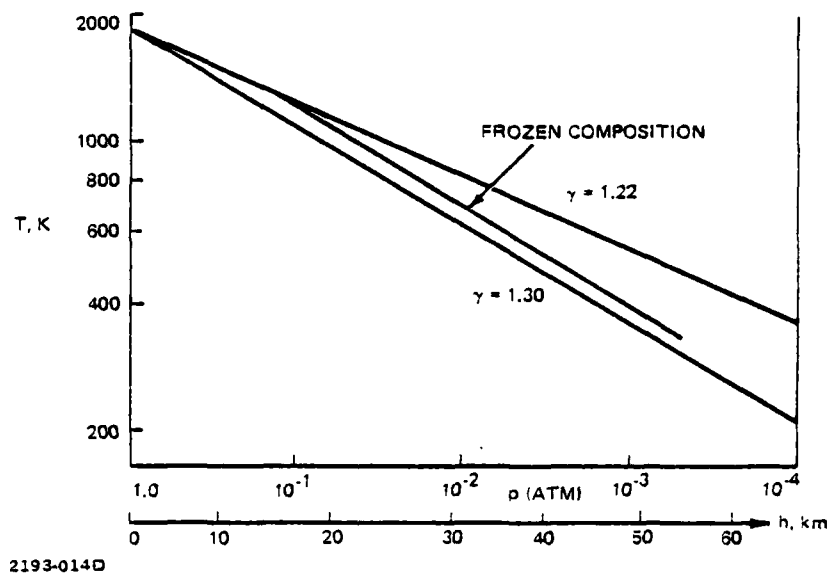accuracy of the frozen expansion process must be examined in the light of the

2193-014□

Fig. 4-9 Comparison of Frozen Composition and Constant γ Expansions

fact that chemical reactions do not necessarily freeze out even at higher altitudes. Figure 4-10 (Ref. 4-1) displays the Damkohler number as a function of altitude for the reaction set shown. Reactions 4, 5, 6, 9 can still be active at the high end of the altitude range. The possible shuffling of chemical species by these four reactions must be examined to determine if they can substantially alter the temperatures achieved by the frozen expansion.

Table I Typical Reaction Set For Amine Fuel Exhaust

$$k_R = A_R \exp(B_R/RT) / T^N$$

R									A_R	N	B_R
1	O	+	O	+	M	=	O_2	+ M	1.000E-29	1.0	0.0
2	O	+	H	+	M	=	OH	+ M	1.000E-29	1.0	0.0
3	H	-	OH	+	M	=	H_2O	+ M	2.000E-28	1.0	0.0
4	OH	+	OH			=	H_2O	+ O	1.000E-11	0.0	-1000.0
5	OH	+	H_2			=	H_2O	+ H	4.000E-11	0.0	5500.0
6	O	+	H_2			=	OH	+ H	3.000E-11	0.0	-3200.0
7	H	+	O_2			=	OH	+ O	3.000E-10	0.0	-16500.0
8	CO	+	O	+	M	=	CO_2	+ H	5.000E-29	1.0	-4000.0
9	CO	+	OH			=	CO_2	+ H	5.000E-13	0.0	-600.0
10	H	+	H	+	M	=	H_2	+ M	5.000E-29	1.0	0.0
11	CO_2	+	O			=	CO	+ O_2	3.200E-09	0.0	-54200.0
12	H_2	+	O_2			=	OH	+ OH	1.600E-10	0.0	-70400.0
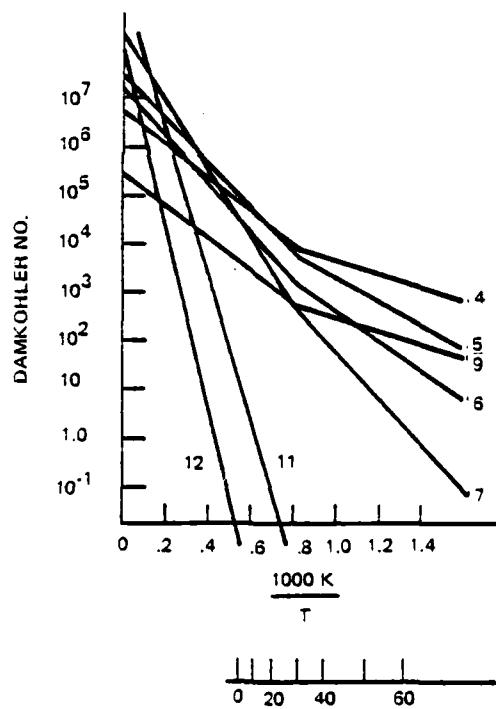
2193-015D

Fig. 4-10 Damkohler Number for Reaction
Set as a Function of Altitude

4-17

REFERENCES

4-1 Rudman, S., Del Guidice, P., Ambruso, R., "Critical Requirements for Mid Altitude IR Predictions" 11th JANNAF Plume Technology Meeting.

4-2 Slack, M., Del Guidice, P., Ambruso, R., Reed, R., Ludwig, C. Malkmus, W., Freeman, G.N., "Plume Data Analysis of Advanced Propellants, Final Report" Grumman Research Department RE-580 Oct. 1979.

SECTION 5

NUMERICAL CALCULATION PROCEDURE

The variety of possible structures of the multiple nozzle plume
impingement flow field requires that the computational procedure employed in
their analysis be as independent of geometry as possible. The code must allow
for a wide variety of shock configurations and have the flexibility to allow
for as yet unknown additional geometries. For this reason the "floating
discrete shock fitting" approach originally devised by Moretti was chosen
(Reference 5-1, 5-2). A two dimensional version of this method was employed
successfully by Salas (Reference 5-3) for a complex two dimensional scramjet
flow field containing many shock waves. For the present problem these methods
were generalized to compute three dimensional steady inviscid flow. Three
types of mesh points are recognized: interior, boundary and discontinuity. The
computational mesh is a fixed Cartesian grid where the shock surfaces and
pressure boundaries propagate freely across the grid. The shock and pressure
boundary surfaces are portrayed as discontinuity surfaces and, for example,
the complex impingement shock/boundary interaction is modelled in detail as a
point singularity.

The discontinuity surfaces are considered on a cell by cell basis so that
the computer code must contain the necessary logic to perform the correct
calculations in all possible cases. Because the cross angle of the
discontinuity surfaces must be determined to compute propagation velocity the
discontinuity cells must be connected. Thus the computations necessary for
each discontinuity cell cannot be done independent of properties in
neighboring cells. The number of possible configurations is large but
manageable for single shock surfaces because it is possible to devise rules to
cover a large portion of the possibilities and to identify and code for the

5-1

exceptions. When two shock surfaces intersect, the geometric possibilities and hence complexity increases enormously with the attendant increases in program logic. The marching step size is restricted to maintain the same configuration of discontinuity cells for each step. At the end of each step, if any of the discontinuities has reached a mesh point, it is crossed to the other side and all the necessary indicators which guide the program logic are reset to account for the new configuration.

The exhaust gas is considered inviscid, thermally and calorically perfect and is governed by the three dimensional Euler equations. In Cartesian coordinates, the conservation of mass, momentum and entropy are

$$u_x + v_y + w_z + \gamma \, (uP_x + vP_y + wP_z) = 0 \tag{5-1.1}$$

$$uu_x + vu_y + wu_z + TP_x = 0 \tag{5-1.2}$$

$$uv_x + vv_y + wv_z + TP_y = 0 \tag{5-1.3}$$

$$uw_x + vw_y + ww_z + TP_z = 0 \tag{5-1.4}$$

$$uS_x + vS_y + wS_z = 0 \tag{5-1.5}$$

where u, v, w are the Cartesian velocity components in the x, y, z directions and P is the natural logarithm of the pressure, S the entropy, T the temperature, γ the ratio of specific heats and all thermodynamic quantities are non dimensionalized by the stagnation conditions (e.g., p_0, ρ_0, T_0), the velocity components with respect to the quantity $\sqrt{p_0/\rho_0}$ and the coordinates by the nozzle exit radius. The marching (time like) direction is the z direction and the following two flow angles are introduced

$$\tau = u/w \qquad \qquad 5\text{-}1.6$$

$$\sigma = v/w \qquad \qquad 5\text{-}1.7$$

Subtract Eq. (5-1.4) multiplied by u from Eq. (5-1.2) multiplied by w and divide the results by w^2 to get

$$\tau\tau_x + \sigma\tau_y + \tau_z + (1/w^2)(P_x - \tau P_z) = 0 \qquad \qquad 5\text{-}2.1$$

Similarly an equation for σ is derived from Eqs. 5-1.4 and 5-1.3

$$\tau\sigma_x + \sigma\sigma_y + \sigma_z + (1/w^2)(P_y - \sigma P_z) = 0 \qquad \qquad 5\text{-}2.2$$

Subtract Eq. (5-1.4) from Eq. (5-1.1) times w and divide the result by w^2 to get

$$\tau_x + \sigma_y + \gamma(\tau P_x + \sigma P_y + P_z(1 - 1/\gamma w^2)) = 0 \qquad (5\text{-}2.3)$$

Divide Eq. (5-1.5) by w to get

$$\tau S_x + \sigma S_y + S_z = 0 \qquad \qquad 5\text{-}2.4$$

Equations (5-2.1 - 5-2.4) form a set of four equations for the four primary unknowns τ, σ, P and S. The remainder of the flow quantities are derived from the following subsidiary equations. Employing the conservation of stagnation enthalpy the equation for w (the axial velocity)

$$w^2 = \frac{2\gamma(1-T)}{(\gamma-1)(1+\tau^2+\sigma^2)} \qquad \qquad 5\text{-}3.1$$

The equation of state for T

$$T = \exp(((\gamma-1)P + S)/\gamma) \qquad \qquad 5\text{-}3.2$$

The definitions (5-1.6) and (5-1.7) for u, v

$$\begin{aligned} u &= \tau w \\ v &= \sigma w \end{aligned} \qquad \qquad 5\text{-}3.3$$
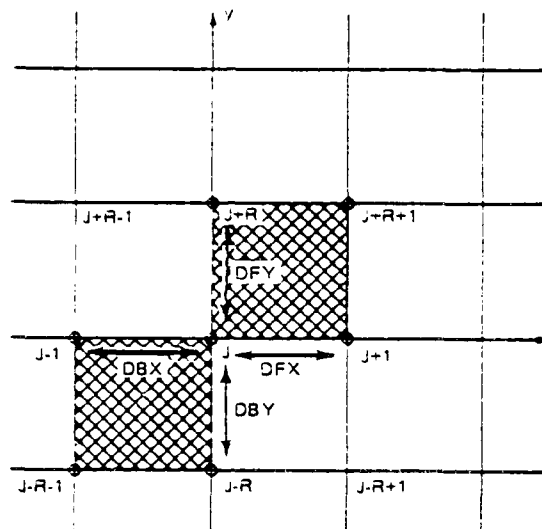
The interior points are calculated by the integration of Eqs. (5-2.1 - 5-2.4) employing the two step MacCormack scheme (Ref. 5-4). The marching direction is the z axis and the sequence of calculations is to solve for P_z from Eq. (5-2.3), then using this value in (5-2.1) and (5-2.2) solve for τ_z and σ_z. S_z is computed directly from Eq. (5-2.4). The basic notation for mesh points and cells is shown in Fig. 5-1, which depicts a segment of the computational plane. Each mesh point is located by a single integer and identified in the figure by an upper case letter. Along each row the mesh point number increases one by moving one mesh point to the right and increases by R, the number of points in each row, by moving up one mesh point. Each cell is identified by the value of J of the lower left hand mesh point and denoted by J. This single array notation, though unconventional, produces some programming simplification, and does not increase computer operations since the normal double subscript approach requires the (transparent to the user) same computations to locate a variable.

The complete details of the use of the MacCormack finite difference algorithm are given in many places (c.f., Ref. 5-4) and will not be repeated here. In the integration scheme, transverse partial derivatives (derivatives in the plane normal to the marching direction) are evaluated by two point forward or backward formulas. The notation for the transverse derivatives in shown in Fig. 5-2. For any of the flow quantities, the following formula are employed for the finite differences at point J.
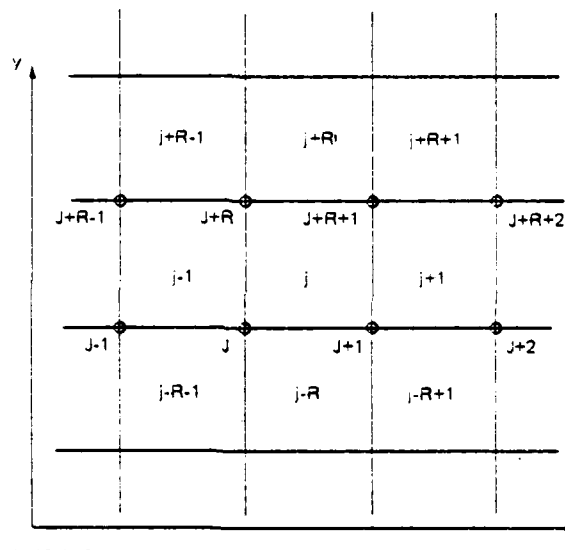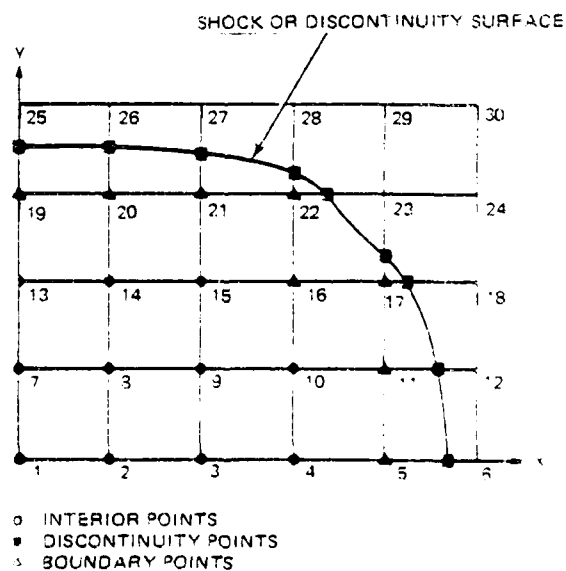
2193-016D

Fig. 5-1 Basic Notation Employed in the Finite Difference Mesh

2193-017D

Fig. 5-2 Notation for Forward and Backward Differences

SHOCK OR DISCONTINUITY SURFACE

o   INTERIOR POINTS
■   DISCONTINUITY POINTS
◊   BOUNDARY POINTS

2193-018D

Fig. 5-3 Sample Finite Difference Mesh

Forward Differences

x direction $\qquad DFX(V) = \dfrac{V(J+1) - V(J)}{\Delta x}$

y direction $\qquad DFY(V) = \dfrac{V(J+R) - V(J)}{\Delta y}$

Backward Differences

x direction $\qquad DBX(V) = \dfrac{V(J) - V(J-1)}{\Delta x}$
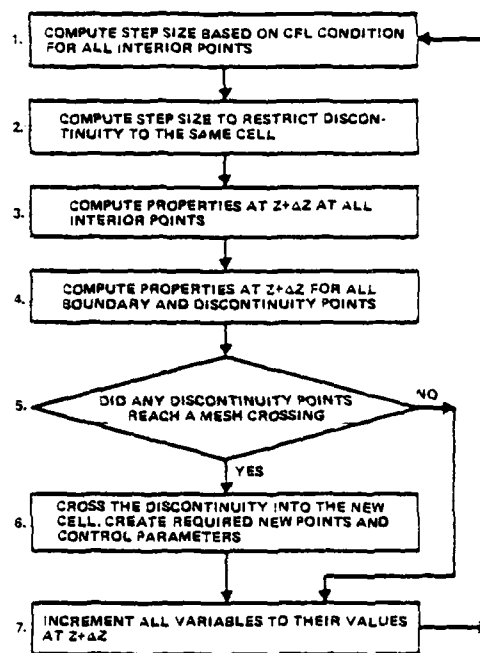
y direction $\qquad DBY(V) = \dfrac{V(J) - V(J-R)}{\Delta y}$

where V is any flow quantity and the equations define the symbols DFX, DFY, DBX and DBY. Combinations of forword and backward differences for the x and y directions is permitted in the predictor step so long as it is reversed in corrector step. If backward differences are employed for both x and y in the predictor step and forward differences in the corrector step the new values at $Z + \Delta Z$ at point J depend only on the seven mesh points bounding the two shaded cells in Fig. 5-2. If there is a discontinuity, a shock wave for example, in either of these shaded cells, then the computation at point J must be modified to account for it. The orientation of this "finite difference molecule" dictates a computational logic in terms of defining how mesh points are affected by discontinuity cells.

Figure 5-3 shows a typical computational mesh denoting the mesh numbering system and snowing a single continuous shock or discontinuity

surface. Three types of points are indicated on the figure: interior points, boundary points and discontinuity points. Boundary points are those interior points associated with a finite difference molecule (see Fig. 5-2) which have a discontinuity passing through it and so cannot be computed employing the standard interior point calculation scheme. The steps involved in one computational step are outlined in Fig. 5-4. The necessity for step 2 is to maintain the overall configuration, that is, all interior points remain interior points, boundary points remain boundary points for both the predictor and corrector portions of the calculation.

In step 4 (Figure 5-4), the computation of the properties at the discontinuity and boundary points of each cell containing a discontinuity is considered individually. The discontinuity surfaces are considered to be oriented so as to recognize the high and low pressure sides. The projection of the discontinuity surfaces on the transverse or computational plane results in a continuous line (c.f., Figure 5-3). If this line is followed from a prescribed starting point, for each cell, the discontinuity can enter on any one of four faces and leave on any of the remaining three faces - giving a total of twelve possible configurations shown in Fig. 5-5. In the computer program, for each discontinuity cell, the properties at the discontinuity point which is the entry point to the cell are associated with that cell. For each of the twelve possible configurations for the discontinuity cells the computer code contains the necessary logic to determine which mesh points are boundary points and which discontinuity points are to be calculated. At any step the code contains a table of the discontinuity cells and the program logic determines the method of calculation for each of the unknown points. A typical example of a discontinuity cell is shown in Figure 5-6. A shock

1. COMPUTE STEP SIZE BASED ON CFL CONDITION FOR ALL INTERIOR POINTS

2. COMPUTE STEP SIZE TO RESTRICT DISCONTINUITY TO THE SAME CELL

3. COMPUTE PROPERTIES AT $Z+\Delta Z$ AT ALL INTERIOR POINTS

4. COMPUTE PROPERTIES AT $Z+\Delta Z$ FOR ALL BOUNDARY AND DISCONTINUITY POINTS

5. DID ANY DISCONTINUITY POINTS REACH A MESH CROSSING — NO / YES

6. CROSS THE DISCONTINUITY INTO THE NEW CELL. CREATE REQUIRED NEW POINTS AND CONTROL PARAMETERS

7. INCREMENT ALL VARIABLES TO THEIR VALUES AT $Z+\Delta Z$

2193-019D

Fig. 5-4 Flow Diagram for One Step Using Floating Discontinuity Finite Difference Computer Program
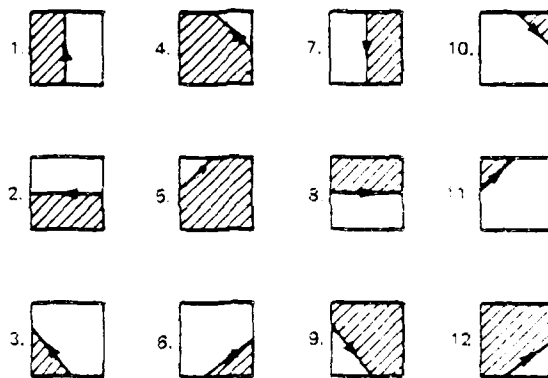
(SHADING INDICATES HIGH PRESSURE SIDE OF SHOCK OR INTERIOR
SIDE OF A PRESSURE BOUNDARY.)

2193-020D

Fig. 5-5 The Twelve Discontinuity Cell Configurations

2193-021D

Fig. 5-6 Notation Used for Discontinuity Calls

enters from the bottom face of the cell and leaves through the top face. To the right of the shock the flow is known (i.e. undisturbed free stream or undisturbed plume). The code logic determines, for this configuration, that the two points to be calculated associated with the j cell are mesh point J and shock point S_j. The unknowns at S_j are the values of τ, σ, P and S on the high pressure side of the shock and the shock point velocity df_j/dz where f_j is the fractional distance of S_j from J (see Fig. 5-6).

The shock configuration shown in Figure 5-6 is the simplest possible. Each of the discontinuity cells is a type 1 as defined in Figure 5-5. The computation of the shock cross flow angle is computed by locating the shock points on either side of the point of interest. This is achieved by looking ahead and behind the discontinuity cell j and locating the shock points in cell j-R and j+R. In this case, the location of the shock point in j+R (j-R) is at $y = \Delta y$ ($y = -\Delta y$) and $x = f_{j+R}\Delta x$ ($x = f_{j-R}\Delta x$) (x, y both measured relative to the mesh point J). In other configurations where cell j-R is type 4 or type 11 (see figure 5-5) the computation of the location of the preceeding shock point follows a different formula. Likewise for the following point. In the configuration shown, the point J is a boundary point and must be calculated accordingly. For each triplet of types of discontinuity points (in Figure 5-6 this is a 1-1-1) a logic pattern is designed to compute the shock cross angle correctly and to determine which point is a boundary point.

The calculation procedure used for discontinuity points and boundary points is outlined below for a two dimensional flow-the extension of these methods to three dimensions is straight forward geometrically but requires some analysis pertinent to three dimensional characteristic theory

and will be discussed in subsequent paragraphs. Three ideas must be developed in order to explain this procedure: (1) computation of characteristic relationships using finite difference algorithms (2) slant marching steps and (3) pseudo point values. Points A, B and C form the finite difference molecule for the computation of the values at point N in a two dimensional MacCormack finite difference scheme (Fig. 5-7). (Note that the intermediate values employed in the predictor/corrector scheme are only notational simplifications and that only values of properties at A, B and C are employed in the computation of N.) The object here is to show how the values computed by the finite difference calculation can be used to compute the characteristic relationships at N without the need for interpolating the values at the points denoted + and − which are at the foot of the characteristics (Figure 5-7). Denote the values at N computed by a second order finite difference scheme to be u_{FD}, w_{FD}, P_{FD}, S_{FD} from which ν_{FD} (ν is the Prandtl Meyer angle) can be computed. The two characteristic relationships associated with point N (second order accurate) are

downward wave $\qquad \Delta\theta + \Delta\nu = \overline{\Gamma}_{-}\,\Delta z \qquad (\ \overline{\Gamma}_{-} = \tfrac{1}{2}(\ \Gamma_{-} \ + \ \Gamma_{N})\,)$

upward wave $\qquad \Delta\theta - \Delta\nu = \overline{\Gamma}_{+}\,\Delta z \qquad (\ \overline{\Gamma}_{+} = \tfrac{1}{2}(\ \Gamma_{-} \ + \ \Gamma_{N})\,)$
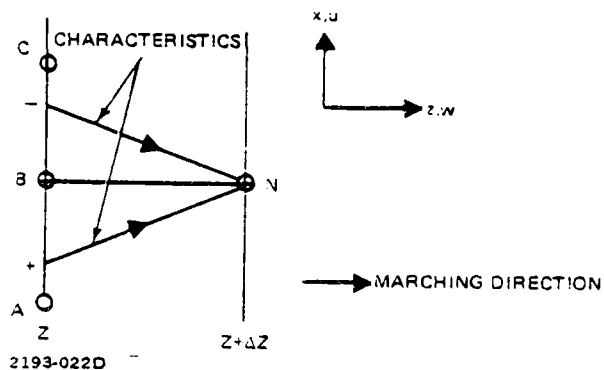
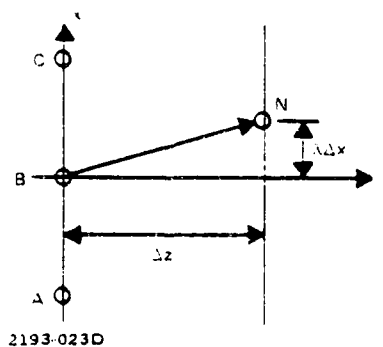Fig. 5-7 Finite Difference Molecule for Two Dimensional Flow

Fig. 5-8 Notation for Slant Step

Where Γ is the inhomogeneous or forcing term containing velocity gradients out of the plane (c.f. Ref. 5-5 for derivation of these equations). Employing the notation of Fig. 5-7, these relationships become

$$\theta_N + \nu_N = \overline{\Gamma}_- \Delta z + \theta_- + \nu_-$$

$$\theta_N - \nu_N = \overline{\Gamma}_+ \Delta z + \theta_+ - \nu_+$$

In the straightforward application of the method of characteristics, these two equations are employed to solve for the two unknowns θ_N and ν_N. This requires the interpolation of data to determine $\theta_\pm$, $\nu_\pm$ and $\Gamma_\pm$. Because the finite difference result and the characteristic result must be the same to second order

$$\theta_N + \nu_N = \overline{\Gamma}_- \Delta z + \theta_- + \nu_- = \tan^{-1}(u_{FD}/w_{FD}) + \nu_{FD}$$

$$\theta_N - \nu_N = \overline{\Gamma}_+ \Delta z + \theta_+ - \nu_+ = \tan^{-1}(u_{FD}/w_{FD}) - \nu_{FD}$$

Thus, the simple result at point N for the two characteristic relationship is

$$\theta_N + \nu_N = \tan^{-1}(u_{FD}/w_{FD}) + \nu_{FD}$$

$$\theta_N - \nu_N = \tan^{-1}(u_{FD}/w_{FD}) - \nu_{FD}$$

which does not require any interpolation or any scheme other than the ordinary finite difference algorithm used at any interior point.

Figure 5-8 shows that (for the discontinuity point) the new values desired at $z + \Delta z$ do not lie on the same value of x as point B, rather the point N is elevated by $\lambda \Delta x$. The computation of this point is made simply by forming a directional derivative from the governing equations. For any system of partial differential equations

$$\frac{\partial U}{\partial z} = A \frac{\partial U}{\partial x} + B$$

where A and B are the matrices appropriate to the equations of interest and U is the unknown vector. To compute the values at point N use the system

$$\frac{dU}{dz} = \frac{\partial U}{\partial z} + \frac{\partial U}{\partial x} \frac{\Delta x}{\Delta z} = \left(A + I \frac{\Delta x}{\Delta z} \right) \frac{\partial U}{\partial x} + B$$

where I is the identity matrix and dU/dz is now the derivative used to compute point N from point B in Fig. 5-8 by a "slanted step." The finite difference scheme is applied to the right hand side of this equation using exactly the same rules as are used at any interior point resulting in a second order accurate predication at N.

The final ingredient necessary for the boundary point calculation is the pseudo or projected point. Figure 5-9a shows the typical configuration encountered in the "shock between the mesh points" type calculation. In general at station z the required properties are known at mesh points A and B and on the high pressure side of S the shock point. These points do not form the standard equally spaced finite difference molecule. In order to use the same algorithm that is used at all other mesh points, the finite difference molecule shown in Fig. 5-9b is constructed. The values of the flow variables at the point P are calculated by a simple linear extrapolation from the values
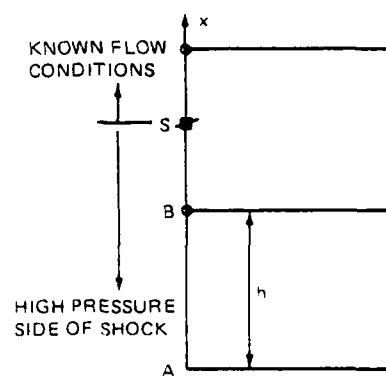
a) SHOCK BETWEEN MESH POINT CONFIGURATION
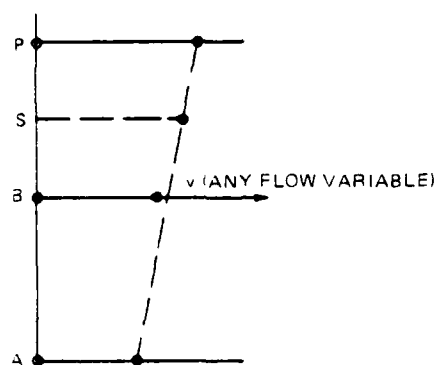
b) CALCULATION OF PSEUDO POINT

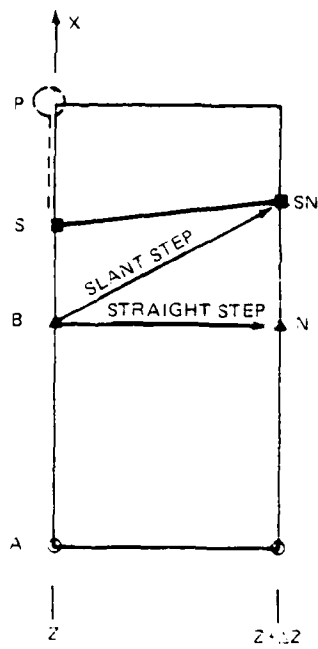2193-024D

Fig. 5-9 Pseudo Point Construction

at A and S. The value at B is not used. This technique has the critical property that for geometries where point S is very close to point B truncation errors are not amplified in creating the value at P. This molecule can be shown to produce a first order rendition of the distribution of flow properties on the mesh segment ABS. However, a simple comparison between the Taylor series expansions employing properties at A, B and S with one employing A, B and P shows that the error involved is, in the worse case, $(1/8)$ $(\partial^2 f / \partial x^2) h^2$ (f being any flow property). Thus reasonably small errors are expected from this approximation.

The sequence of steps for calculating a typical boundary and shock point (the flow upstream of the shock is known in this case) are as follows (refer to Fig. 5-10): (1) the shock location at $z + \Delta z$ (SN) is estimated based on the known shock slope at S; (2) the flow variables at point P are computed: (3) the finite difference molecule ABP is employed to compute the values at point N using the standard MacCormack scheme; (4) the slant step and same procedure is used to compute the finite difference values of the new variables at SN; (5) these new values are combined to yield a single characteristic equation - in this case

$$\theta_{SN} - \nu_{SN} = \tan^{-1} \ (u_{FD}/w_{FD}) - \nu_{FD};$$

(6) the Rankine-Hugoniot equations and two estimates of the shock slope at SN are used to calculate two solutions for the conditions behind the shock at SN: (7) assume linear variation between these two solutions to derive a linear equation

$$\theta_{SN} + a \nu_{SN} = b$$

2193-025D

Fig. 5-10 Mesh Configuration for Floating Shock Calculation

for properties behind the shock; (8) solve the two equations from step (7) and step (5) for the shock properties at SN. The accuracy of the scheme is further enhanced by correcting the location of the shock at SN based on an average slope between S and SN and repeating the sequence 1-8 above.

The discontinuity point calculation procedure for three dimensional flow requires additional analysis. The procedure presented for two dimensional flow takes full advantage of supersonic flow theory. This theory provides a direct relationship between the geometric flow angle θ and the Prandtl Meyer angle along characteristic lines. In three dimensional flow, there is no simple direct relationship between flow orientation and Prandtl-Meyer angle. The flow direction at any point is described by two angles, τ and σ for example, and is not unique. In the past investigators (Refs. 5-6, 7, 8,9) have employed "reference plane" characteristics to overcome this complication. In this method, a plane is prescribed a priori which is oriented in a direction convenient to the calculation. That is, the direction chosen simplifies program logic and reduces the need for interpolation to a minimum. The components of the velocity vector in these planes are treated as two dimensional flows and are evaluated based on a method of characteristics analysis in the reference plane. Velocity components out of the reference plane are computed by an auxiliary equation - usually the transverse momentum equation. Velocity gradients and the transverse velocity components appear in the inhomogeneous or forcing term in the reference plane characteristic equations. In the present calculation procedure, a new method is described. It is based on a theoretical analysis which demonstrates that there are in fact distinguished planes, in a local sense, in which the flow is described by equations in two space dimensions.

In three dimensional supersonic flow, the zone of dependence of a point in the flow is the upstream Mach cone. Each generator of this cone is a bicharacteristic. It was demonstrated in Ref. 5-10 that two of the infinite number of bicharacteristics on this Mach cone play exactly the same role as do the two characteristics in axisymmetric flow. These bicharacteristics are along the intersection of the Mach cone and the osculating plane of the streamline Figure 5-11. The osculating plane contains the tangent vector and principal normal to the streamline. The normal to this plane is in the binormal (or b) direction. There are no velocity components normal to the osculating plane. In fact the equations of motion normal to this plane reduce to $\partial p/\partial b = 0$ (p is the static pressure and b is the coordinate in the binormal direction). In the osculating plane there is the familiar relationship between changes in flow angle and changes in Prandtl Meyer angle that exists for axisymmetric flow. Only the gradient in the b direction of velocity component in the b direction appears in the equations. The entire computational scheme devised for the discontinuity point calculation for two dimensional (or axisymmetric) flows can be employed in the three dimensional flow in the osculating plane. In general the binormal direction is given by $\vec{b} = \vec{\nabla p} \times \vec{q}$ (q is the local velocity vector, $\vec{b}$ is a vector parallel to the unit vector b). This formula is based on the properties that the b vector be normal to both the tangent vector and acceleration vector of a fluid element. $\vec{q}$ is tangent to the streamline and ∇p is parallel to the acceleration vector. Thus the orientation of the $\hat{b}$ vector or alternatively the orientation of the osculating plane are determined along with the solution.

OSCULATING PLANE

$\hat{t}$

STREAMLINE

$\hat{b}$

STREAMLINE

$\hat{n}$

PRIMARY BICHARACTERISTICS

MACH CONE
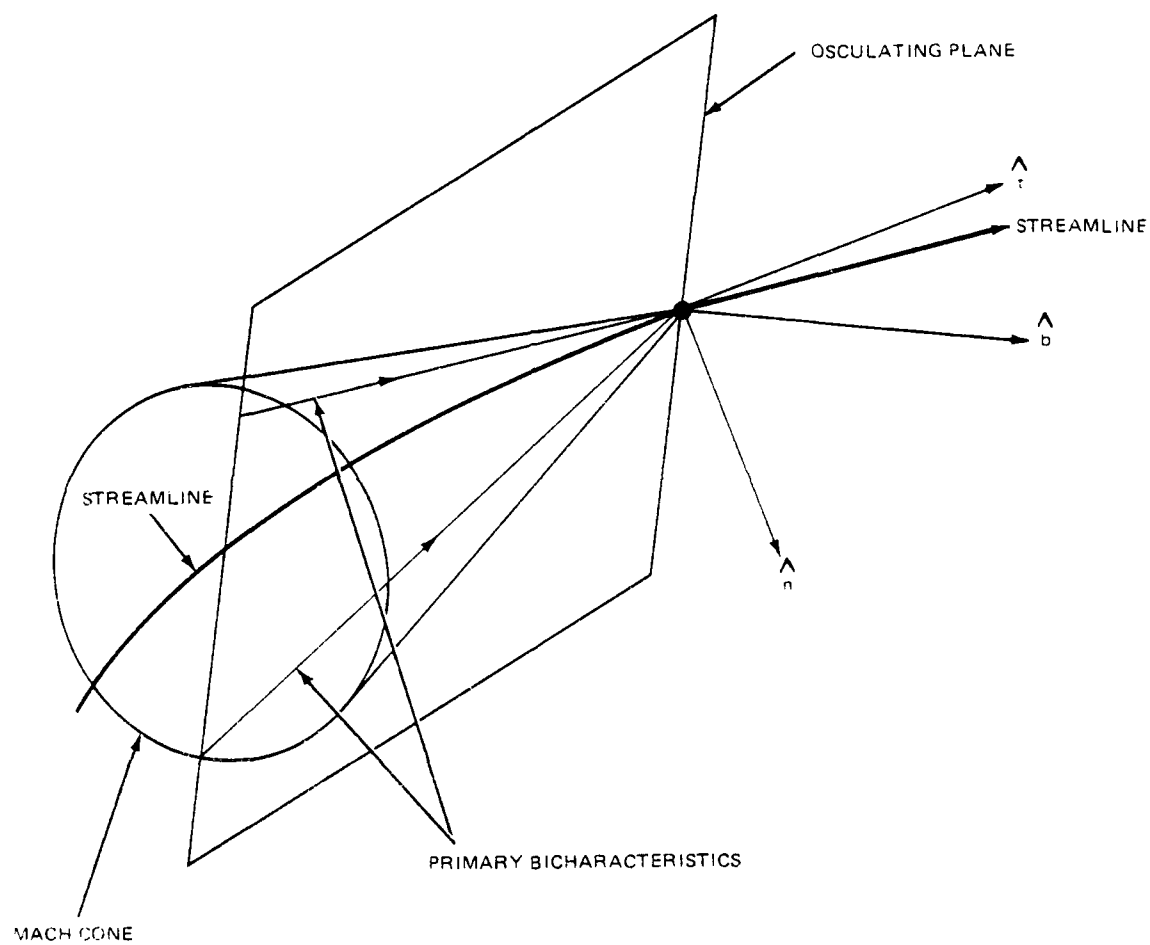
$\vec{R}$ = POSITION VECTOR OF FLUID PARTICLE

$\hat{t} = \dfrac{(d\vec{R}/ds)}{|q|}$ = UNIT TANGENT VECTOR

$\hat{n} = \dfrac{d\hat{t}/ds}{\kappa}$ = UNIT NORMAL VECTOR

$\hat{b} = \hat{n} \times \hat{t}$ = BINORMAL VECTOR

2193-026D

Fig. 5-11 The Osculating Plane and the Primary Bicharacteristics

To demonstrate the use of this theory the three dimensional shock point calculation is outlined below. Figure 5-12 shows a schematic of the shock point calculation. All flow properties are known at station z including the shock velocity in the y direction. The procedure follows exactly the steps outlined in the two dimensional calculation described in the previous paragraphs with the following additions. The shock position at all points at z + Δz are computed as a first estimate by simple forward integration. Thus

$$YSN = YS + (dYS/dz)\Delta z$$

where YSN (YS) is the value of the shock height at z + Δz (z) on the vertical grid line through mesh point B (N) and dYS/dz is the shock velocity in the y direction at station z on the same grid line. After computing the new location of the shock on each mesh line the shock cross flow angle can be determined by a simple centered difference of the locations at SN $^+$ and SN $^-$ (see Fig. 5-12). The only unknown parameter for the shock geometry at point SN is dYSN/dz or the shock speed at station z + Δz. As in the two dimensional case (step 6) two values are assumed for the shock speed. In the 3D case the two velocity vectors associated with these two assumed shock normals are used to define the $\hat{b}$ direction (Fig. 5-13). The remainder of the calculation procedure is identical with the 2D procedure. It is not clear that this is only method for computing the $\hat{b}$ vector. The method is linked to the way the shock cross angle is computed. This is nonunique and the influence of variations of this step on calculated results should be studied. The method presented is self consistent and achieves accurate and reliable results when combined with the rest of the computational procedure.

5-23

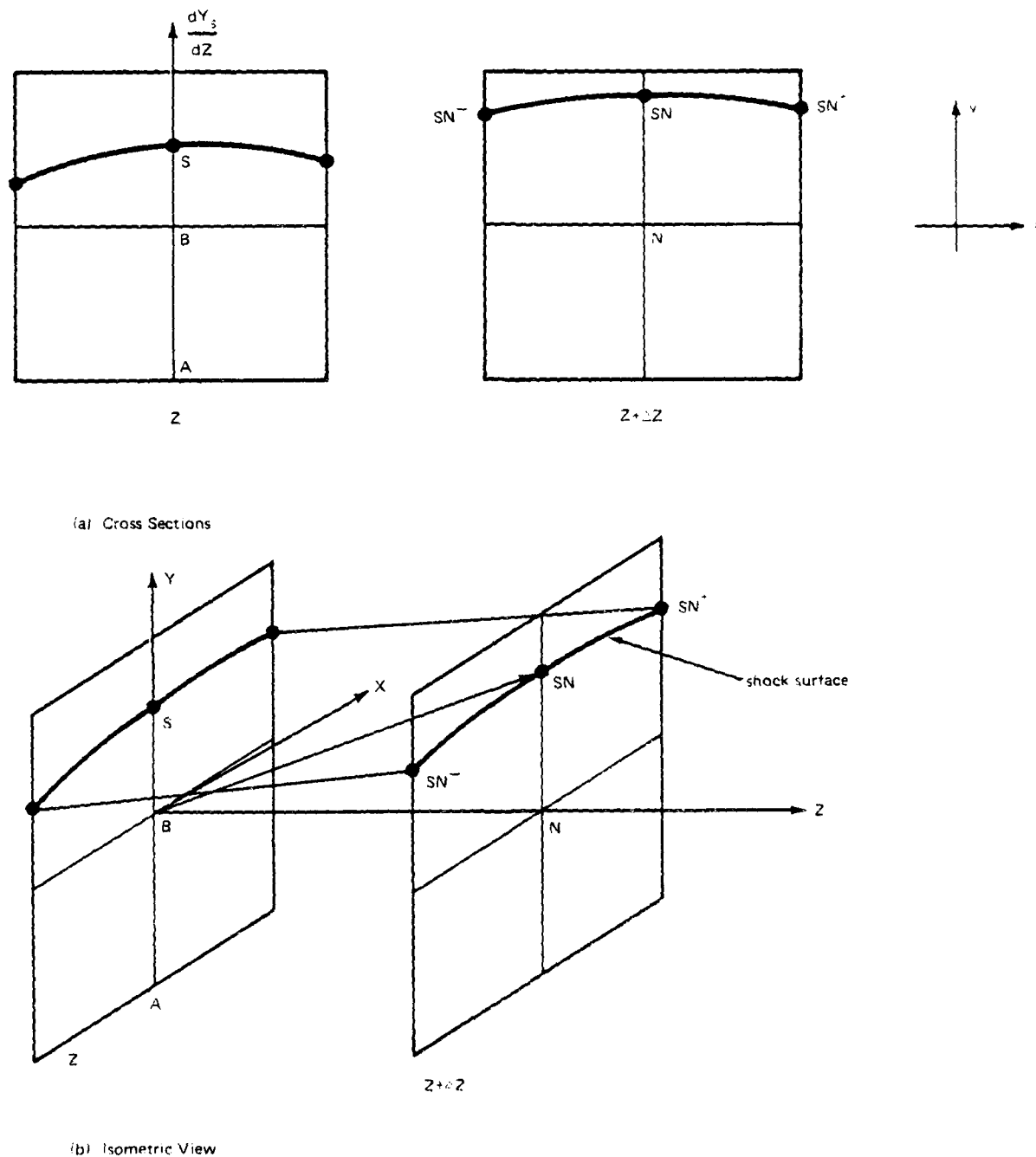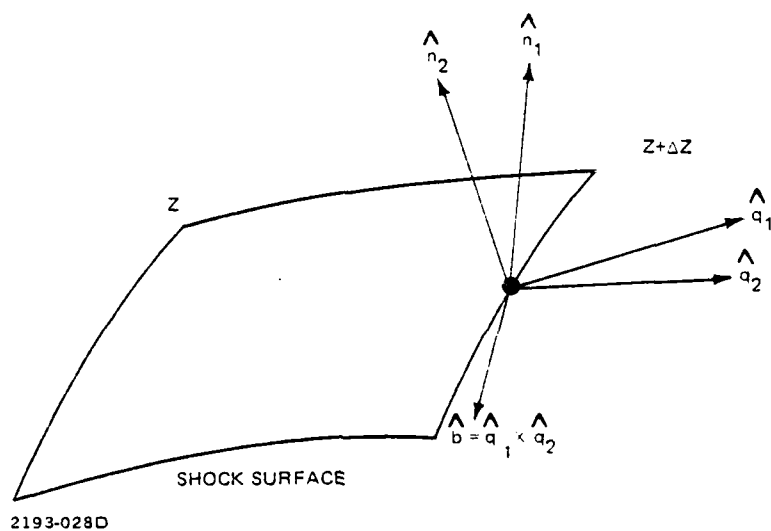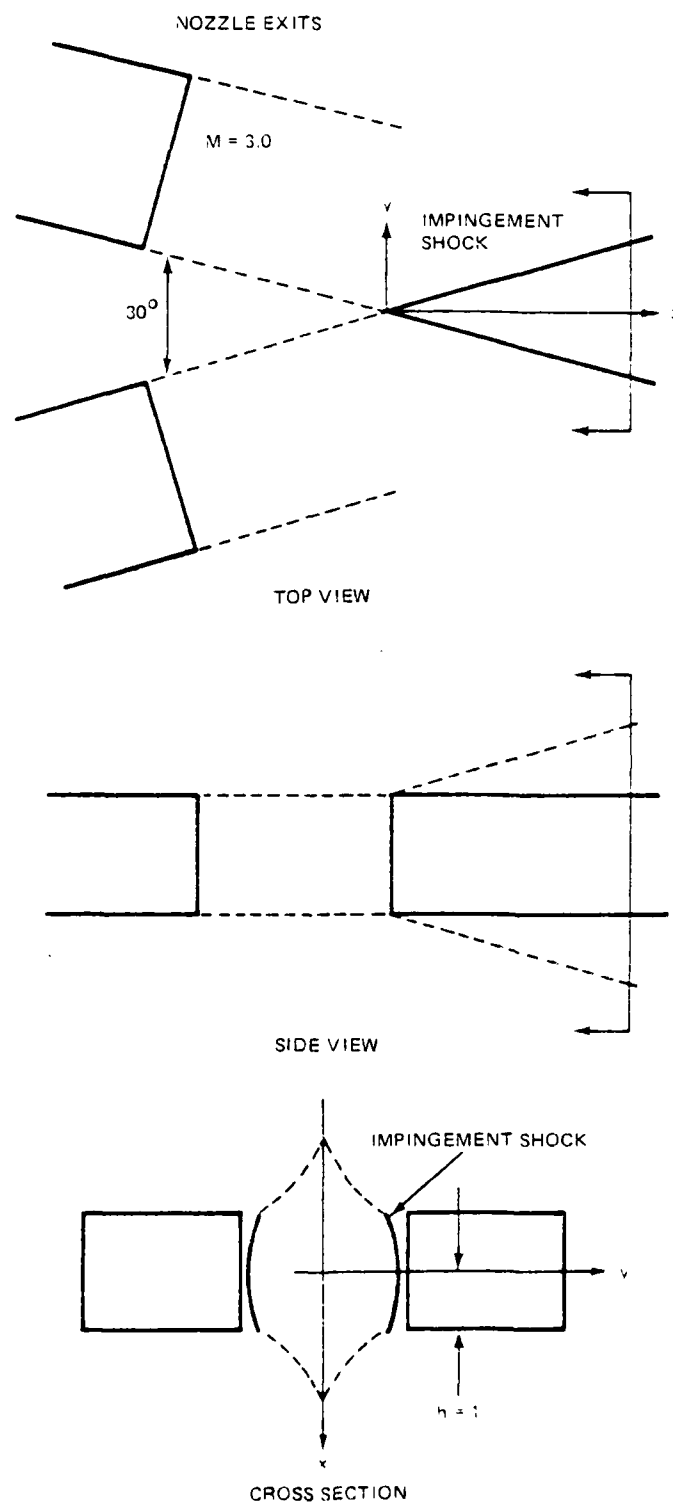(a) Cross Sections

(b) Isometric View

Fig. 5-12. Schematic Diagram Showing Notation for Three-Dimensional Shock Computation

2193-028D

Fig. 5-13 Definition of the $\hat{b}$ Vector for the Shock Point Calculation

A computation employing the three dimensional floating discontinuity program was achieved for the flow field created by the impingement of two uniform rectangular jets. This geometry was chosen so as to minimize the complexity brought about by nonuniformities in the underexpanded plume. The geometry describing the initial calculation is shown in Fig. 5-14. Two uniform Mach 3.0 plumes of rectangular cross section impinge at 30°. Impingement shocks spread across the plumes (top view) to make the two flows parallel. This results in pressure above the background, and the flow spreads laterally (side view) to relieve this overpressure. The cross-section shown in Fig. 5-14 is characteristic of the calculated results. The impingement shocks are slightly curved and are bounded by the free jet boundary. The pressure boundaries spread laterally in a vee shaped pattern. A typical cross section from the calculation is shown in Fig. 5-15. (Only one fourth of the total cross section is shown because the flow has bilateral symmetry). The flow from the undisturbed plume passes downward through the impingement shock and jumps in pressure. The impingement shock intersects the undisturbed plume boundary in a complex interaction involving a sonic shock condition and a sonic shock condition and a centered Prandtl Meyer fan with the combined result of no pressure change along the pressure boundary. Figure 5-16 is a schematic of the flow near that point. The flow is decomposed into components tangential and normal to the shock wave/plume boundary intersection line. (see Section 6 of this paper for detailed discussions relating to this type of analysis). In the plane normal to the intersection line the shock wave is sonic at the point of impingement. Attached to the impingement point is a centered expansion which reduces the pressure back to ambient. The

5-26

NOZZLE EXITS

M = 3.0

30°

IMPINGEMENT
SHOCK

y

z

TOP VIEW

SIDE VIEW

IMPINGEMENT SHOCK

x

y

h = 1

CROSS SECTION

2193-029D

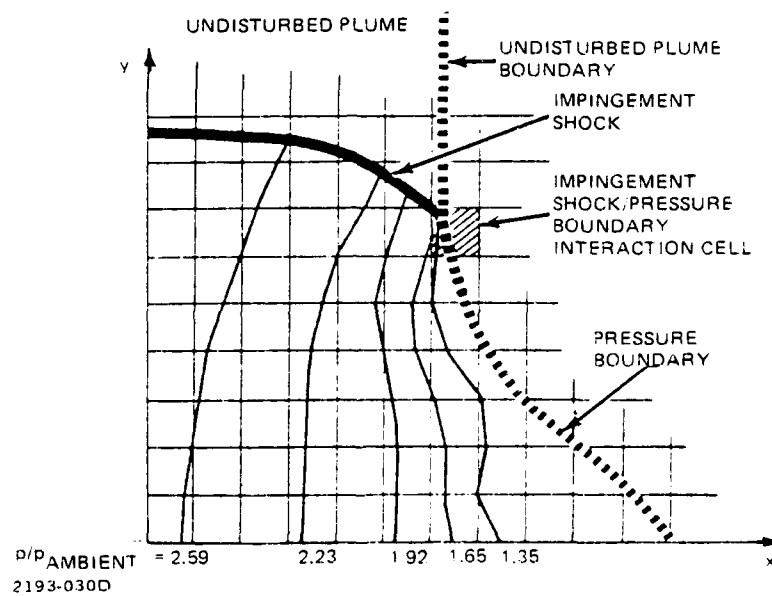Fig. 5-14 Schematic of Geometry for the Impingement
of Two Rectangular Plumes

Fig. 5-15 Typical Cross Section at z = 2.12 Including Isobars
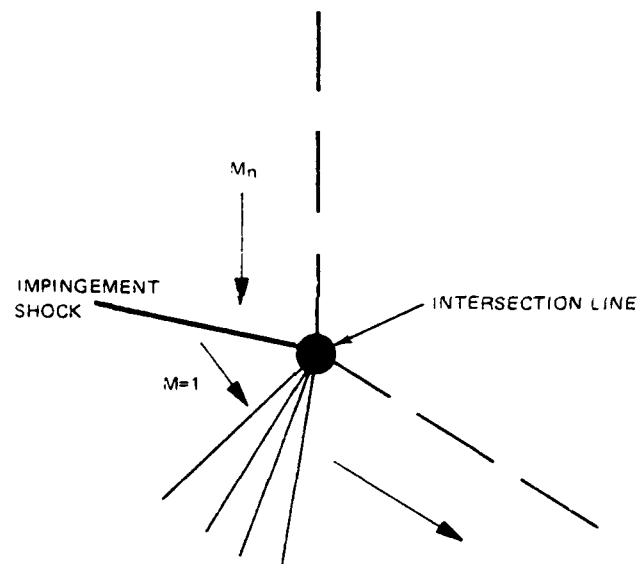for the Sample Calculation

Fig. 5-16. Details of Impingement Shock/Plume Boundary Interaction

fundamental unknown in the calculation of this point is the speed of the impingement point. The calculation procedure is similar to ordinary shock points. Flow properties behind the impingement shock are matched to the interior flow by a characteristic relationship in a local osculating plane. This procedure is an approximation and must be examined in the light of the more accurate flow solutions that are discussed in Section 6.

The isobars for the cross section in Fig. 5-15 show that the flow has nearly the undisturbed two dimensional impingement shock value at the centerline (see Fig. 5-17). The decay to background pressure takes place across the entire flow and is most rapid in the vicinity of the shock/boundary intersection point. Figure 5-17 shows the symmetry plane pressure profile and the cross sectional view $z = 2.12$ (the plume half width is unity). There is a region of near constant pressure developing at the outer fringes of the pressure boundary as would be expected. There are some "wiggles" in the pressure in this zone that are most probably due to the low number of mesh points used in the calculation (Fig. 5-15 shows the exact mesh employed). Figure 5-18 (a) shows the calculated development of the cross sections for the impingement region as a function of distance downstream of the impingement line. Each profile is ten calculation steps from the previous; the first being at Step 10. The pressure boundary develops into a pointed shape. Figure 5-18 (b) shows the flow profiles superimposed on the computational mesh. The impingement shock, pressure boundary and interaction cell have crossed many mesh points and have attained a variety of configurations with no apparent breakdown of the scheme. An interesting comparison is made in Fig. 5-19 with calculations reported in Ref. 5-11. The calculations are for the
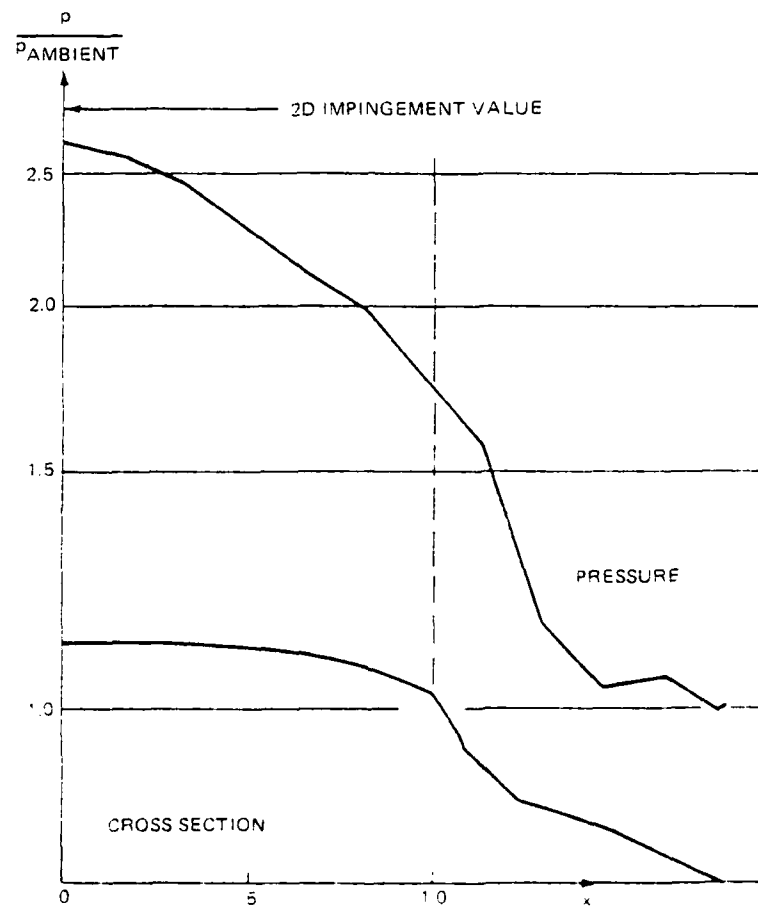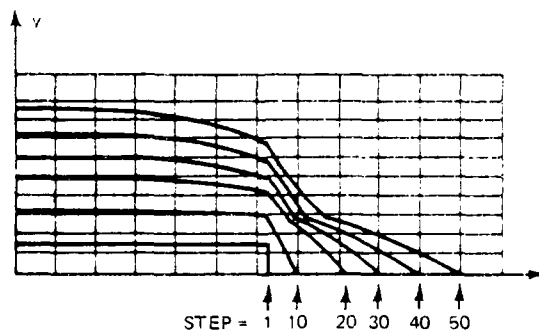
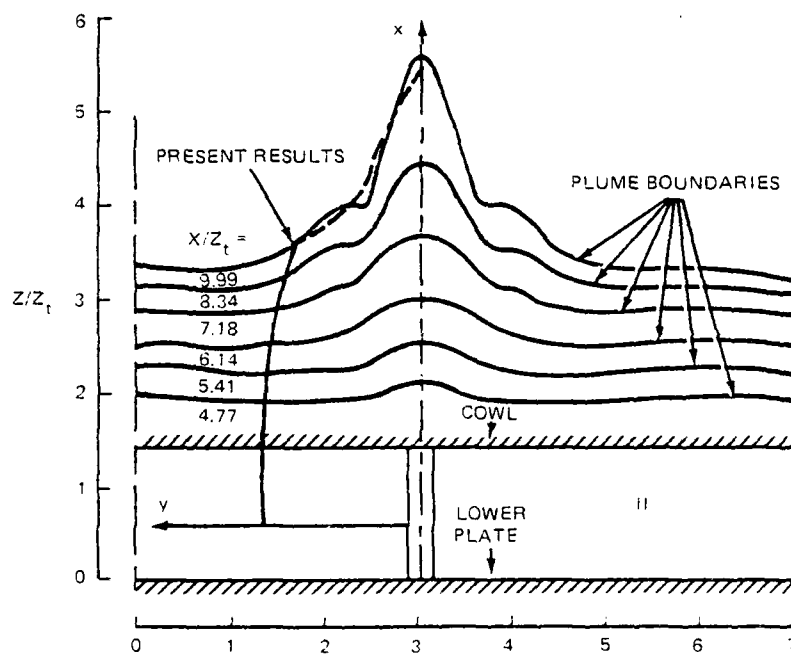Fig. 5-17 Computed Symmetry Plane Pressure Profile z = 2.12

2193-032D
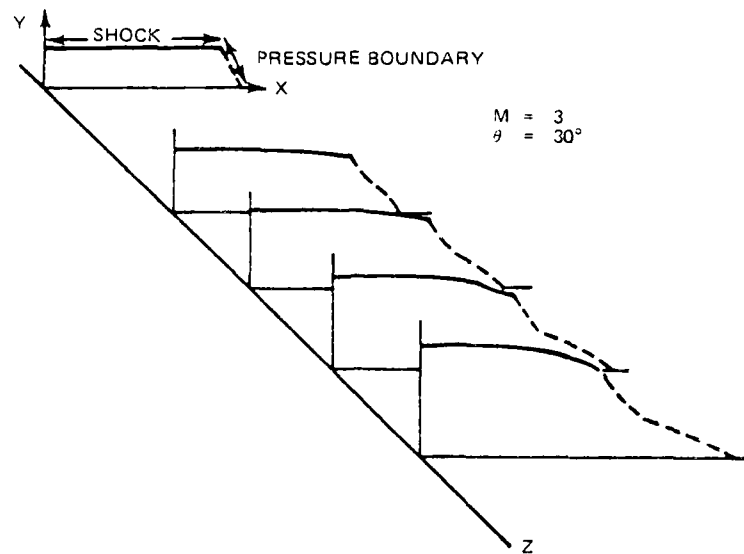
(A)   FLOW CROSSECTIONS

B)   COMPUTED BOUNDARY PROFILES CROSSING
THE FINITE DIFFERENCE MESH

Fig. 5-18.   Computed Development of the Flow Pattern for the
Impingement of Two Rectangular Plumes

Fig. 5-19 Comparison of Present Results with Scramjet Plume Calculation

2193-068D

plume boundary of a scramjet exhaust employing a shock capturing technique. The splitter plate produces impingement shocks similar in geometry to those in the present calculation. The comparison which is meant to be qualitative, is quite striking in that even the irregular shape of the boundary is reproduced. This gives some confidence in the present results, however, further comparison with other three dimensional flow calculations would be useful.

REFERENCES

5-1   Moretti, G., "Floating Shock Fitting Technique for Imbedded
       Shocks in Unsteady Multidimensional Flow," Proceedings of the
       1974 Heat Transfer and Fluid Mechanics Institute, Stamford
       University Press, 1974.

5-2   Moretti, G., "Three Dimensional, Supersonic, Steady Flows with
       any Number of Imbedded Shocks," AIAA Paper No. 74-10, Jan.
       1974.

5-3   Salas, M., "The Anatomy of Floating Shock Fitting" AIAA
       Second Computational Fluid Dynamics Conference, June 19-20,
       1975.

5-4   Mac Cormack, R., "The Effect of Viscosity in Hypervelocity
       Impact Cratering," AIAA Paper No. 69-354, May 1969.

5-5   Ferri, A., Elements of Aerodynamics of Supersonic Flow,
       MacMillan Co., N.Y. 1949.

5-6   Rakich, J.V. and Cleary J.W., "Theoretical and Experimental
       Study of Supersonic Steady Flow Around Inclined Bodies of
       Revolution", AIAA Paper No. 69-187, 1969.

5-7   Moretti, G., "Three Dimensional Supersonic Flow Computations,"
       AIAA Journal Vol 1, No. 9, 1963.

5-8   Rudman, S., "Numerical Study of Highly Underexpanded Three
       Dimensional Plumes" ATL TR 184, Advanced Technology Labs,
       Westbury, New York, June 1973.

5-9   Del Guidice, P., "Three Dimensional Nozzle Flow Fields by a
       Reference Plane Technique - Including the Effects of Equilibrium
       Hydrogen-Air Chemistry" Ph.D. Thesis, New York University,1972.

5-10   Frohn, A., "An Analytical Characteristics Method for Steady
       Three Dimensional Isentropic Flow," Journal of Fluid Mechanics,
       Vol. 63, Part 1 pp 81-96, 1974.

5-11   Dash, S., and Del Guidice, P., "Shock Capturing Finite
       Difference and Characteristic Reference Plane Techniques
       for the Prediction of Three Dimensional Nozzle-Exhaust
       Flow Fields," ATL TR 243 Advanced Technology Labs, Westbury, N.Y.,
       March 1977.

SECTION 6

THREE DIMENSIONAL PHENOMENA

In Section 3 the flow pattern of two underexpanded interacting rocket
plumes was discussed and the general features of the possible flow fields were
pointed out. In this section the intersection of two three dimensional shock
surfaces and the impingement shock liftoff will be analyzed. These features
have no counterparts in two dimensional supersonic flow. In both situations
there is an abrupt change in configuration because attached shock solutions
are no longer viable. The configurational change takes place through a
conical solution centered at the transition point. Detailed understanding of
the nature of these transitions and the ability to compute them accurately is
required in the subject problem. Many other three dimensional supersonic flows
of current interest require understanding of the shock intersection problem
and other three dimensional features which are peculiar to those problems.
These transition problems are generally complex. The shock wave pattern
formed by two intersecting wedges is an example of a similar conical flow that
is less complex than the two transitions being considered. The computation of
the "corner flow" problem has been the subject of research for many years and
is the subject of several papers (Refs 6-1 to 6-3) and was recently the
subject of a Ph.D. thesis (Ref. 6-4)).

The intersection process that occurs between two three dimensional shock
surfaces will be discussed first . A single three dimensional shock surface
has a certain amount of arbitrariness in its description that does not exist
in the two dimensional counterpart. In both cases, the jump conditions for

the thermodynamic state variables can be reduced to the one dimensional Rankine-Hugoniot relationships employing the Mach number normal to the shock wave (defined by velocity component normal to the wave and the undisturbed sound speed). The tangential component of the oncoming velocity vector is unchanged by the shock wave. In two dimensions, this leads to an unambiguous relationship between pressure ratio and flow deflection across a shock wave and the definition of a shock polar. In three dimensions, it is possible to arbitrarily decompose the tangential velocity vector into two components in the surface of the wave. One of these components can be combined with the normal velocity component to form a velocity vector oblique to the wave. The jump condition, for the thermodynamic variables, can be determined by the corresponding two dimensional oblique shock relationships. The velocity downstream of the shock surface is found by adding to the oblique shock solution the remaining component of tangential velocity (which is unchanged by the wave). Because the decomposition of the tangential velocity vector is arbitrary, a three dimensional shock wave surface can be described by an infinity of two dimensional oblique shocks with an additional tangential velocity component. For a given surface normal vector to the shock the downstream result is always identical.

The intersection of two shock waves in three dimensional flow takes place along an intersection line whereas the two-dimensional counterpart takes place at a point. The properties of the interaction depend not only on the shock strengths but also the local orientation of the intersection line. When the flow is supersonic downstream of the interaction the intersection line is at the leading edge of the transmitted and reflected waves. The transmitted and

reflected waves originate at the intersection line in the same manner the attached shock surfaces originate at the leading edges of swept wings in supersonic flow. Thus the sweep of the intersection line plays a strong role in the interaction. Because a three dimensional shock surface can cause flow deflection in any azimuthal direction it cannot be simply described as a first (upward deflection) or a second (downward deflection) "family" shock as a two dimensional shock can. In two dimensional flows the intersection of two shock waves can be categorized according to whether both shocks are of the same or opposite family. In either case there are a variety of shock configurations that can result and the subject is an established segment of supersonic flow theory (see, for example, Refs. 6-5,6). While a three dimensional shock cannot be described simply as belonging to one of two families, the interaction process of two shock surfaces can still be categorized in this manner. At a point along the intersection line each of the two waves can rotate the flow in the same direction or in opposite directions relative to an imaginary axle parallel to the intersection line. Thus, the simple classification employed in the two dimensional theory can be employed locally for three dimensional shock surfaces.

In the following discussion the evolution of a three dimensional shock/shock interaction process is elucidated by considering the model problem of a circular conical shock intersecting a planar shock surface. This model problem has the highly desirable feature of constant shock strengths (in terms of pressure ratios) at all points along the geometric intersection line which is a true hyperbola. The case considered here has a regular reflection process at the leading edge of the intersection line. When viewed along the

intersection line, the initial interaction is locally that of two same family shock waves intersecting and there is a simple transmitted and reflected wave pattern. Downstream of the leading edge the sweep angle of the intersection line increases, giving rise to decreasing apparent normal Mach numbers and increasing apparent deflection angles so that at some point the simple regular reflection process is no longer possible. A detailed discussion of the reasons for this is given employing the shock polar diagrams in the pressure/deflection plane. A Mach (or irregular) reflection process develops in which an additional shock segment bridges the span between the two incoming waves. This shock segment moves ahead of the geometrical intersection of the two incoming waves and there are now two shock triple points characterizing the intersection. The cross flow behind this additional shock segment is subsonic relative to the triple points and is analogous to the Mach reflection that develops in the three dimensional compression corner flow field. The propagation of an irregular reflection pattern thus involves the intersection of three shock surfaces - the two incident waves and the Mach reflection wave which is generated by the intersection.
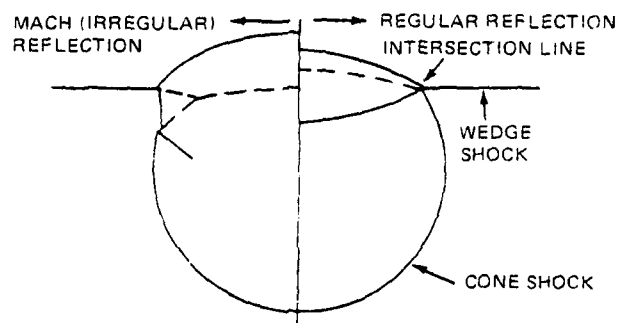
The complex nature of the intersection of shock wave surfaces in three dimensional flows can be illuminated by considering the model flow configuration shown in Fig. 6-1. A thin wedge in a supersonic stream produces a supersonic oblique planar shock surface and a uniform flow parallel to the wedge. A cone is aligned with this flow giving rise to a conical shock surface. The conical shock and the planar shock intersect along a hyperbolic line in the plane of the oblique shock (Fig. 6-1(b)). In cross-sectional view, the circular conical shock intersects the planar oblique shock at two

WEDGE SHOCK   CONE SHOCK

q^∞

q_w CONE
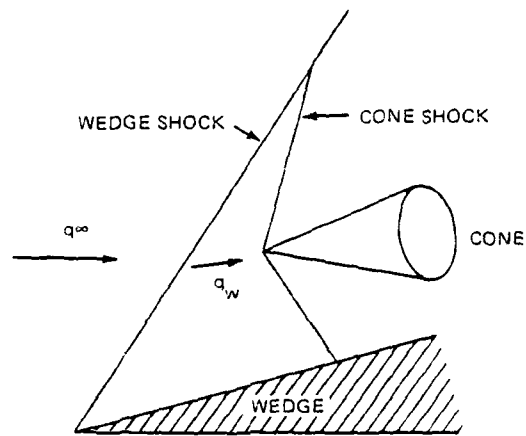
WEDGE

a) SCHEMATIC OF FLOW FIELD

ϕ_∞

ϕ
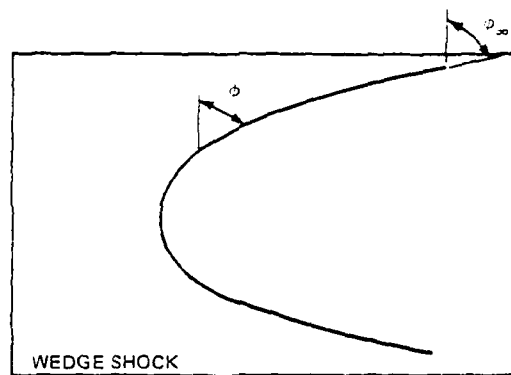
WEDGE SHOCK

b) INTERSECTION LINE IN PLANE OF THE
   WEDGE SHOCK

MACH (IRREGULAR)   REGULAR REFLECTION
REFLECTION   INTERSECTION LINE

                          WEDGE
                          SHOCK

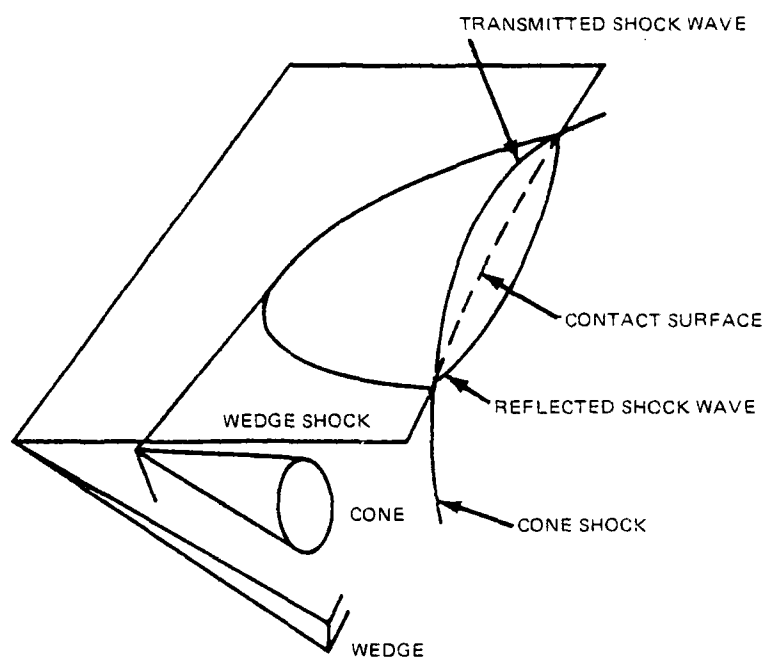   CONE SHOCK

c) CROSS SECTIONAL VIEW OF SHOCK SYSTEM

2193-034D

Fig. 6-1 Intersection of a Planar Wedge Shock and a Circular
          Conical Shock

points. The wave system that joins these two points can be characterized as either a simple transmitted and reflected wave system (regular) or a more complex system containing the equivalent of a Mach reflection (irregular). These are shown on the right hand side and left hand side of Fig. 6-1(c) respectively. The pattern that prevails (regular or irregular) depends on the location along the intersection. Initially, the sweep angle is zero and the interaction is regular (for the cases considered here with supersonic downstream velocity). Downstream, as the sweep angle increases, a transition occurs and the shock pattern becomes irregular. In the regular reflection a local two dimensional flow analysis centered on the intersection line can be employed to determine the local solution. There is a simple transmitted and reflected wave and contact surface that leaves the point of intersection (right-hand side of Fig. 6-1(c). The cross flow relative to the intersection line behind the reflected/transmitted waves is supersonic. Therefore, the intersection line can be viewed as the leading edge of these shocks and the solution is independent of downstream properties . In the Mach (irregular) reflection case, the resulting shock system is actually ahead of the geometrical intersection of the cone and wedge shocks (left hand side of Fig. 6-1(c). There are now two shock triple points, and the cross flow is, in general, subsonic; thus, flow properties from the high pressure side determine the propagation velocity.

In the case of the regular reflection (shown schematically in Fig. 6-2, the solution is arrived at by decomposing the free stream velocity into the components normal and tangential to the intersection line. The tangential component of velocity is parallel to all the wave surfaces by virtue of the

TRANSMITTED SHOCK WAVE

CONTACT SURFACE

REFLECTED SHOCK WAVE

WEDGE SHOCK

CONE

CONE SHOCK

WEDGE

2193-035D

Fig. 6-2 Isometric View of Regular Shock Pattern for
the Wedge-Cone Shock System

geometry of the intersection. Figure 6-3 details a point along the intersection line showing the two incoming waves and the transmitted and reflected wave surfaces. In the plane containing the normal component of velocity (Fig. 6-4), the flow pattern is identical to that of the two-dimensional flow containing the intersection of two shock waves of the same family. The incident shock waves are known in strength and do not interact until they intersect (the flow behind them is supersonic). The solution for the transmitted and reflected wave strength is achieved by determining the deflection of the contact surface δ_3 (Fig. 6-4) to match the pressures in regions (3) and (4) behind the transmitted and reflected waves, respectively. This can be achieved by a simple iteration procedure. The process is best understood by studying the flow process in the pressure/flow deflection hodograph plane (Fig. 6-5). Each point on curve I, the shock polar associated with the upstream velocity (the velocity component normal to the intersection line in the three-dimensional case) corresponds to conditions on the high pressure side of the shock wave. The entire polar corresponds to all shock wave angles ranging from the local Mach angle to a normal shock (for both positive and negative deflections). The pressure in zone (1) is determined simply by moving to the deflection δ_1, on the abscissa. For the Mach number of the flow, in zone (1) a shock polar, curve II, can be constructed at point (1), and the pressure at (2) is determined corresponding to the deflection δ_2. The shock polar at point (2), curve III completes the solution. Polars I and III intersect at a point which is denoted as point (3) along polar I and (4) along III. Points (3) and (4) are coincident in the pressure/deflection plane but represent different velocities and entropy (or
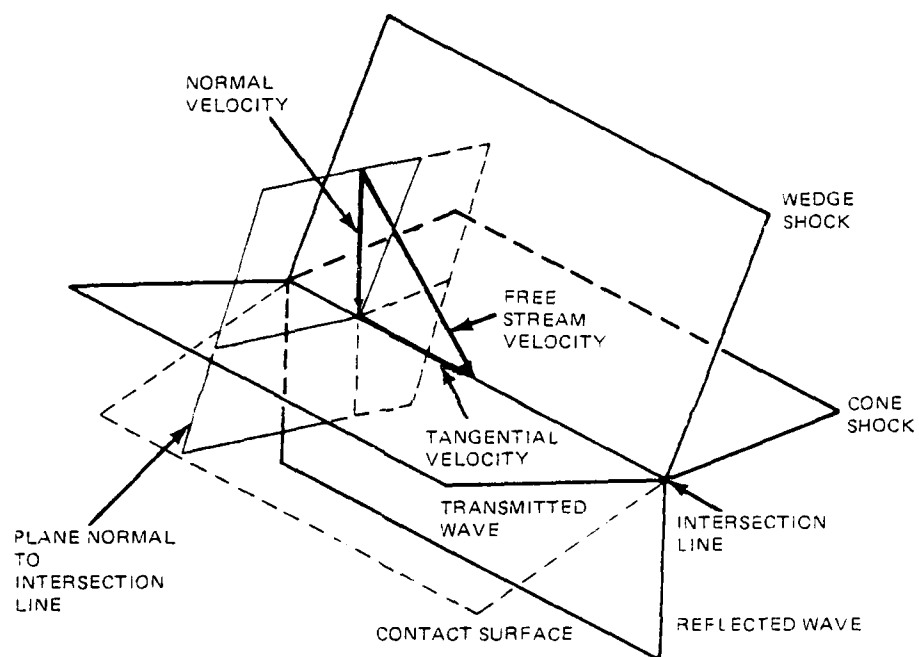
2193-036D

Fig. 6-3 Details of Regular Intersection Pattern of the Wedge
Shock and Cone Shock Along the Intersection Line

WEDGE SHOCK

CONE SHOCK

δ_1

TRANSMITTED
WAVE

2

δ_2

δ_3
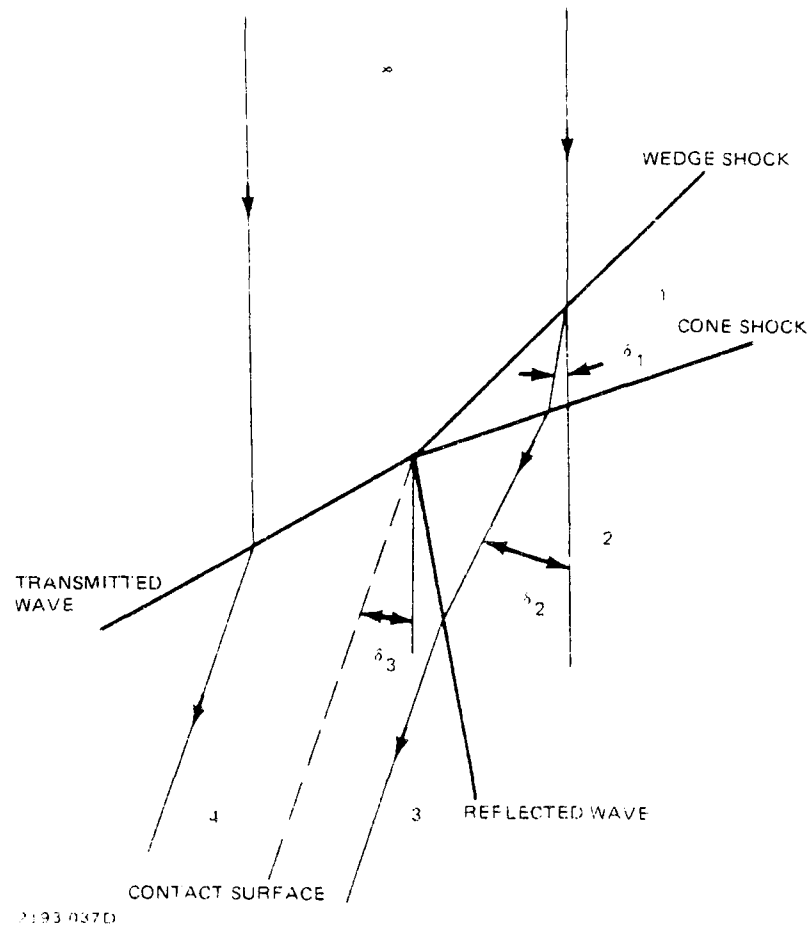
REFLECTED WAVE

3

CONTACT SURFACE

Fig. 6-4 Regular Shock Reflection Pattern in the
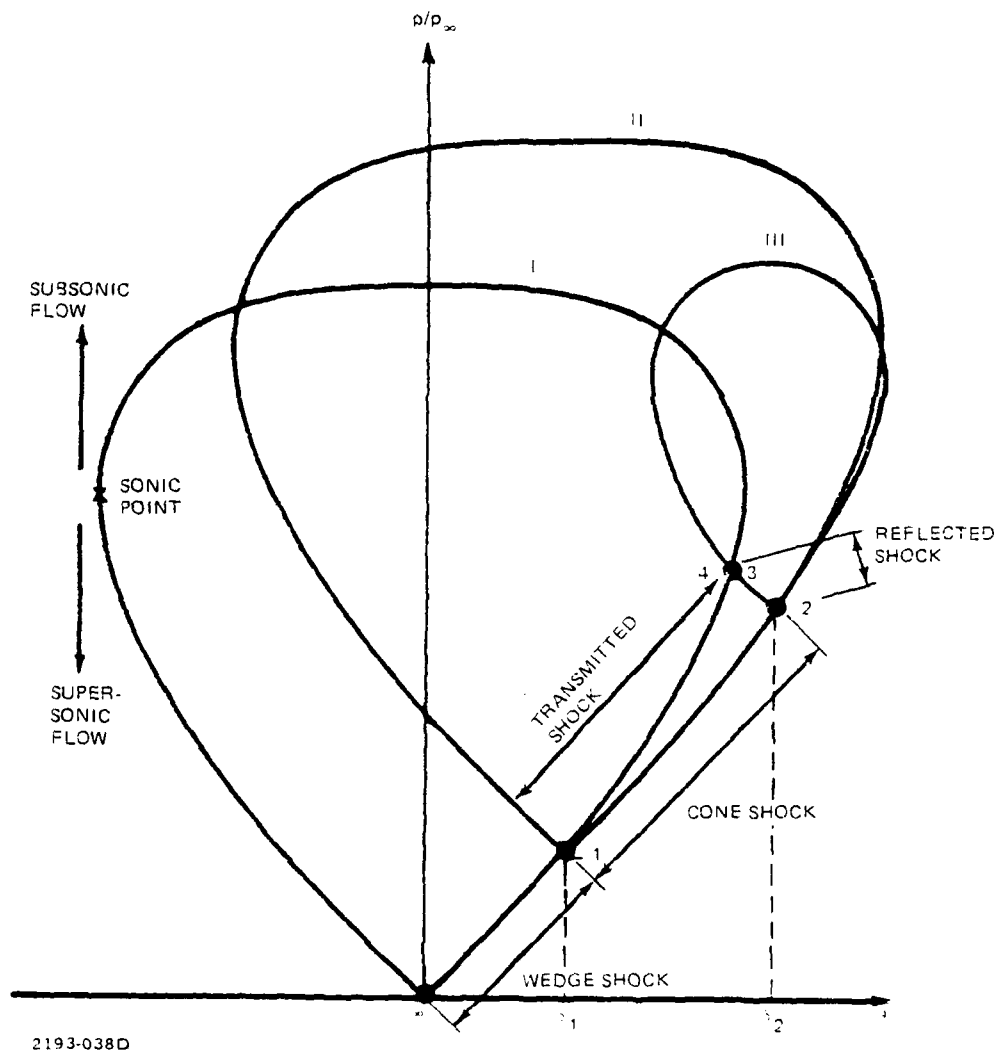Plane Normal to Intersection Line

Fig. 6-5 Pressure Deflection Plane Showing Shock
Polar Configuration for Regular Reflection

2193-038D

density). By the nature of the construction, point (3/4) is at the desired
condition which brings the flow behind the transmitted and reflected waves to
identical pressures and flow deflections. The regular wave system depicted in
Fig. 6-5 has a weak compression wave (the arc (2) - (3)) as the reflected
wave.

The reflected wave between polars I and II can be an expansion or
compression wave depending on the orientation of polars I and II. There are
four possible intersection patterns of polars I and II (Refs. 6-5, 6-6) shown
in Fig. 6-6 that are characterized by the number of points the two curves
intersect. Whenever point (2) on polar II (see Fig. 6-5) is at a lower
pressure than a point on curve I for the same deflection, the reflected wave
is a compression (shock) as described in the preceeding paragraphs. However,
in the $m = 0$, $m = 2$ and a portion of the $m = 3$ case (m is the number of
intersection points of the two curves), the geometry is reversed and the
solution for the reflected wave is a simple centered expansion, as shown in
Fig. 6-7. It can be shown (Refs. 6-5, 6-6) that the intersection pattern is
dependent on free stream Mach number and deflection angle δ_1, (as well as
the ratio of specific heats for the gas). In any of these cases the wave
pattern becomes irregular when the shock polar III does not intersect polar I
(or in the case of a reflected expansion wave when the characteristic curve
does not intersect I). The simple all supersonic (cross) flow pattern
associated with the regular reflection is no longer possible and a more
complex pattern emerges.

In the model flow problem for specified cone and wedge angles and free
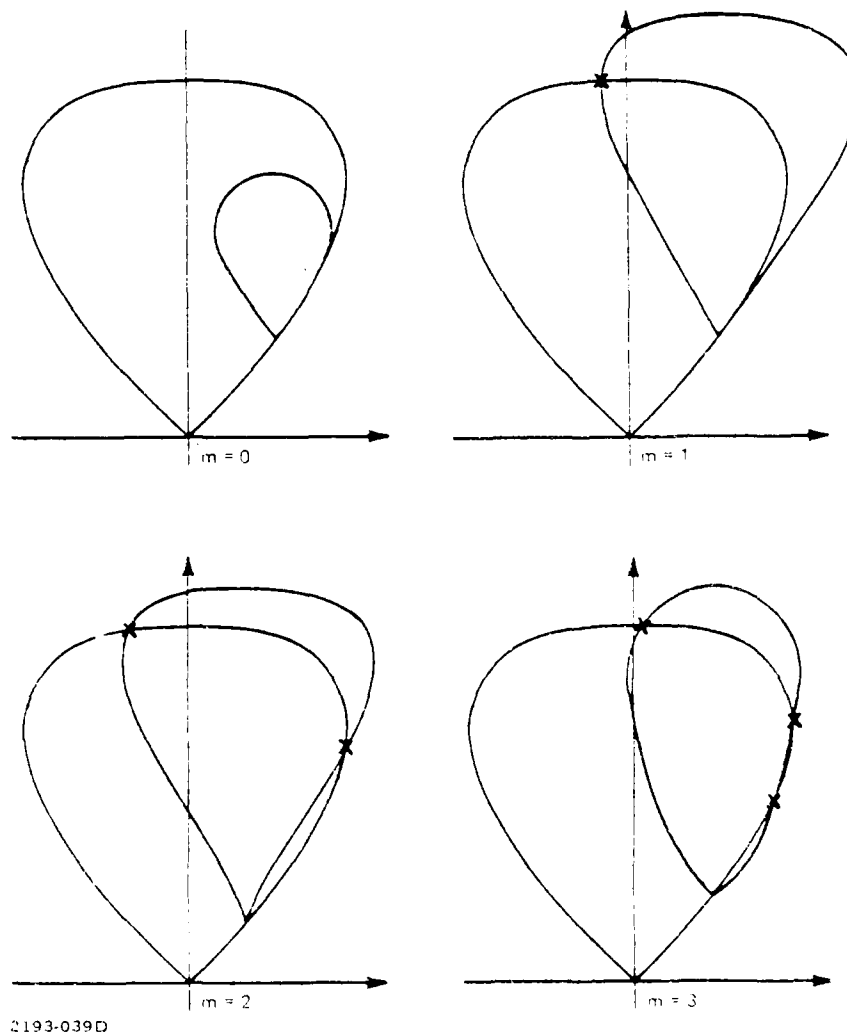stream Mach number (the conical/wedge shock intersection problem), the local

2193-039D

Fig. 6-6 The Four Possible Configurations for Two
Shock Intersections

END
DATE
FILMED
5-81
DTIC

AD A
097244

MICROCOPY RESOLUTION TEST CHART

∞

WEDGE SHOCK

CONE SHOCK
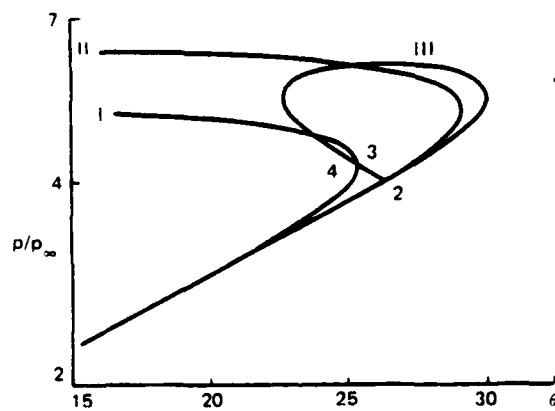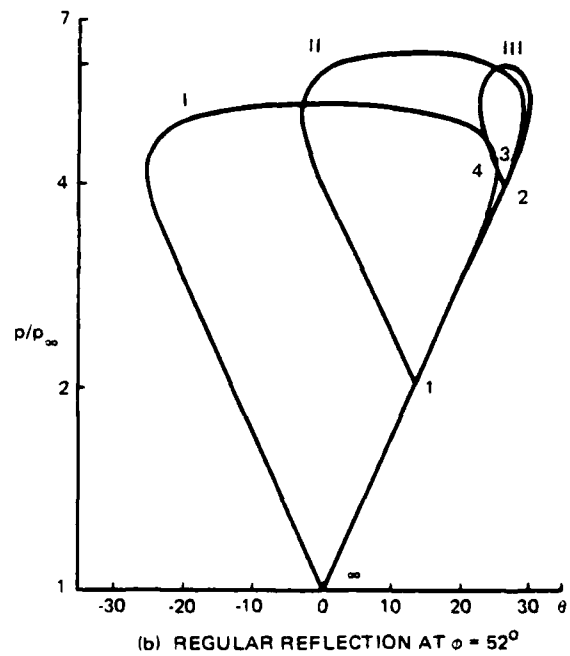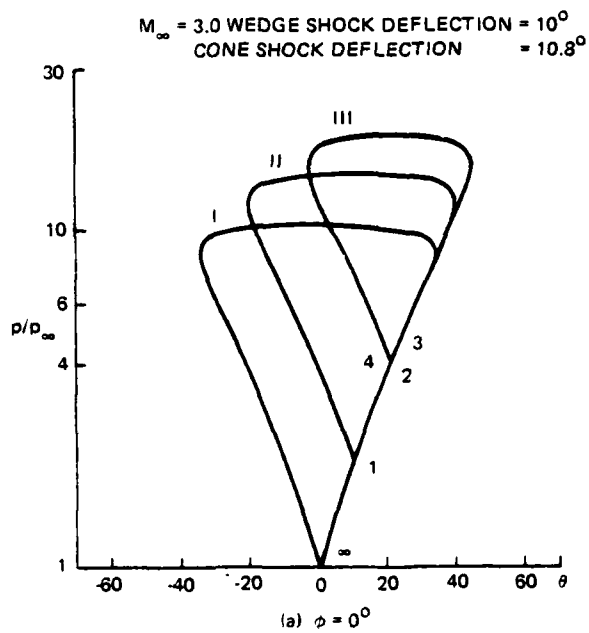
1

TRANSMITTED
WAVE

4

2

3

REFLECTED EXPANSION WAVE
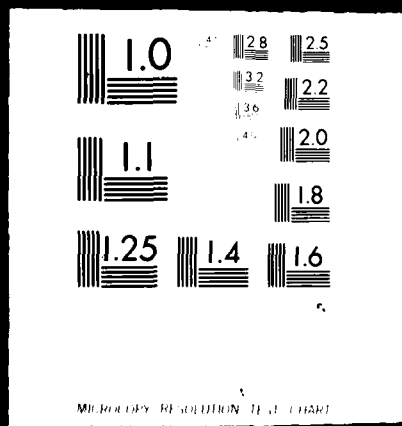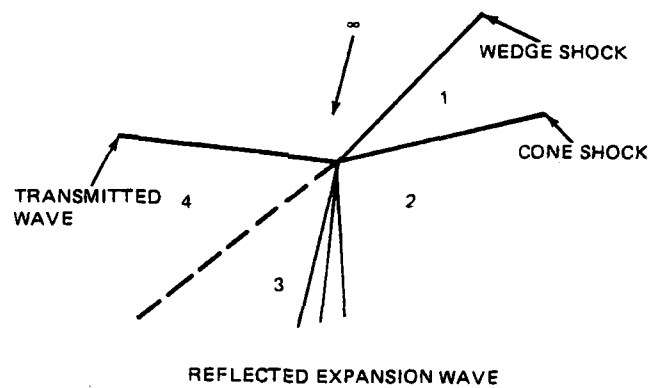
2193-040D

Fig. 6-7 Regular Shock Intersection with a Reflected
Expansion Wave

solution depends solely on the sweep angle (see Fig. 6-1) of the intersection line. This is because the pressure ratios across each shock wave are constant and independent of location. In addition the apparent deflections through the two incoming waves as well as the governing Mach number normal to the intersection line are all functions of the sweep angle because the flow is uniform upstream of the wedge shock. Evolution of the shock system transition from regular to irregular is illustrated in Fig. 6-8. These figures detail the shock polars for the following conditions: M_∞ = 3.0, γ = 1.4, wedge angle 10°, wedge pressure ratio p_W/p_∞ = 2.054, cone angle θ_c = 20°, cone pressure ratio p_c/p_W = 1.95 or p_c/p_∞ = 4.005, (see Fig. 6-1 for definitions). The asymptotic sweep angle of the intersection line (ϕ_∞) is 60°. Figure 6-8a is the pressure/deflection plane for the initial intersection of the shocks (ϕ = 0). In this case the polars are very close together and the reflected wave is a very weak expansion wave which cannot be seen on the scale of the figure. Downstream along the intersection line Fig. 6-8b shows the shock polar pattern for ϕ = 52°. Note that while the polar patterns are considerably different, the pressure at points (2) and (3) which are the wedge and cone shock pressures are the same as the ϕ = 0° case. At this sweepback angle, ϕ = 52°, the normal Mach number to the intersection line has decreased to 2.15 from the free stream value of 3.0. The apparent wedge and cone shock deflection angles which were 10° and 20.8° initially are now 13° and 26.2°, a geometric result of projecting the flow fields onto the plane normal to the intersection line. The decreased normal Mach number and increased apparent deflection moves the solution toward the upper right hand corner of polar I. A closeup of this upper right hand portion of Fig. 6 -8b

M∞ = 3.0 WEDGE SHOCK DEFLECTION = 10°
CONE SHOCK DEFLECTION = 10.8°

(a) φ = 0°

(b) REGULAR REFLECTION AT φ = 52°
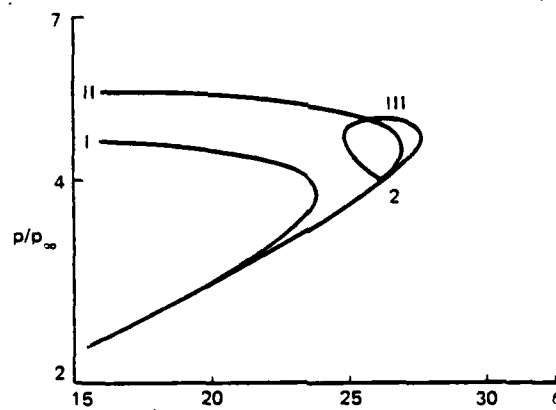
(c) DETAILS OF SHOCK POLAR CROSSINGS FOR φ = 52°

2193-041D(1/2)

Fig. 6-8 Pressure Deflection Diagram for the Intersection of a
Conical Shock and a Wedge Shock (Sheet 1 of 2)
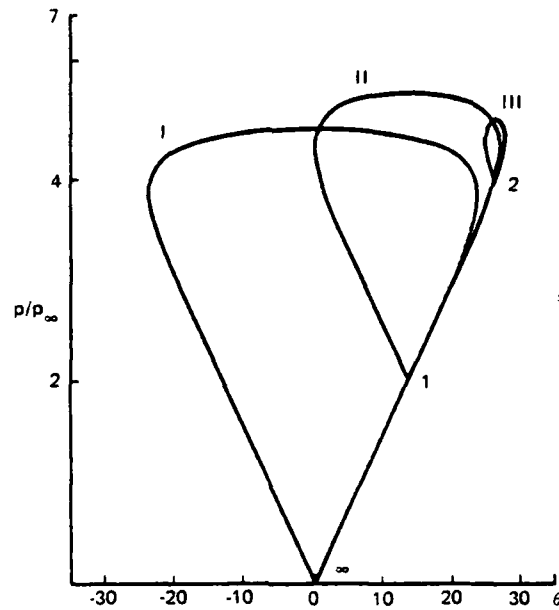
(d) MACH REFLECTION AT ϕ = 55°

(e) DETAILS OF SHOCK POLAR CROSSINGS FOR ϕ = 55°

2193-041D(2/2)

Fig. 6-8 Pressure Deflection Diagram for the Intersection of a
Conical Shock and a Wedge Shock (Sheet 2 of 2)

is shown in Fig. 6-8c. This case is interesting because point (4), the flow behind the transmitted wave, is on the subsonic portion of polar I. The cross flow becoming subsonic is a signal that there is an incipient change in structure. In fact, a small distance downstream where $\phi = 55°$ (Fig. 6-8d) polar III no longer intersects polar I, and the regular four wave pattern that had prevailed is now not possible. A closeup of the interesting portion of this figure is shown in Fig. 6-8e*

The subsequent flow pattern is characterized by a five-wave intersection made up of two three wave intersections, as shown in Fig. 6-9a. This shock pattern is qualitatively similar to the one that prevails in the internal compression corner flow field (Refs 6-1,2,3,4). The major qualitative difference is that the two contact surfaces forming the triangular zone behind the Mach reflection shock meet at a point, denoted b on Figure 6-9a, on a contact surface. In the compression corner flow field this point is in the corner. It is not possible to characterize the entire interaction by a single shock polar pattern because there are now two intersection lines. However, in order to visualize the process the velocity field normal to the interaction is approximated as constant and uniform. In Fig. 6-9b the flow in the pressure /deflection plane would then be as follows (Ref. 6-6) describes the two dimensional counterpart): (a) points (1) and (2) are at the wedge and cone shock pressures as before; (b) shock polars I and II intersect in only one place (for this case) and that determines the pressure and deflection at the

---

* The change in structure might come at the point where the cross flow becomes sonic. It is not clear at present exactly where the transition occurs.
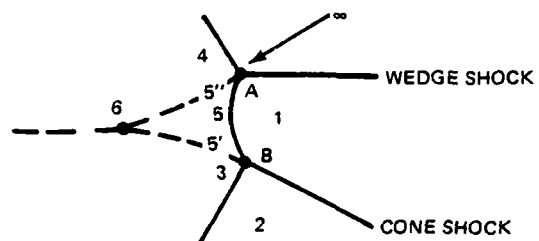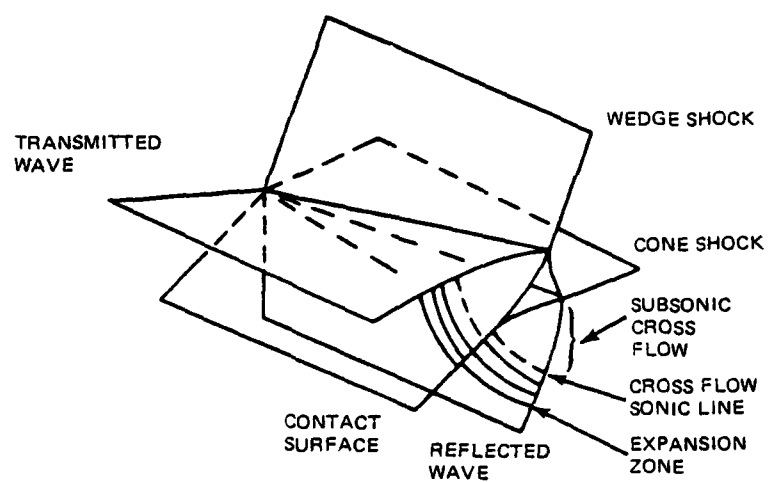
(a) SHOCK PATTERN
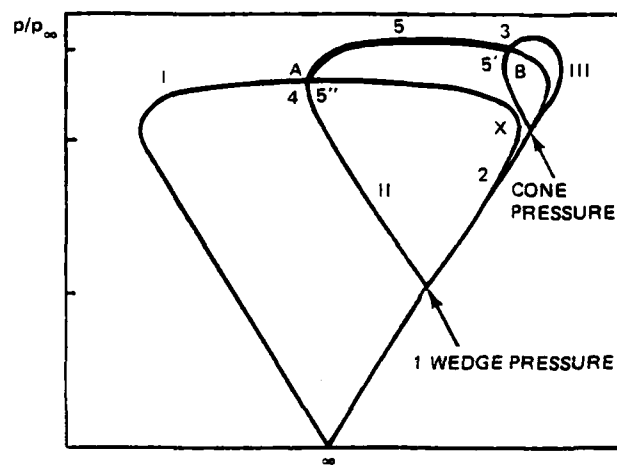
(b) PRESSURE/DEFLECTION PLANE

2193-042D

Fig. 6-9 Mach Reflection for Wedge/Cone Shock Intersection

intersection line labeled A; (c) a similar process takes place at intersection
B - the junction of zones (1), (2), (3) and (5) - where B (in Fig. 6-9b)
represents the only possible shock transition starting from conditions (1) and
(2); and (d) where the segment of the shock wave between A and B is a curved
shock (shown as a bold line in Fig. 6-9b).

A schematic of the expected transition pattern is shown in Fig. 6-10.
Relative to the transition or breakup point the flow is conical in nature.
The cross flow is subsonic in the zone immediately behind the shock
interaction and is thus governed by elliptic partial differential equations.
Thus the propagation speeds of the two triple points leaving the transition
zone can only be determined as part of the solution of the entire transition
zone. An interesting and important aspect of the flow pattern is that the
pressure levels prevailing behind the interaction shocks are higher than the
levels attained by the regular reflect pattern just before it breaks apart
(shown as the X on polar I in Fig. 6-9b). Thus, at the point along the
intersection line where the shock pattern transitions from regular (four-wave)
to irregular (five-wave) the flow pattern must include a three dimensional
expansion zone immediately behind the shock wave to equilibrate the pressure.
Again the strength and distribution of this expansion zone are determined as
part of the complete solution of the transition zone.

The(impingement) shock lift off problem is another three dimensional
transition problem that occurs in the multinozzle flow field. Between
stations denoted by 0 and 1 Figure 3-2(a) is the initial portion of the
impingement flow field and the origin of the impingement shock surface. The
flow pattern in this region can be studied by examining the simpler flow in

TRANSMITTED WAVE

WEDGE SHOCK

CONE SHOCK

SUBSONIC CROSS FLOW

CROSS FLOW SONIC LINE

CONTACT SURFACE

REFLECTED WAVE

EXPANSION ZONE

2193-043D

Fig. 6-10 Shock Wave Pattern in the Transition Zone
from Regular to Mach Reflection

which two uniform circular jets impinge. Figure 6-11 shows the overall flow
configuration (leaving out the interaction for clarity). Two circular jets
with uniform properties impinge at the symmetry plane. The intersection of
the plume boundary and the symmetry plane is an ellipse. The shock pattern
develops as is shown in an isometric view in Fig. 6-12. In the cases that are
considered here the shock wave is initially attached at the origin. The
initial shock pattern when viewed as cross sections have the appearance of arc
segments anchored at the ends to the intersection line. At some point along
the intersection line this pattern is no longer possible and the shock ends
lift off.

The shock pattern is shown in Figure 6-13 along with the details of the
flow at the shock leading edge. In a manner completely analogous to that
employed to determine the shock wave strength at the leading edge of a swept
wing in supersonic flow (c.f. Ref. 6-7) the shock is examined in a plane
perpendicular to the intersection line. Again the component of velocity
tangential to the intersection line is unaltered by the shock surface. These
sections appear adjacent to each cross section in Fig. 6-13 . Near the
leading edge the Mach number normal to the intersection is large enough and
the deflection (δ_1) small enough so that there is an attached shock
solution as shown by the adjacent pressure deflection shock polar diagram.
Downstream at station 2 the normal Mach number (M_{n2}) has decreased and the
apparent deflection δ_2 has increased. The shock polar has diminished in
size and the required deflection (δ_2) is getting near the maximum deflection
possible for M_{n2}. At station 3 the shock has already lifted off the
symmetry plane. This is required because at M_{n3} the deflection δ_3 cannot

6-22

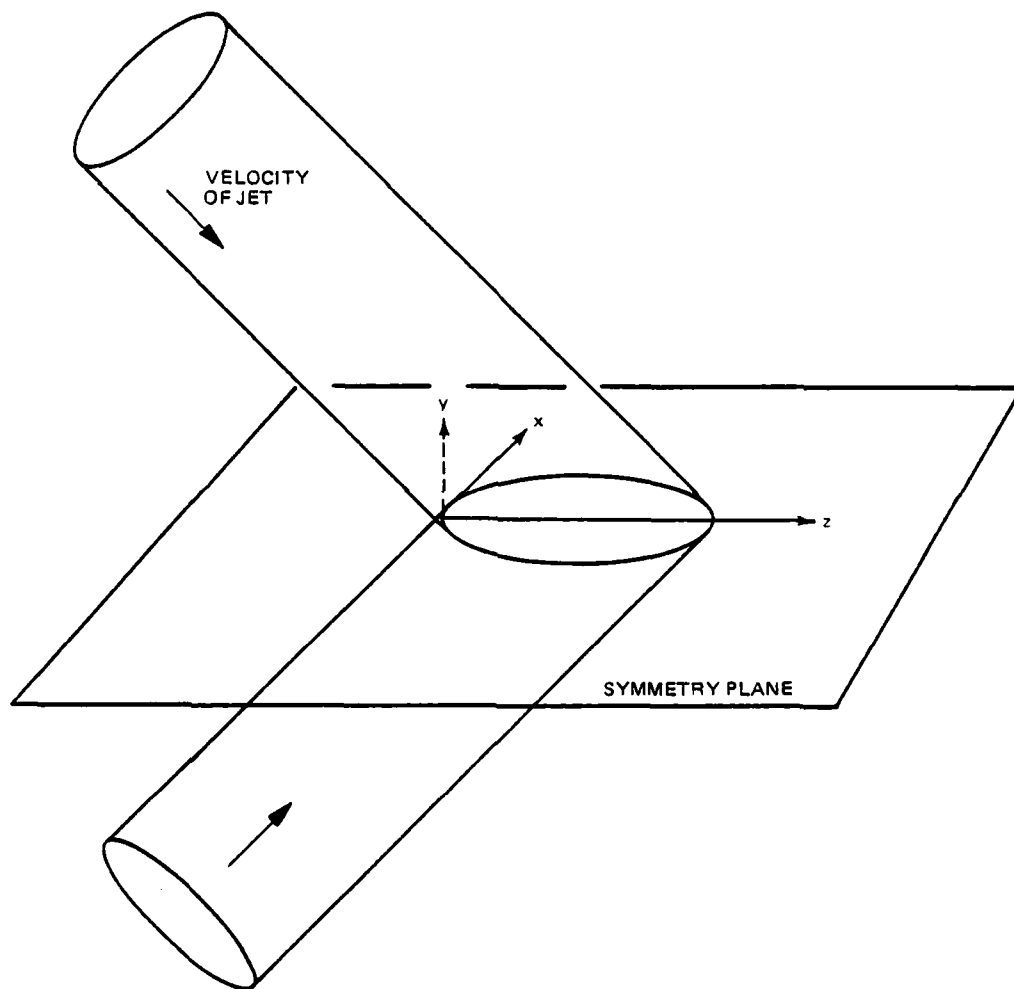**VELOCITY OF JET**

SYMMETRY PLANE

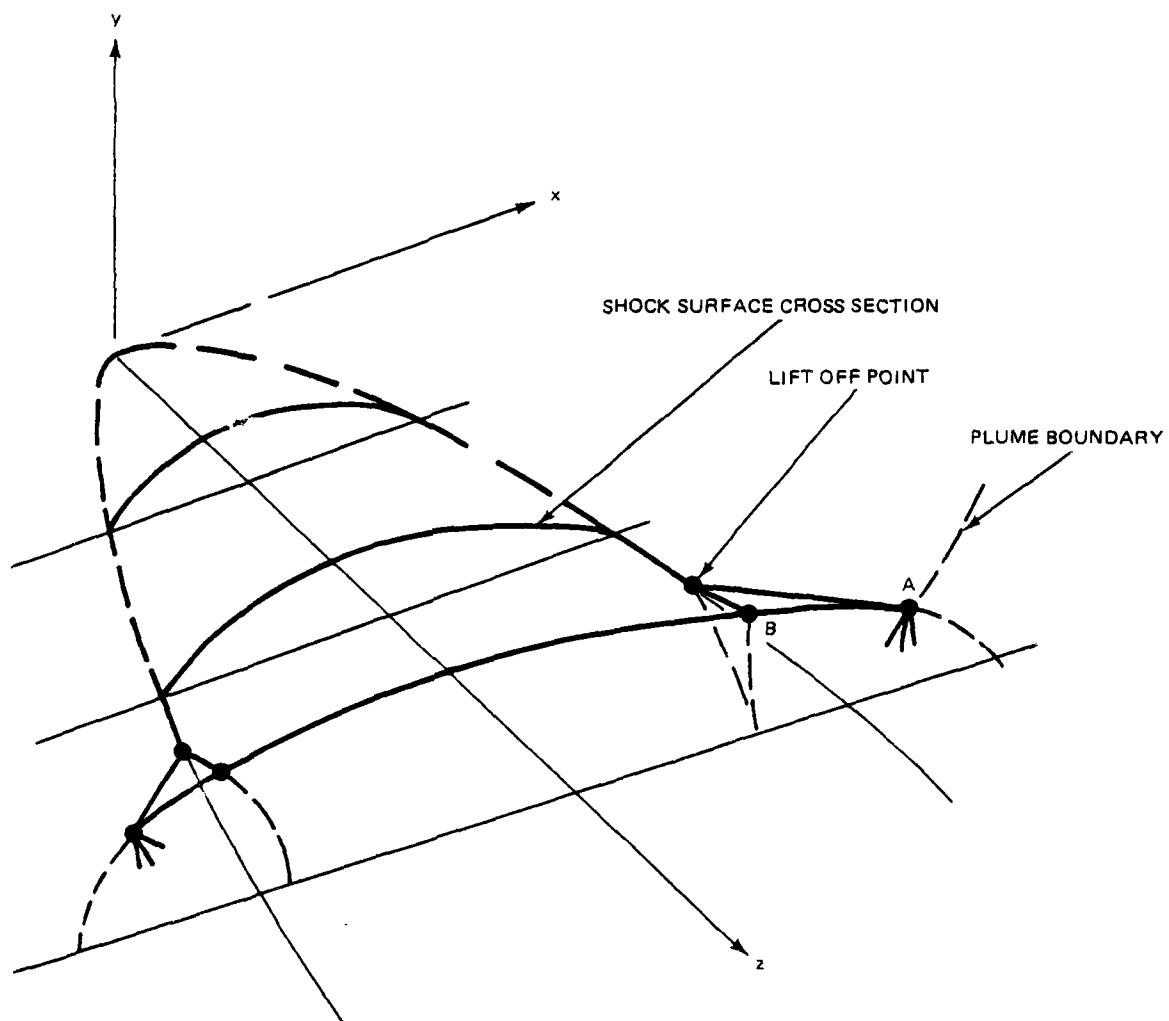Fig. 6-11 Schematic Diagram Showing the Intersection
of Two Circular Jets

Fig 6-12 Geometry of Initial Region of the Impingement Shock
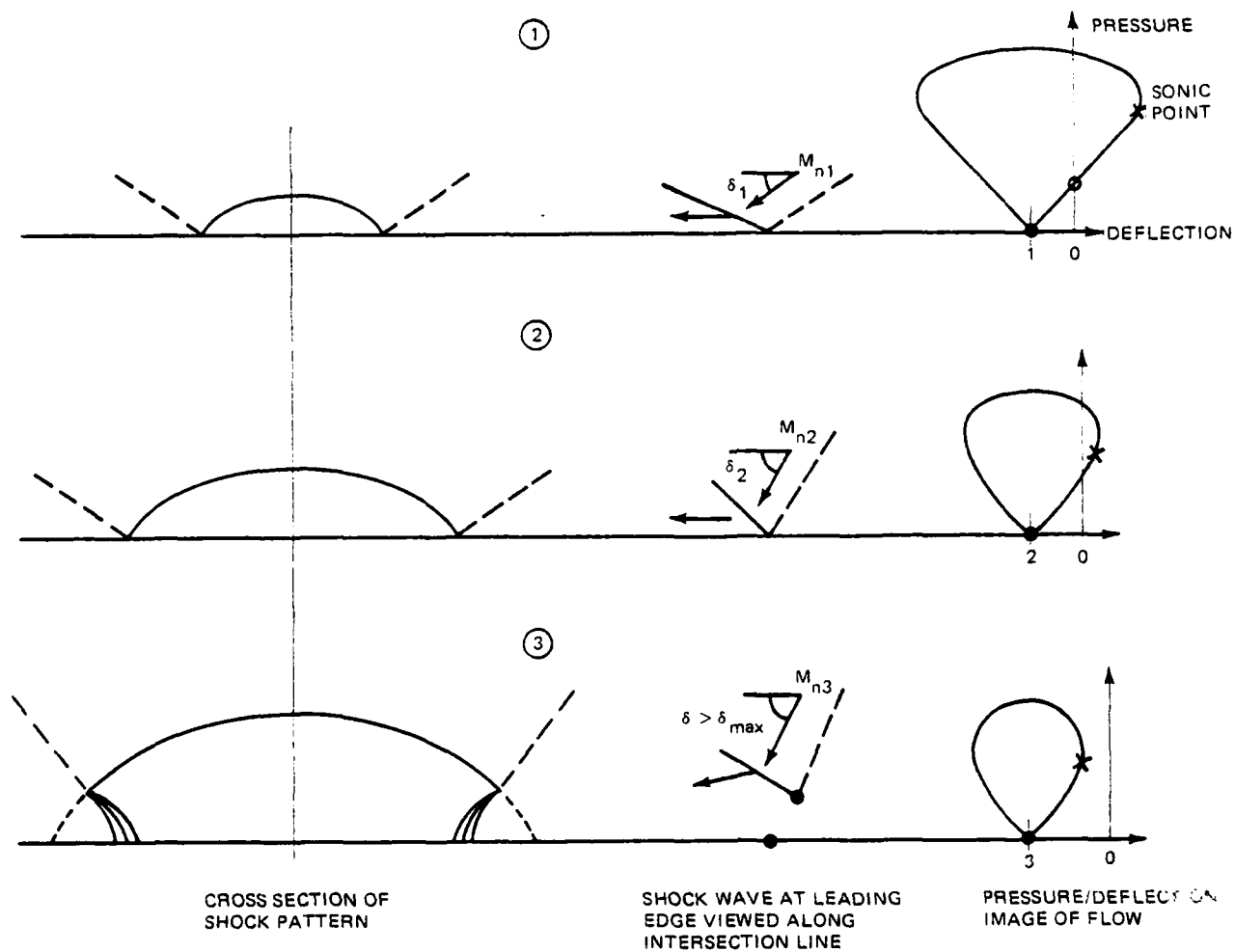for Uniform Circular Jet Impingement

6-24

Fig. 6-13 Cross Section Details of Impingement Shock and Corresponding
Hodograph Diagrams

be achieved by an attached shock. Note that M_{n3} and δ_3 are determined relative to the geometric intersection line of the plume and the symmetry plane. The actual leading edge of the shock wave moves up along the undisturbed plume boundary. The flow perpendicular to this leading edge or intersection line must be at least sonic (see Section 3) because the velocity must be supersonic to reexpand and match the pressure on the plume boundary.

In the neighborhood of the liftoff point the flow pattern is conical. With the liftoff point as the origin of a spherical coordinate system the flow pattern develops along spherical rays and is geometrically similar when scaled to the distance from the liftoff point. A schematic of this conical flow is shown in Fig. 6-14. The orientation and relative position of this pattern is shown in Fig. 6-12. The Mach cone that leaves the liftoff point limits the extend of its influence. The flow outside this cone is uneffected by the liftoff. Inside the region bounded by the Mach cone the cross flow (conical) is subsonic and the governing conical equations are elliptic. Therefore the solution of this domain rests on an iterative or relaxation procedure. The segment of the shock between AB (Figs. 6-14 and 6-12) has the following properties. At point B the shock rotates the flow opposite in sense from that at point A. At point A and at points 1 and 2 upstream (see Fig. 6-13) the shock rotates the oncoming flow through a clockwise deflection. At point B the deflection is counterclockwise. Between A and B the shock goes through the spectrum and produces no rotation (is normal in the conical sense) at point C. The shock produces sonic velocity at point B where there is anchored a centered expansion to reestablish the background pressure. This expansion produces supersonic cross flow so that a portion of the domain shown in Fig. 6-14 does not have subsonic cross flow.

FLOW UNAFFECTED
BY LIFTOFF

UNDISTURBED
PLUME BOUNDARY

A

C

B

SYMMETRY
PLANE

TRACE OF MACH CONE
FROM LIFTOFF POINT
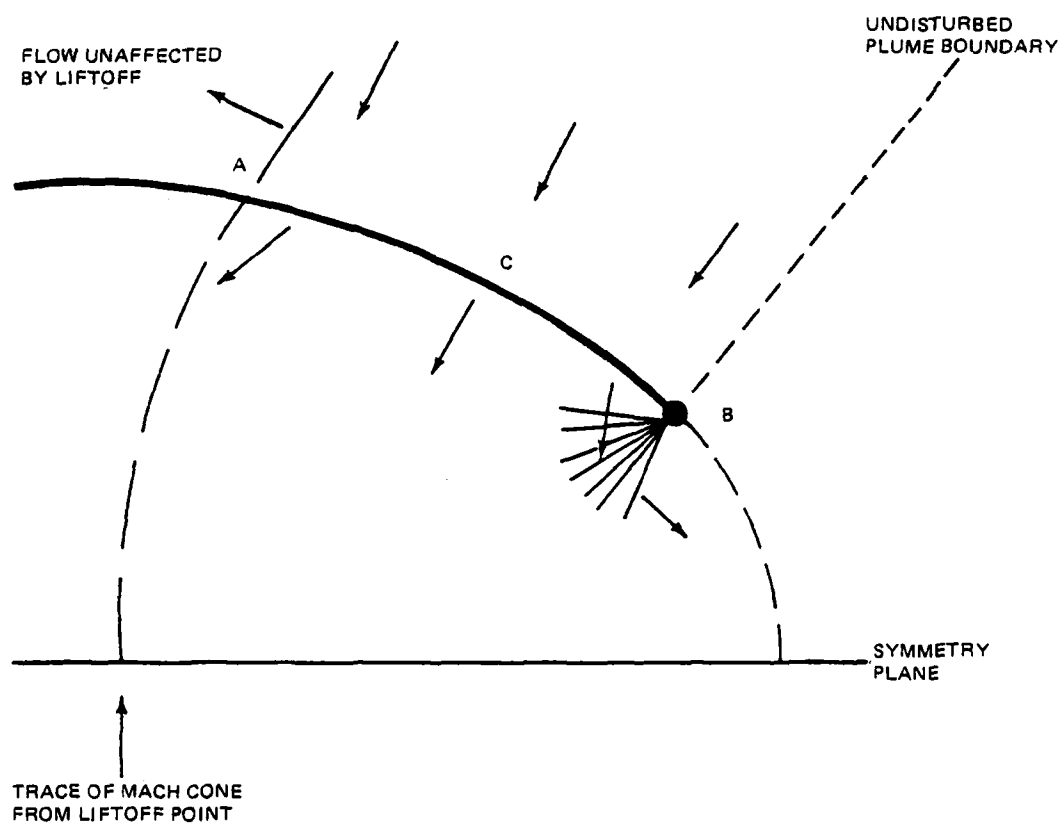
Fig. 6-14   Details of Conical Flow Geometry in the Shock Lift Off Region

REFERENCES

6-1   Kutler, P., "Supersonic Flow in the Corner Formed by Two
      Intersecting Wedges, " AIAA J., Vol. 12, p. 577, May 1974.

6-2   Anderson, D.A. and Nanqia, R.K., "Comparison of Numerical and
      Experimental Conical Flow Fields in Supersonic Corners with
      Compression and/or Expansion", Aeronautical Quarterly, Vol.
      28, Nov. 1977.

6-3   Shanker, V., Anderson, D., and Kutler, P., "Numerical Solutions
      for Supersonic Corner Flow", Journal of Computational Physics,
      Vol. 17, No. 7 July 1975.

6.4   Marconi, F., "The Supersonic Flow in Concial Corners" Ph.D
      Dissertation, Polytechnic Inst. of NY, June 1981.

6-5   Henderson, L.F., "On the Confluence of Three Shock Waves in
      a Perfect Gas," Aeronautical Quarterly, pp. 181-197, May 1964.

6-6   Henderson, L.F., "On a Class of Multi-Shock Interactions in
      a Perfect Gas," Aeronautical Quarterly, Vol. XVII, pp. 1-20,
      Feb. 1966.

6-7   Ferri, A., Elements of Aerodynamics of Supersonic Flow,
      Mac Millan Co. NY 1949.

SECTION 7

A NEW METHOD FOR TRACKING DISCONTINUITIES IN NUMERICAL CALCULATIONS

The multinozzle plume flow field is an example of a complex three dimensional supersonic flow field. These flow fields by their very nature have solutions which are discontinuous or have discontinuous derivatives. This is reflected in the mathematical description of the flow field by a set of hyperbolic partial differential equations. Equations of this type have wave like solutions which permit the propagation of functions which have discontinuous derivatives. In addition these equations admit solutions which are discontinuous. For the Euler equations the jump conditions along these discontinuities are the familiar Rankine-Hugoniot conditions. Two regions of continuous solution can be joined by a jump along a shock. A numerical solution procedure for supersonic flow problems should, therefore, include within it the ability to deal with these properties. Section 4 of this paper describes a "floating fitted discontinuity" scheme that tracks each discontinuity in detail, and computes the jump properties exactly. This method as outlined requires a large amount of program logic to handle complex geometries. In this section a new approach to tracking discontinuites is examined. The algorithm employs the normal functional approximations (Taylor series) at all regular mesh points. At mesh points which are recognized as being adjacent to discontinuities the appropriate flow properties are approximated by discontinuous functions.

There is an underlying assumption in almost all finite difference algorithms - the unknown function can be approximated locally by a Taylor series expansion. In fact, finite difference schemes are categorized primarily on this basis. A scheme is said to be second order, for example,

if the difference solution and the exact solution expanded in a Taylor series match to second order.   Supersonic flows solution generally cannot be approximated by Taylor series in all regions. It seems reasonable then to try to employ other more general functions in portions of the flow where there are discontinuities. As an example the Euler equations for 2D flow can be written in vector form* as

$$U_x + V_y = 0 \qquad\qquad (7-1)$$

At a shock wave the values of U upstream of the shock (U^-) and downstream of the shock (U^+) are related by

$$[U] - [V]/W = 0 \qquad\qquad (7-2)$$

where [ ] means jump across the shock and W is the shock propagation speed. The exact solution in the vicinity of a shock wave through the origin is

$$U = U^- + [U]\, H\,(x - y/W)$$

$$V = V^- - W[U]\, H\,(x - y/W) \qquad\qquad (7-3)$$

where H(z) is the unit step function given by

$$H\,(z) = 0 \quad z < 0$$

$$= 1 \quad z > 0 \qquad\qquad (7-4)$$

Simply substituting (7-3) shows that it is a solution (7-1) (in the context of the existence of the delta function $\delta\,(z)$) This analysis strongly suggests that solutions for U in the vicinity of the shock should take the form

$$U = U^- + [U]\, h\,(z) \qquad\qquad (7-5)$$

where h (z) is a chosen function that has the desired properties of H(z) and can easily be employed in a numerical scheme.

---

* for the Euler equations $\quad U = \begin{pmatrix} \rho u \\ p + \rho u^2 \\ \rho u v \\ \rho u h_0 \end{pmatrix} \quad V = \begin{pmatrix} \rho v \\ \rho u v \\ p + \rho v^2 \\ \rho v h_0 \end{pmatrix}$

Before proceeding it is interesting to note some of the properties of the "exact" solution for a shock wave Equation (7-3). Neither U or V are continuous across a shock wave. $U + WV$ is continuous

$$U^- + WV^- = U^+ + WV^+ \qquad (7-6)$$

The vector V is a function of U only. It can be expressed symbolically as $V = F(U)$ so that $V^+ = F(U^+)$ and $V^- = F(U^-)$. Equation 7-6 is then a relationship between the vector U^- and U^+

$$U^- + WF(U^-) = U^+ + WF(U^+) \qquad (7-7)$$

No value of U between U^- and U^+ can be substituted on the right hand side of Equation (7-7). In shock capturing schemes where the solution vector U varies smoothly (or not so smoothly) between U^- and U^+ in the region of the shock jump Equation (7-7) is not satisfied. The portion of the flow field between U^- and U^+ is an artifact of the calculation and has the inherent error associated therein.

As a test bed for these ideas the solution of a supersonic flow field containing a contact discontinuity was employed. This flow field was chosen because : (1) contact discontinuities spread out over more mesh points than shocks and (2) it represents a jump in entropy (total pressure) only - pressure and deflection are continuous across it. In the following paragraph the use of a ramp function to model a jump in entropy is described in detail. Then the brief discussion of the numerical calculation procedure is given. At mesh points away from the jump a standard first order finite difference scheme is employed. Results of two test computations are discussed in detail. (In the computer code stagnation pressure is used instead of entropy.)

The ramp function shown in Fig. 7-1 was employed in order to implement some of these concepts.

$$R(z) = \begin{cases} 1 & z < 0 \\ 1 - z/h & 0 < z < h \\ 0 & h < z \end{cases}$$

Figure 7-2 shows a portion of a finite difference mesh near the vicinity of a discontinuity in entropy (or stagnation pressure). In the mesh inverval $(j-1, j+1)$ there is a discontinuity in the function S. If the functional form of S in this mesh interval is given by the ramp function then

$$S = S_{j+1} + (S_{j-1} - S_{j+1})\, R\, (x - x_{oj}) \qquad (7\text{-}9)$$

where $x_{oj} = x_j - h(S_{j-1} - S_j)/(S_{j-1} - S_{j+1})$ $\qquad (7\text{-}10)$

or $\qquad \lambda = (S_{j-1} - S_j)/(S_{j-1} - S_{j+1})$

$\qquad x_{oj} = x_j - \lambda h$

A possible interpretation of the distribution of S in the interval is shown as a dashed line in Figure 7-2. S can be envisioned to have a step discontinuity at the mid point of the ramp function. The value of S_j serves to locate this point between $j-1$ and $j+1$. The governing equation for S in one dimensional unsteady flow is*

$$S_t + u S_x = 0 \qquad (7\text{-}11)$$

Using the ramp solution of equation 7-11 given by equation (7-9) the value of S at time Δt latter than is shown in figure 7-2 is given by

---

* Discontinuous solutions of this equation follow the same form as equation 7-3. $S = S^- + [S]H(x-ut)$
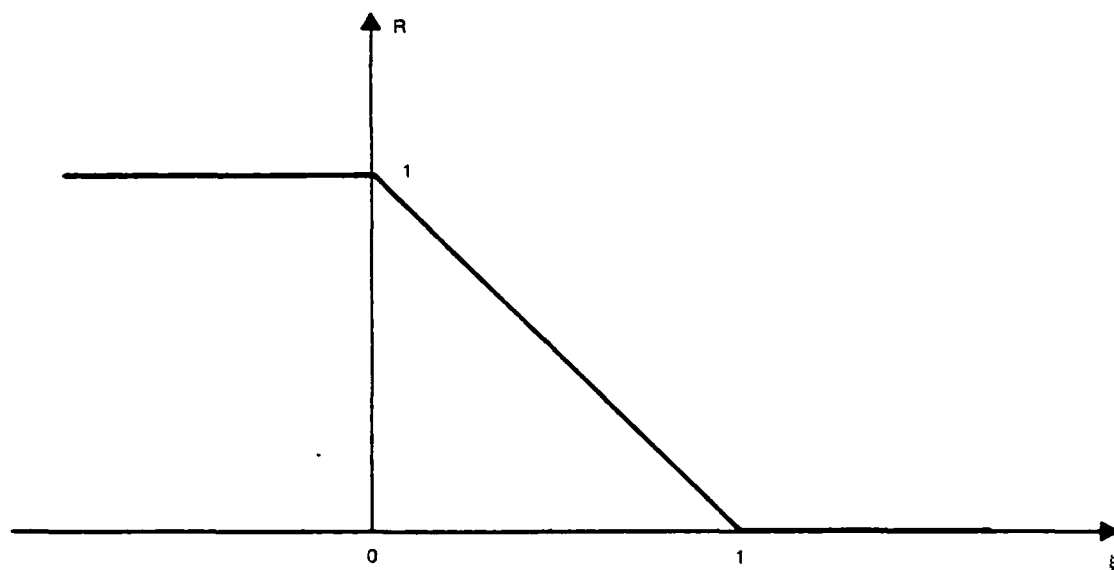
7-4

$$R = \begin{cases} 1 & \xi < 0 \\ 1 - \xi & 0 \leqslant \xi \leqslant 1 \\ 0 & \xi > 1 \end{cases}$$
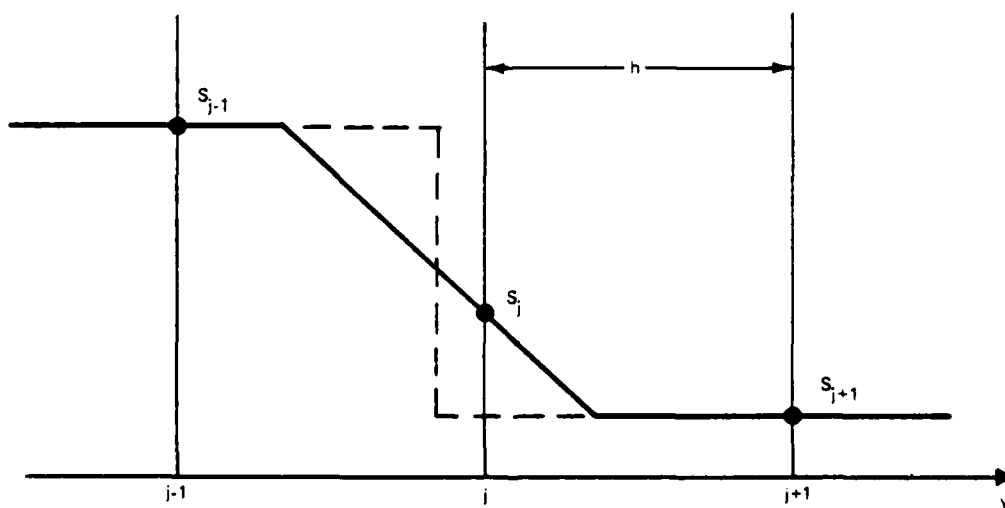
Fig. 7-1 Definition of the Ramp Function

Fig. 7-2 Ramp Profile Rendition of Entropy Discontinuity

7-5

$$SN_j = S_{j+1} + (S_{j-1} - S_{j+1}) \, R \, (x_j - u_j \Delta t - x_{0j}) \qquad (7\text{-}12)$$

if $u > 0$

$$SN_{j+1} = S_{j+1} + (S_{j-1} - S_{j+1}) \, R \, (x_j - u_j \Delta t + h - x_{0j}) \qquad (7\text{-}13)$$

if $u < 0$

$$SN_{j-1} = S_{j+1} + (S_{j-1} - S_{j+1}) \, R \, (x_j - u_j \Delta t - h - x_{0j}) \qquad (7\text{-}14)$$

A research code (KAYT1) was written to investigate the utility of the ramp function in certain problems. The program is for two dimensional supersonic flows and employs a finite difference calculation procedure using windward differences and characteristic form for the equations. The purpose of this section is to describe the results using the ramp function so only a brief outline of the numerical scheme will be given. The primary unknowns are pressure, flow deflection and total pressure. The governing equations are

$$\theta_x + \lambda_1 \theta_y + (\beta/\gamma M^2)(P_x + \lambda_1 P_y) = 0 \qquad (7\text{-}15)$$

$$\theta_x + \lambda_2 \theta_y - (\beta/\gamma M^2)(P_x + \lambda_2 P_y) = 0 \qquad (7\text{-}16)$$

$$P_{ox} + \lambda_3 P_{oy} = 0$$

$$(7\text{-}17)$$

where $P = \ln(p/p_r)$, $\lambda_1 = \tan(\theta + \mu)$, $\lambda_2 = \tan(\theta - \mu)$,

$\lambda_3 = \tan\theta$, and $P_0 = \ln(p_0/p_r)$ and p_r is

some reference value of pressure. The marching direction is the x direction. Transverse (y) derivatives in each equation are evaluated by either forward or backward two point formulas depending on the sign of λ_i multiplying that term. For example, in equation (7-15) the term $\lambda_1 P_y$ is evaluated at mesh point J (where $y = h(J-1)$ and h is the mesh spacing) as follows

$$\lambda_1 P_y = \begin{cases} (\lambda_1/h) \, (P(J) - P(J-1)) & \lambda_1 > 0 \\ (\lambda_1/h) \, (P(J+1) - P(J)) & \lambda_1 < 0 \end{cases} \qquad (7\text{-}18)$$

In this formula all values of the pressure are at the known station x. The derivatives in the marching direction (x) are evaluated by two point forward derivatives as follows

$$P_x = (PN(J) - (P(J))/\Delta x \qquad (7-19)$$

where PN(J) denotes the value of P at mesh point J and $x = \Delta x$. Formulas (7-19) and (7-18) are used for all derivatives in equations (7-15), (7-16) and (7-17) to derive, at every mesh point, two equations in the two unknowns PN and θN and an equation for P_0N. The code overrides the basic equation for P_0N if it is determined that there is a discontinuity in P_0 at some mesh point. Then the determination of P_0N employs the ramp function algorithm as outlined in the previous paragraphs.

Figure 7-3 shows the schematic of the flow field used as the first test example. Initially at x = 0 and y > 0 the flow is inclined at 15° to the x axis. At x = 0 and y = 0 the flow inclination is 10°. The flow has a Mach number of 2 at mesh points 2-10 and 4 at mesh points 11-50 and 2.19 at mesh point 1. The flow situation develops as follows. There is initially a discontinuity in total pressure between mesh points 10 and 11. A 5° expansion which is initially between mesh points 1 and 2 propagates into the flow and interacts with the contact surface. At the contact surface both pressure and flow deflection are continuous and there is a jump in stagnation pressure. The flow is divided into five regions by the expansion waves as shown in Figure 7-3. In these regions the flow properties are constant and the exact solutions are given in the table on the figure. Figure 7-4 shows the numerical computation of this flow using KAYT1. The step size in the x direction is held fixed at h/2 for these calculations. The values at the boundaries y = 0 (J = 1) and y = 49 (J = 50) are also held fixed.

7-7
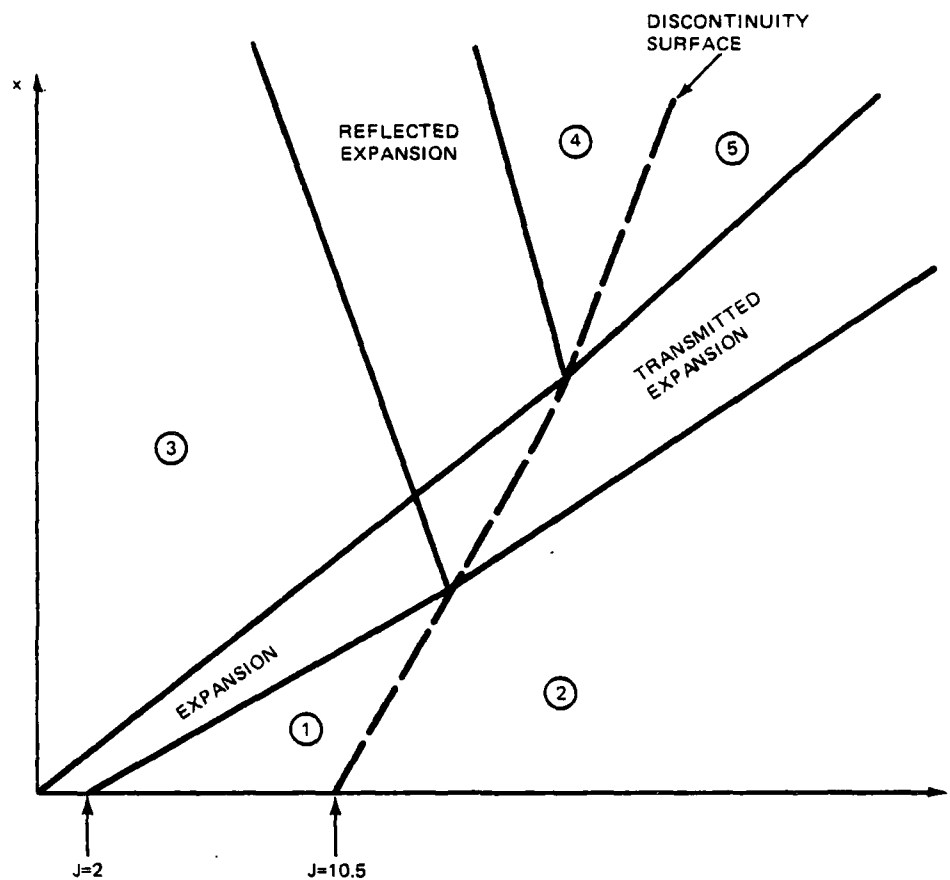
TABLE OF PROPERTIES IN EACH REGION

	M	θ	$\ln (p/p_1)$	$\ln (p_0/p_1)$	$\theta + \nu$	$\theta - \nu$
1	2	.262	0	2.057	.722	-.199
2	4	.262	0	5.023	1.41	.886
3	2.19	.175	-.291	2.057	.722	.373
4	2.24	.199	-.375	2.057	.771	-.373
5	4.29	.199	-.375	5.023	1.41	-1.01

Fig. 7-3 Schematic of Supersonic Flow Field Having an Expansion
Fan Interact with a Discontinuity in Total Pressure
(Test Case One)

(a) PRESSURE PROFILES
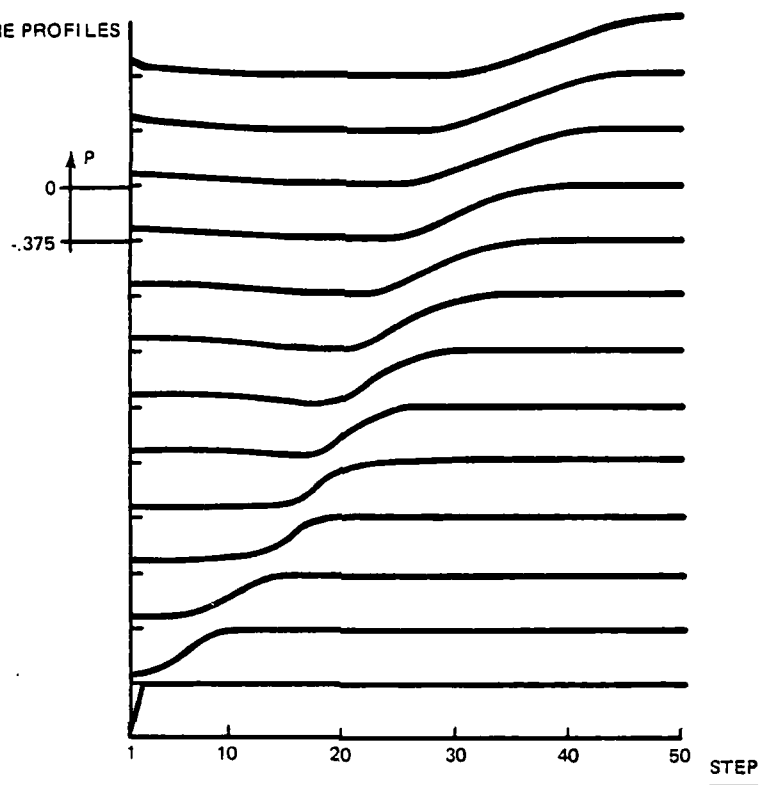
(b) FLOW DEFLECTION
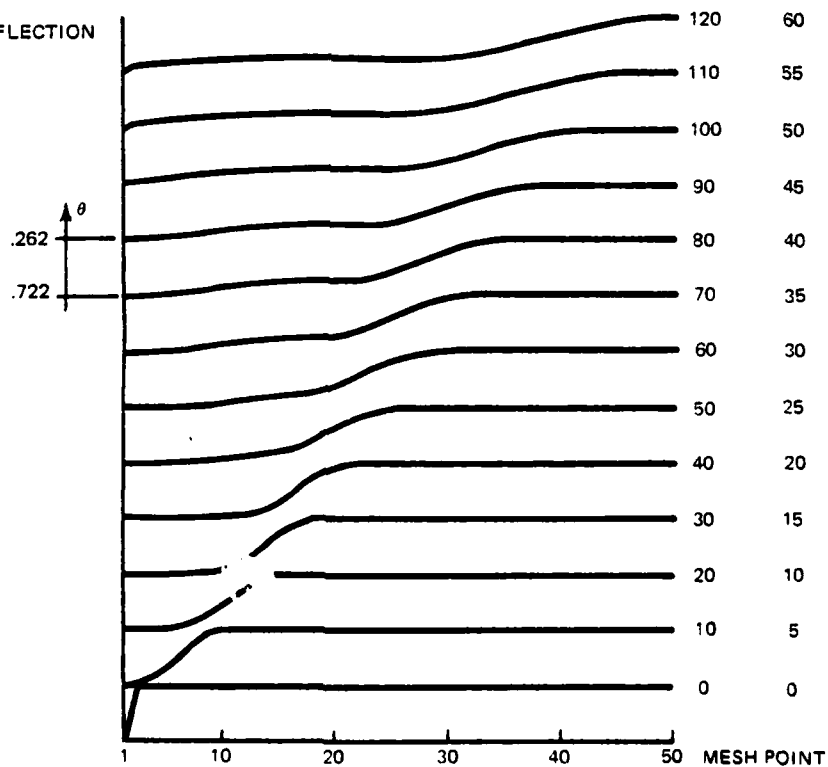
STEP	x
120	60
110	55
100	50
90	45
80	40
70	35
60	30
50	25
40	20
30	15
20	10
10	5
0	0

Fig. 7-4 Numerical Computation of Test Case 1 (Sheet 1 of 3)

(c) STAGNATION PRESSURE

LOCATION OF SLIP LINE
BY CHARACTERISTIC
CALCULATION

Po

5.023

2.057

1   10   20   30   40   50

STEP	X
120	60
110	55
100	50
90	45
80	40
70	35
60	30
50	25
40	20
30	15
20	10
10	5
0	0

(d) $\theta + \nu$

$\theta + \nu$

1.41

.771
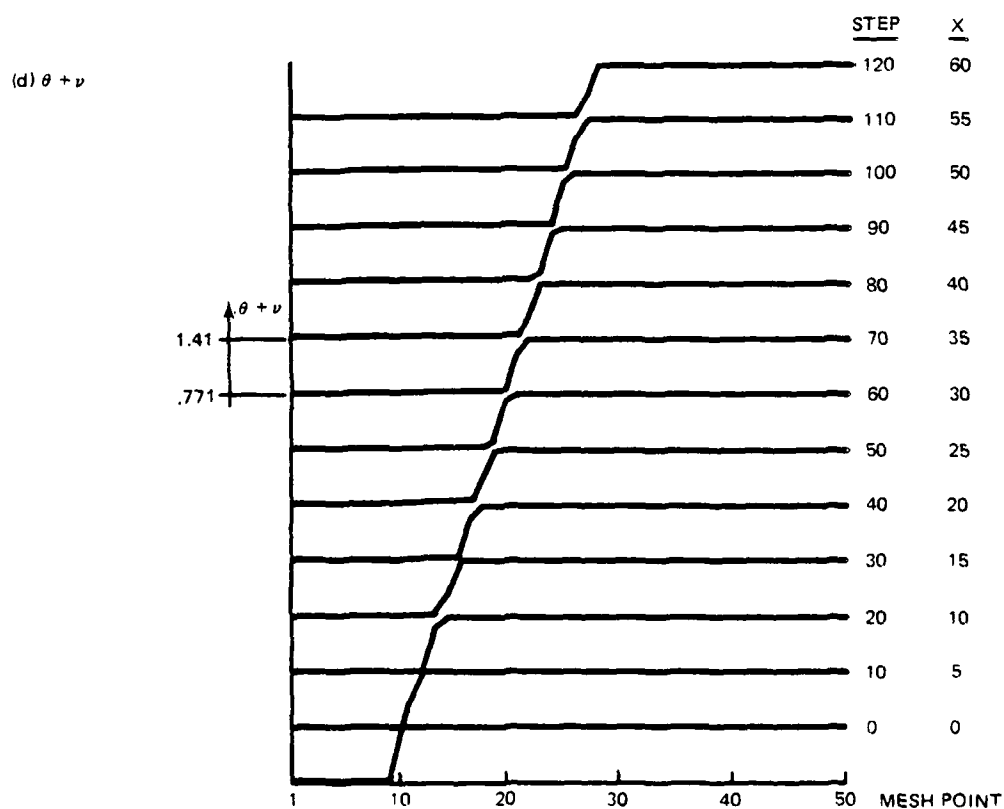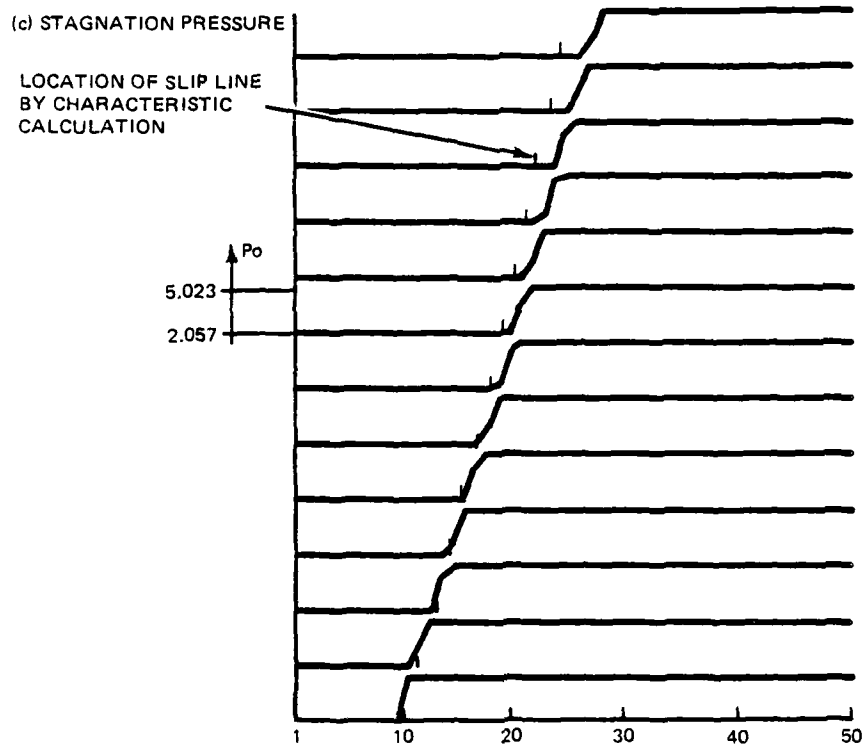
1   10   20   30   40   50   MESH POINT

Fig. 7-4 Numerical Computation of Test Case 1 (Sheet 2 of 3)
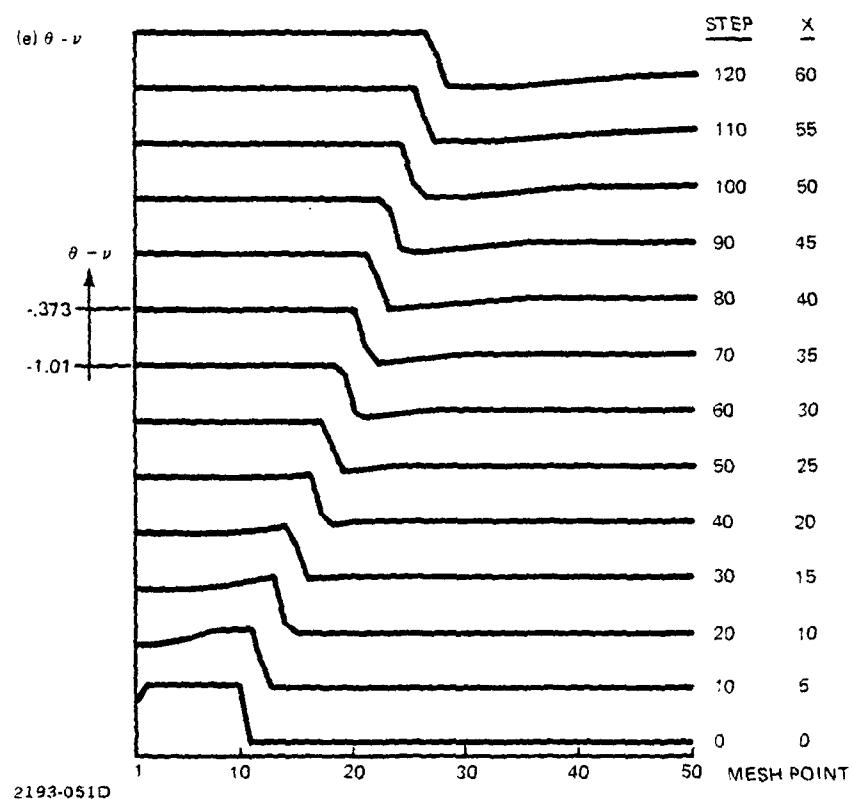
(e) θ - ν

2193-051D

Fig. 7-4 Numerical Computation of Test Case 1 (Sheet 3 of 3)

Figures (7-4) (a) and (b) show the smooth development of pressure and flow deflection. In these diagrams it is hard to see where the discontinuity is. Figure (7-4) (c) shows the total pressure profiles. The ramp profile joins the constant region on the left to the higher but constant region on the right. The jump in total pressure takes place with a single intermediate mesh point. At two stations step 60 and step 90 these are actually two intermediate mesh points. This occurred because the detection scheme for locating the total pressure discontinuity was very primitive. In any event the algorithm produces self mending results. Figures (7-4)(d) and (e) show the profiles of Reimann invariants $\theta + \nu$ and $\theta - \nu$ respectively. The code does not use these variables in the computations. These graphs serve as checks on the calculation procedure. The jumps that occur in each of these profiles is a result of the jump in total pressure which is associated with a jump in Mach number and hence a jump in ν the Prandtl Meyer angle. In (7-4)(e) the initial expansion fan starts at x = 0 between mesh points 1 and 2. It moves to the right (along $\theta + \mu$ characteristics) and spreads out. The natural spreading of the fan is augmented in the numerical calculation because the wave front (discontinuous jump in derivative) at the head and tail of the fan are not tracked by the program. (There are no general algorithms for the computations of supersonic flow which address this point.) By step 20 (x = 10) the expansion has intersected with the contact discontinuity and is subsequently transmitted. Only a wave moving to the right appears in the results for $\theta - \nu$. This is in accordance with classical supersonic flow theory. In Fig. (7-4)(d) the left moving waves become evident. Before step 40 only the movement of the discontinuity is evident. Then at step 40 the reflected expansion wave starts to form. The values of $\theta + \nu$ and $\theta - \nu$ in regions 4 and 5 are compared with

their exact values in the table below. Is it clear that the numerical calculation is very accurate in the computation of these quantities.

Comparison of Characteristic Calculation and Finite Difference Calculation				
Region	$(\theta + \nu)_{FD}$	$(\theta + \nu)_{Char}$	$(\theta - \nu)_{FD}$	$(\theta - \nu)_{Char}$
4	.770	.771	- .373	- .373
5	1.41	1.41	-1.01	1.01

Figure 7-5 compares the computations using the ramp profile with a computation that does not specifically "fit" the discontinuity. Figure (7-5)(a) compares the profiles of total pressure. The profiles are smooth but the jump in total pressure is spread out over approximatley fifteen mesh points. Figure (7-5)(b) and (c) show the profiles of the Reimann invariants. Again the results are smooth and have the correct values upstream and downstream of the discontinuity. However, it is clear that in these results the discontinuity zone is now fifteen mesh points wide. This represents about one third of the mesh points used in the calculation.

The most series errors in the computed results using the ramp function appears in figure (7-4)(c). The exact location of the discontinuity and the center of the ramp function have drifted apart. This is a result of the wave front spreading noted in the previous discussion. The expansion zones spread out ahead of the exact characteristics location and cause the value of the streamline slope to change in advance of the proper positon. In order to
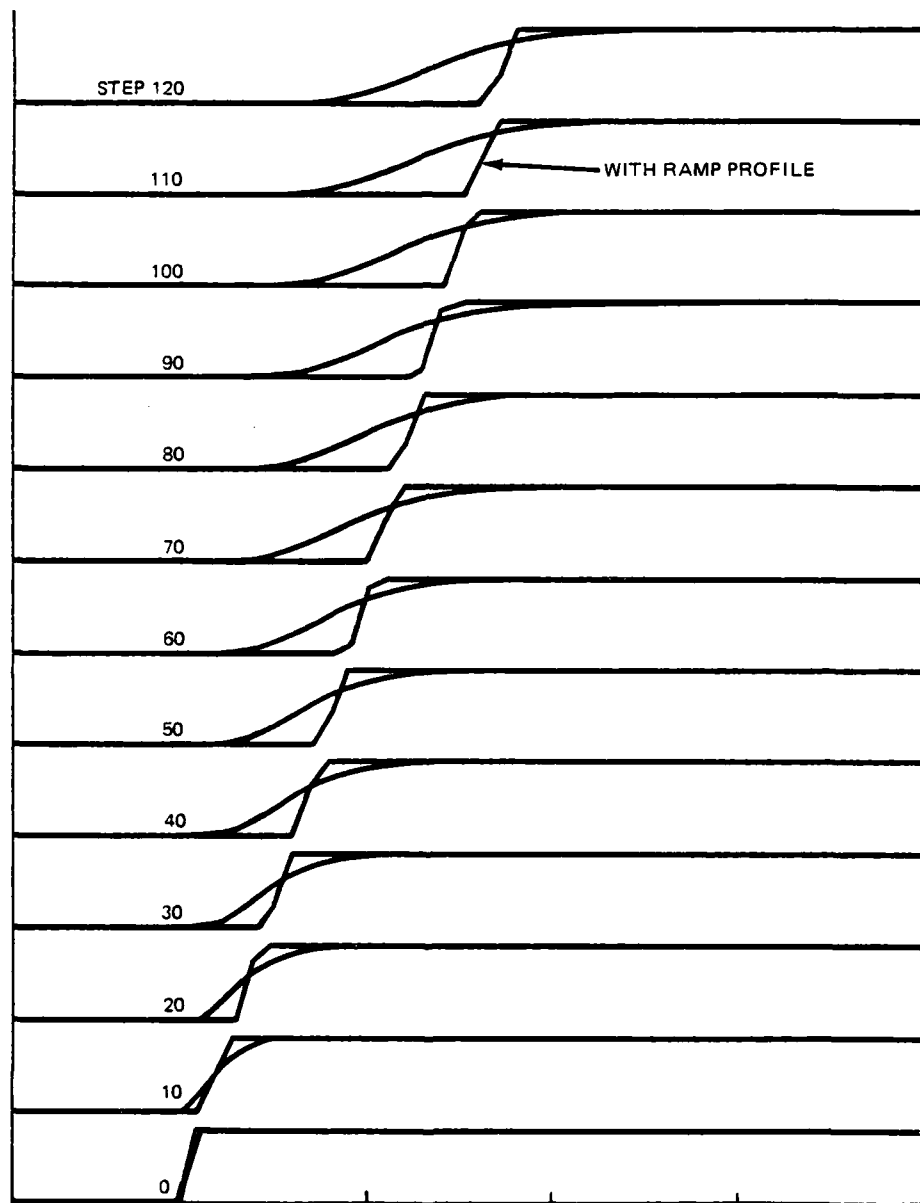
(a) TOTAL PRESSURE

Fig. 7-5 Comparison of Numerical Calculation of Test Case One
With and Without Ramp Profile
(Sheet 1 of 3)

7-14
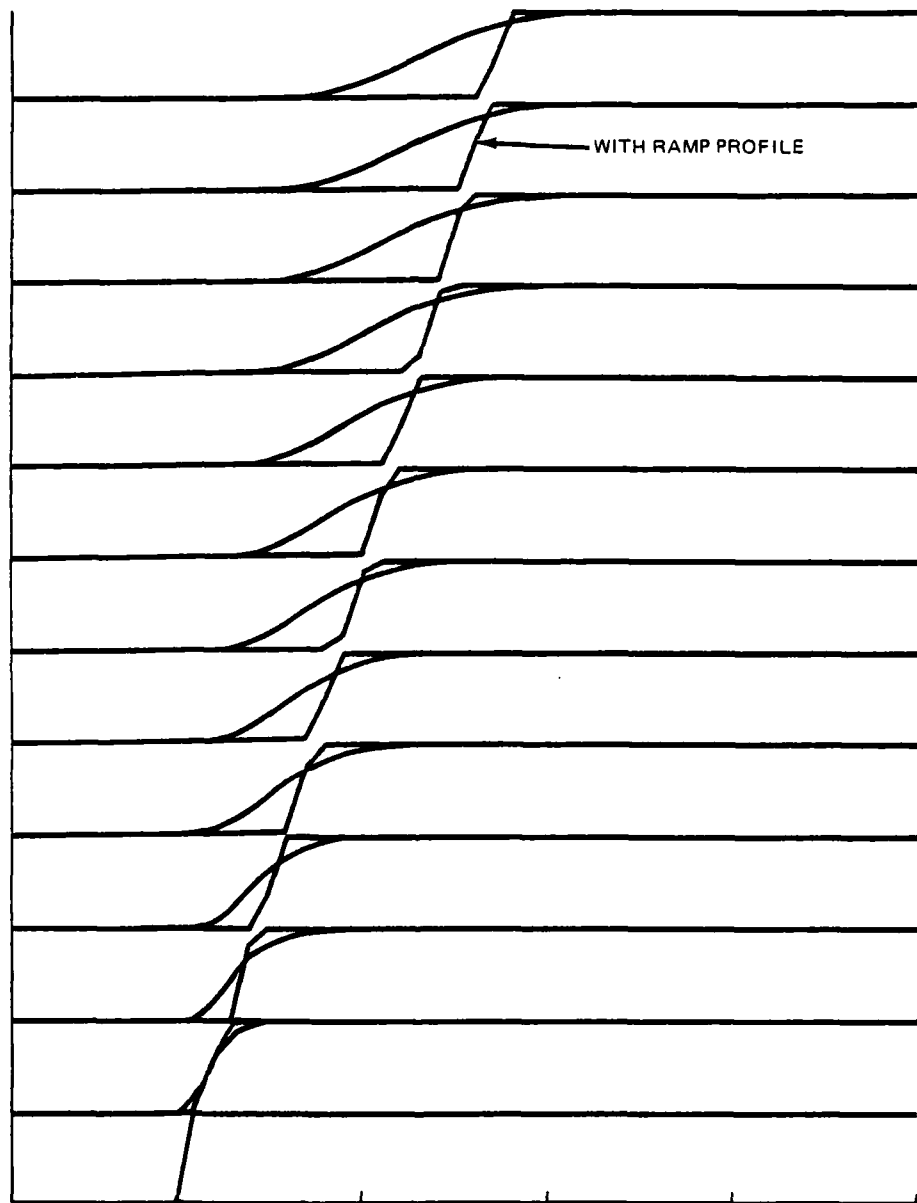
(b) $\theta + \nu$

Fig. 7-5 Comparison of Numerical Calculation of Test Case One
With and Without Ramp Profile
(Sheet 2 of 3)

(c) $\theta \cdot v$

Fig. 7-5 Comparison of Numerical Calculation of Test Case One
With and Without Ramp Profile
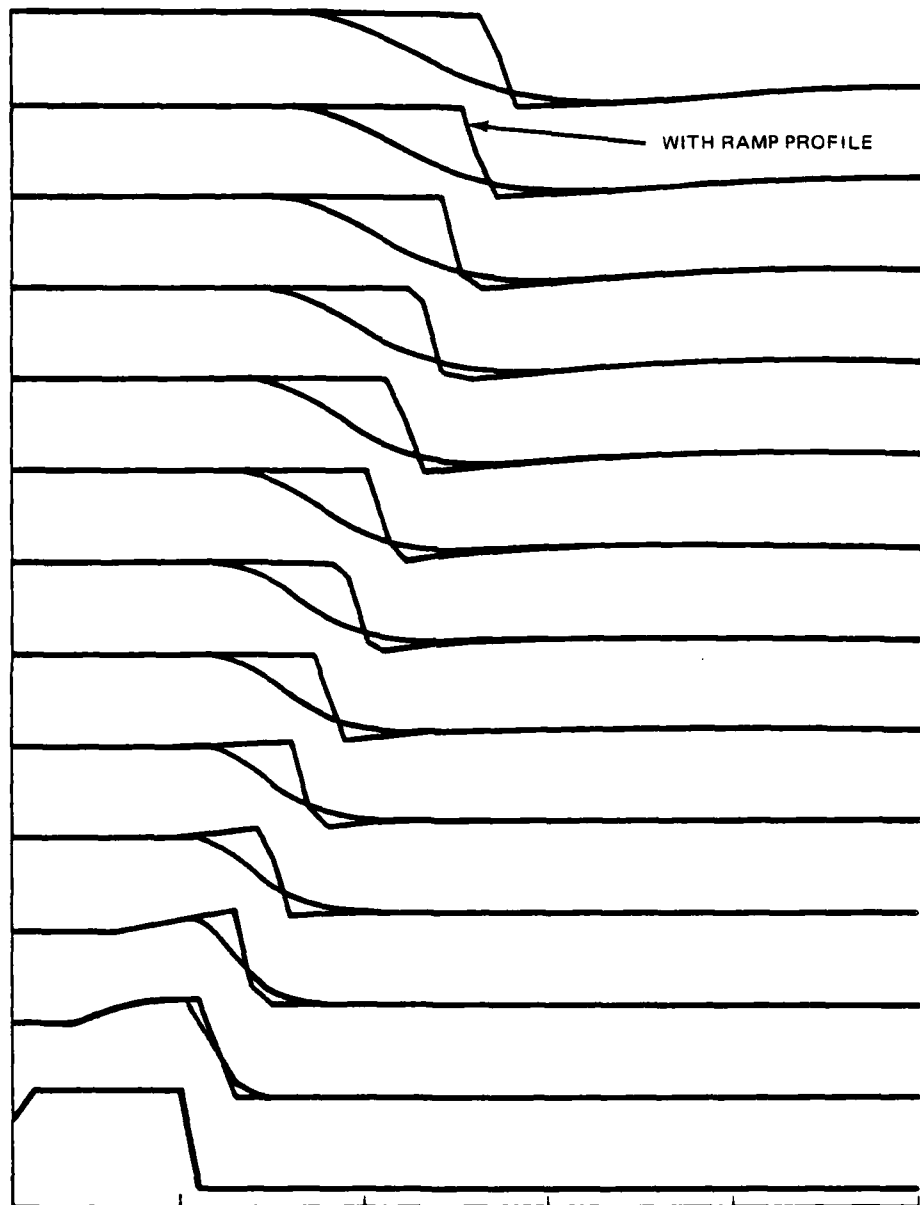(Sheet 3 of 3)

determine if this is the correct explanation an additional calculation was performed that did not have a wave front in the initial profile. Figure 7-6 shows the characteristic mesh for this computation. At step zero there is an expansion zone which is propagating toward a constant pressure boundary. In the finite difference program this constant pressure boundary is modelled by a jump in total pressure. The expansion zone impinges on the boundary and reflects as compression waves which move back into the flow. On this figure is the computed location of the flow boundary by the finite difference calculation. The agreement is virtually perfect. Figure 7-7 shows pressure profiles for the entire computation. Figure 7-7(a) is the initial pressure distribution at x = 0. Figure (7-7)(b) is at x = 10 where the expansion has partially reflected from the boundary. The finite difference computation and the characteristic calculation are in virtual agreement. The largest errors seems to be near the boundary where there is a break in slope in pressure. Figures 7-7(c) and (d) shows the subsequent development of the flow field. At x = 70 the compression wave is about to reflect from the inner boundary. There is a spreading of the wave that is first evident at x = 40. At x = 70 the finite difference results first preceded then lag the exact calculation by 3-4 mesh points. The precise cause of this dispersion has not been studied. Two primary sources that should be investigated are the first order nature of the computational algorithm and the details of the reflection process at the boundary ramp function.
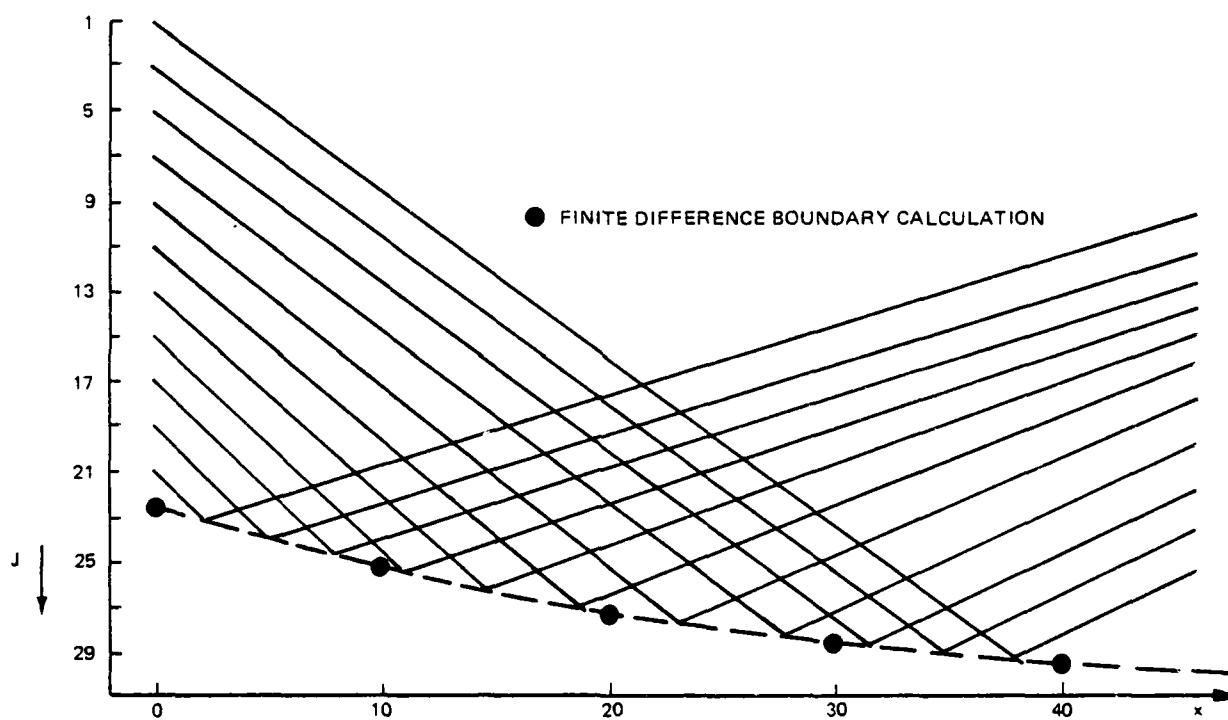
Fig. 7-6 Test Case Two - Calculation of Constant Pressure Boundary

(a) INITIAL PROFILE

● FINITE DIFFERENCE CALCULATION

● BOUNDARY BY FINITE
   DIFFERENCE CALCULATION

(b) x = 10

(c) x = 40

(d) x = 70
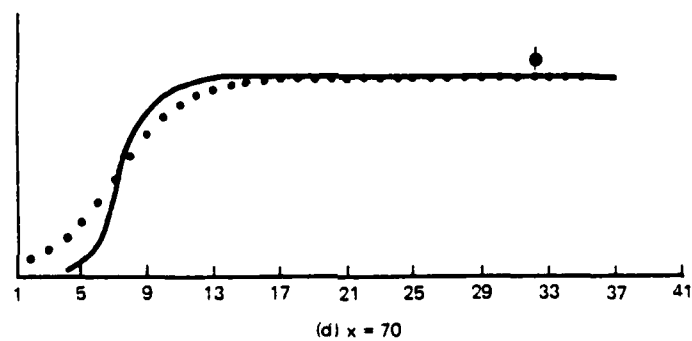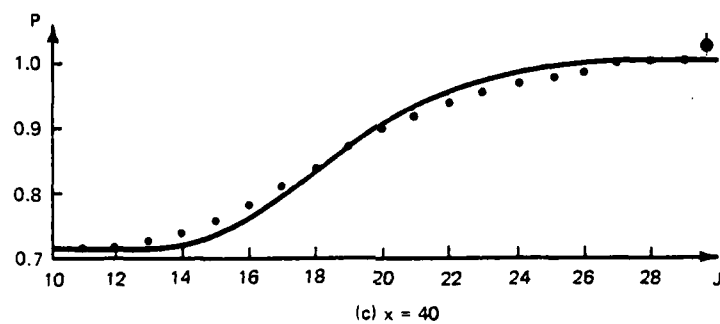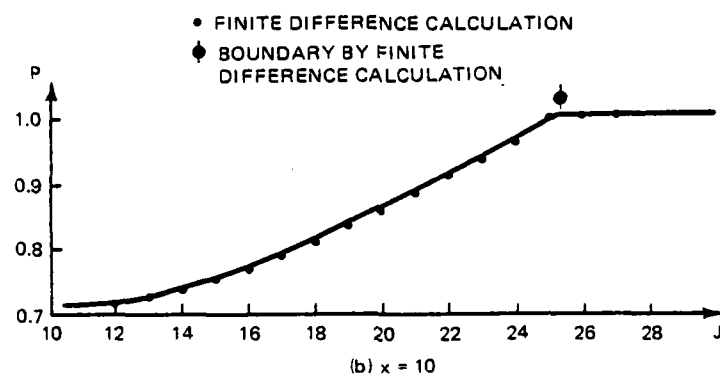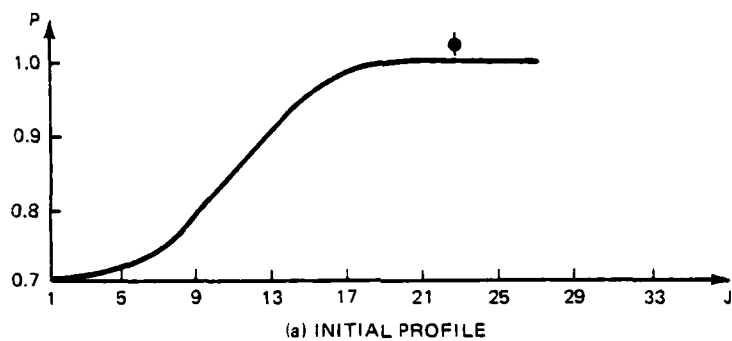
Fig. 7-7 Comparison of Pressure Profiles for Characteristic Calculation
and Finite Difference Calculation for Test Case Two

The use of the ramp function in three dimensional flow requires further work. In two dimensional flow the actual position of the discontinuity was associated with the intermediate value of the function. In essence the method tracks the discontinuity on a subgrid basis. In three dimensions this tracking must take place in two directions (in the cross plane). A method must be worked out to accomplish this in a simple manner. The ramp function must also be tested out in flows with shock waves. The shock waves have a jump in all flow properties and not just a single one as was employed in the test calculations. The shock propagation problem has the added complication that the properties behind it are a function of the shock (wave) speed.

SECTION 8

MACH DISC ANALYSIS AND NUMERICAL COMPUTATION

Shock wave systems in exhaust plume flow fields can develop in a manner which produces normal shock waves or Mach discs. In axisymmetric flows the shock wave strength intensification process leading to the formation of the Mach disc is understood on theoretical grounds. For three dimensional plumes there is little or no knowledge of the processes and flow properties that result in normal shock segments in the plume (see Section 3). The numerical prediction of the location of the Mach disc in axisymmetric flows has been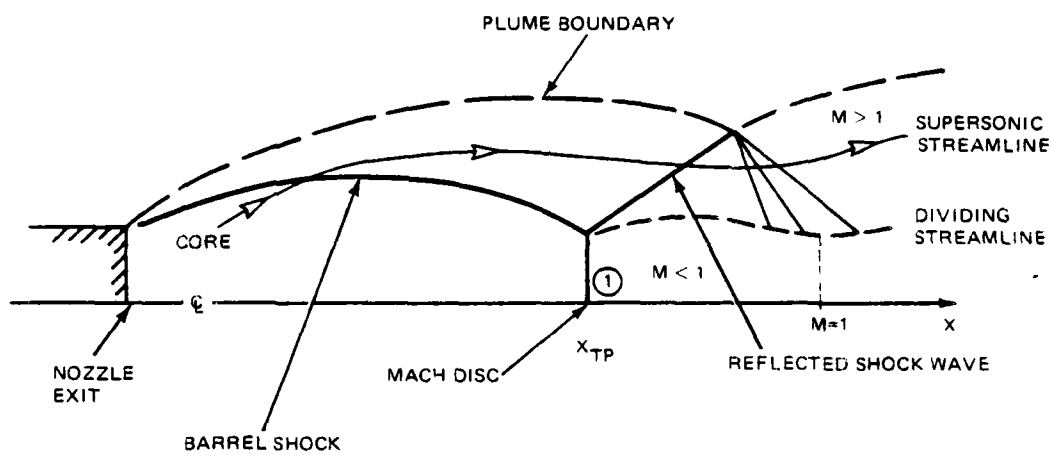 accomplished in recent years (Refs. 8-1, 8-2). These studies are purely numerical calculations. In this section an analysis is derived which explicitly highlights the key properties of the exhaust plume that influence the Mach disc location. Employing the results of this analysis a new numerical integration scheme is derived to compute Mach disc streamtubes. This new method has the potential for overcoming the shortcomings of the previous integration procedures. The improved understanding of the axisymmetric Mach disc physics should serve as a first step in understanding the three dimensional plume situation.

A schematic of an axisymmetric plume with a Mach disc is shown in Fig. 8-1. At all points in the flow outside of the Mach disc streamtube the plume gas velocity is supersonic. A barrel shock divides the plume into a "core" and a shock layer upstream of the Mach disc. At some point along the barrel shock there is a triple point which is the confluence of the barrel, reflected and Mach disc shock waves. Downstream of the triple point the flow is divided into a supersonic flow bounded on the outside by the reflected shock wave and plume boundary and on the inside by a dividing streamline and a subsonic core. The subsonic core flow has passed through the normal shock (Mach disc) and is centered about the plume axis.

PLUME BOUNDARY

M > 1   SUPERSONIC
        STREAMLINE

CORE

DIVIDING
STREAMLINE

M < 1

M = 1   x

NOZZLE
EXIT

MACH DISC

x_{TP}

REFLECTED SHOCK WAVE

BARREL SHOCK

2193-055D

Fig. 8-1 Schematic of Axisymmetric Underexpanded Rocket Exhaust Plume

According to Abbett (Ref. 8-1) the triple point location can be uniquely determined by finding the Mach disc position which leads to a smooth passage through the sonic acceleration of the subsonic streamtube (see Fig. 8-1). In both Refs. 8-1 and 8-2 the following models were employed. The subsonic streamtube was described by a one dimensional flow model. For an estimated position of the triple point the subsonic flow and supersonic flows are computed simultaneously by a forward integration schemes. Two possible solutions result: a supercritical flow has the subsonic streamtube reaching sonic velocity while it is still decreasing in area. In the other case, a subcritical flow the subsonic streamtube reaches a minimum in area and then increases in diameter without choking. An iterative procedure is employed which narrows down the axial position of the triple point by observing these two types of solutions. This is a classical shooting method to determine a solution for a system of equations which have a saddle point singularity downstream (at the throat of the subsonic streamtube). The basic disadvantage of this scheme is that no solution for the subsonic streamtube emerges. Rather a bracket on the triple point location is developed. The existence of a solution within this bracket is not certain.

The present method does not require shooting the solution from the triple point location. In the inviscid approximation the location of the sonic throat can be calculated without a subsonic calculation. The subsonic streamtube can then be computed by an upstream integration of the equations from the sonic throat making use of certain known properties of supersonic flow to determine the outer flow. A viscous approximation to the Mach disc problem is presented which accounts for the effects of mixing between the subsonic streamtube and supersonic flow in the simplest manner possible. This

does not alter the basic computational scheme but adds one more layer to the iteration scheme.

A one dimensional model for the subsonic streamtube is retained. The equations governing the flow passing through the Mach disc are (Ref. 8-3)

$$\frac{M^2-1}{\gamma M^2} \frac{1}{p} \frac{dp}{dx} + \frac{1}{A} \frac{dA}{dx} = \frac{1 + (\gamma-1)M^2}{2} \left(\frac{4\hat{f}}{D}\right) \qquad (8-1)$$

$$\frac{1}{p_0} \frac{dp_0}{dx} = -2\gamma M^2 \left(\frac{\hat{f}}{D}\right) \qquad (8-2)$$

where M is the Mach number, p the static pressure, A and D the subsonic streamtube cross sectional area and diameter, p_0 the average stagnation pressure, and $\hat{f}$ is the friction factor. Using a friction factor in this manner is an approximation that allows for the simple introduction of mixing effects along the dividing streamline. The flow behavior outside the dividing streamline is incorporated in the function $f(x) = \theta + \nu$ which is the value of the Reimann invariant on the downward running characteristic determined from a calculation of the supersonic flow. The pressure on the outside of the Mach disc tube flow is related to f by the following steps

$$f' = \theta' + \nu' \qquad (8-3)$$

( )' denotes d/dx

ν is the Prandlt Meyer function and is only a function of external Mach number (m)

$$\nu' = \frac{d\nu}{dx} = \frac{d\nu}{dm} \frac{dm}{dx}$$

using

$$\frac{p}{p_{o2}} = \left(1 + \frac{\gamma - 1}{2} m^2\right)^{-\gamma/\gamma-1}$$

and the fact that p_{o2} is constant along the bounding streamline equation (8-3) becomes

$$\frac{1}{p} \frac{dp}{dx} = \frac{f'-\theta'}{h(m)} \qquad (8-4)$$

where $h(m) = p \frac{dm}{dp} \frac{d\nu}{dm} = -\frac{1}{\gamma\beta} \left(1 + \frac{\gamma-1}{2} m^2\right) \left(\frac{1}{1+\epsilon\beta}^2 - \frac{1}{1+\beta}^2\right)$

where $\beta = \sqrt{m^2 - 1}$ and $\epsilon = (\gamma-1)/(\gamma+1)$

Equation (8-4) relates the pressure gradient in the external supersonic stream to the geometry ($\theta'(x)$) of the subsonic streamtube. The solution of the Mach disc flow requires that the pressure along the dividing streamline is matched. Therefore, combining equations (8-4) and (8-1) the basic interaction equation is

$$\frac{m^2-1}{\gamma M^2} \left(\frac{f'-\theta'}{h(m)}\right) + \frac{1}{A} \frac{dA}{dx} = \frac{1+(\gamma-1)M^2}{2} \left(\frac{4\hat{f}}{D}\right) \qquad (8-5)$$

For axisymmetric flow $A = \pi y^2$ where y is the local height of the subsonic streamtube. The governing equations become

$$\theta' - f' + B\theta = \sigma / (1-M^2) \qquad (8\text{-}6)$$

$$\frac{1}{p_0} \frac{dp_0}{dx} = \sigma_1 \qquad (8\text{-}7)$$

$$\text{where } B = \frac{2\gamma M^2}{1-M^2} \frac{h(m)}{y} \qquad (8\text{-}8)$$

$$\sigma = \gamma M^2 h(m) \left[1+(\gamma-1)M^2 \right] \hat{f}/y \qquad (8\text{-}9)$$

$$\sigma_1 = - \gamma M^2 \hat{f}/y \qquad (8\text{-}10)$$

Equation (8-6) is the fundamental interaction equation governing the pressure balance between the supersonic and subsonic flows and combined with equation (8-7) (when $\hat{f} \neq 0$) must be solved to determine the subsonic streamtube solution. The approximation $\tan\theta \approx \theta$ has been used in the derivation. The numerical solution of equations (8-6) and (8-7) will be discussed in later paragraphs. A discussion of the properties of equation (8-6) brings out interesting properties of the Mach disc and associated plume.

In the inviscid case it is possible to locate the sonic point in the subsonic flow before solving equation (8-6) by the following process. For a given location of the triple point along the barrel shock the computation of the external supersonic flow can be continued employing an approximate shape for the dividing streamline (see Fig. 8-1). From this solution the function $f(x) = \theta + \nu$ along the dividing streamline can be determined. Downstream of the Mach disc the total and static pressure as well as the Mach number M_1 are known and denoted p_1 and p_{01}. The corresponding sonic pressure p^* can be computed by the formula.

$$\frac{p^*}{p_1} = \left[\frac{\gamma+1}{1 + (\gamma-1)M_1^2} \right]^{\frac{\gamma}{\gamma-1}}$$

The sonic condition requires that $\theta = 0$. Determine the pressure on the supersonic side of the dividing streamline at every point for $\theta = 0$ from the (known) function $f(x)$

$$\nu(x) = f(x) - \theta(x)$$

$$\nu(x) = f(x)$$

Use the isentropic expressions relating ν to m and m to p to compute the pressure. Figure 8-2 shows a schematic plot of this pressure versus x. The sonic point or throat for the inner flow is determined at the point where these two curves cross. (Figure 8-2 shows two such crossings. It will become clear in the following discussion why the second crossing is the appropriate point). The point denoted $x*$ is the throat because it has the two required properties $\theta = 0$ and $p = p*$.

Properties of the solution at the initial point and the throat can be deduced from the interaction equation. For inviscid flow the interaction equation is

$$\theta' - f' + B\theta = 0 \tag{8-11}$$

The coefficient B is always negative for subsonic flow (Note that $h(m) < 0$). At the triple point the pressure is matched at p_1. There are two possibilities $\theta_1 > 0$ or $\theta_1 < 0$. For $\theta_1 > 0$ $\theta' - f' = -B\theta > 0$ therefore $\theta' > f'$. Thus if $f' > 0$ the initial dividing line will be unstable because $\theta' > 0$ and the slip line slope increases and forms an upward cusp. To attain a concave downward curve the initial value of f' must be negative. In terms of pressure this is a compression wave. In the case of $\theta_1 < 0$ a stable curve can only be achieved for $f' < 0$. In all plume calculations that have been examined the initial flow behind the triple point is compressive or has $f' > 0$, therefore, in these cases it is concluded that the initial slope of the dividing streamline must be positive.
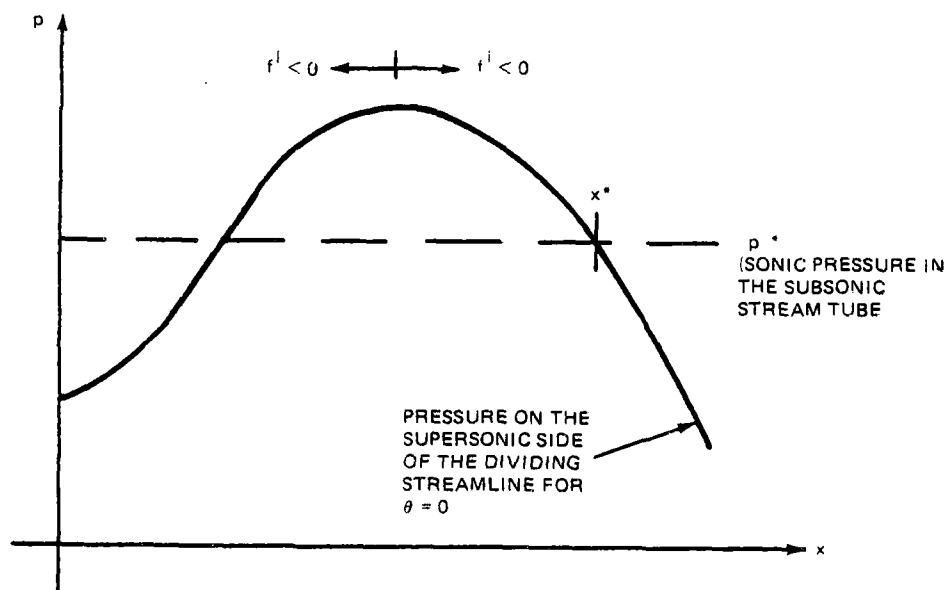
Fig. 8-2 Locating the Sonic Throat by Matching Supersonic
Side Pressure to Sonic Pressure

At the sonic throat the flow is accelerating and so $dp/dx < 0$. The pressure gradient has the same sign as $\theta'-f'$ since $h(m) < 0$ (see equation (8-4)). Thus $\theta'-f' < 0$ or $f' > \theta'$. The sonic throat has the following two conditions $\theta = 0$ and $\theta' > 0$. Therefore, the throat can only occur when $f' > 0$ or an expansion portion of the supersonic flow. This precludes the sonic throat from occurring at the first place the curves cross in Fig. 8-2 where $f' < 0$.

The following general picture (Fig. 8-3) emerges for the Mach disc streamtube. The solution curve in Fig. 8-3 is the pressure on the dividing streamline or in the subsonic streamtube. Also shown is the curve of pressure in the supersonic stream for $\theta = 0$ on the dividing line (denoted curve A) and the values of total pressure p_{01} and sonic pressure p^* in the subsonic streamtube. When the solution curve is above (below) curve A $\theta > 0$ ($\theta < 0$). The solution starts downstream of the triple point with pressure p_1. For all flows where there is a compression following the triple point in the supersonic flow the initial angle must be positive and decreases with x. Downstream of the triple point the subsonic streamtube undergoes an increase in pressure until the value of θ reaches zero. Downstream of this point in Zone (2) f' is still negative signifying a compressive outer wave pattern but $\theta' < f'$ so that the pressure drops and the angle decreases. In Zone 3 the outer flow is expanding and the function $f' > 0$. The value of θ increases smoothly ($\theta' > 0$) and reaches zero precisely at the point where sonic conditions are met and the inner streamtube is choked.
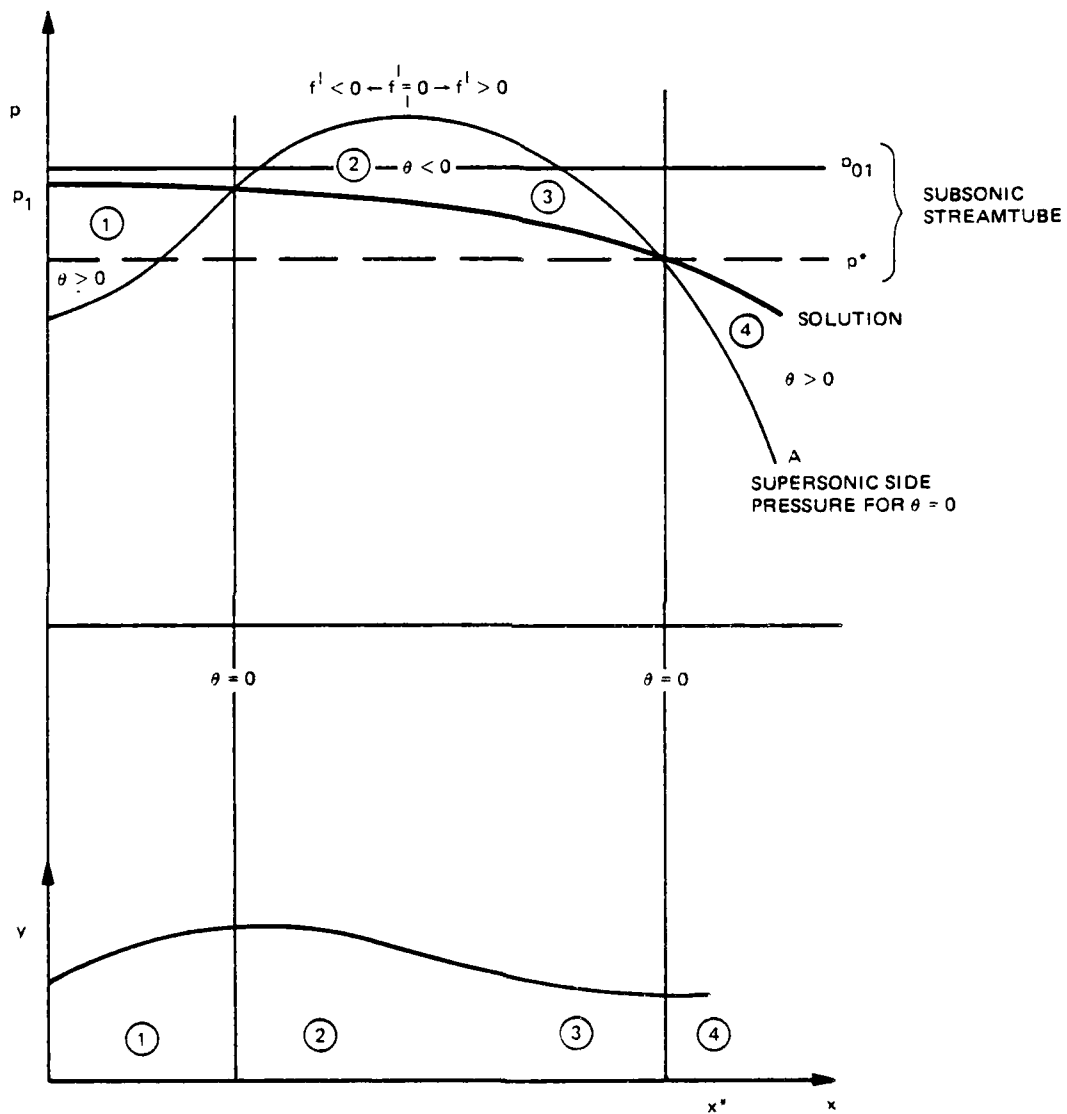
Fig. 8-3 Geometry of Mach Disc Stream Tube and Corresponding
Solution of Interaction Equation

It is clear that the function f plays a decisive role in determining the subsonic streamtube solution and hence Mach disc position. The value of the function f is related in a complex way to the entire plume flow solution upstream of the triple point. It is possible, however, to highlight some interesting properties which determine f. The value of f, the Reimann invariant on the downward running characteristic, would remain constant and equal to its value on the plume boundary if the flow were two dimensional and isentropic. Because the plume is axisymmetric and nonisentropic f is not constant along the waves but it is expected that whatever variations are due to these effects are approximately the same for all waves.

Figure 8-4 is a schematic of two plumes at widely different free stream conditions. The quiescient plume is shown for a slightly underexpanded nozzle exit conditions. The Mach number in the plume shock layer (between interface and barrel shock) is low, therefore, the downward running waves are at a steep angle and reach the Mach disc streamtube in a short axial distance. The pressure on the plume boundary is constant so that the variation in the function f comes from the curving plume boundary (Constant pressure means that ν is constant). The extent of the plume interface which directly influences the Mach disc flow is rather short. The highly underexpanded plume (Fig. 8-4b) has quite a different picture. The gas in the plume shock layer is at very high Mach number so that the portion of the plume boundary where f originates is quite extended. In addition the plume is in a hypersonic free stream which creates a large pressure gradient on the interface. Therefore, the details of the pressure and deflection along a large segment of the plume boundary are influential in determining both θ and ν along the interface and hence on the value of f at the Mach disc interface.
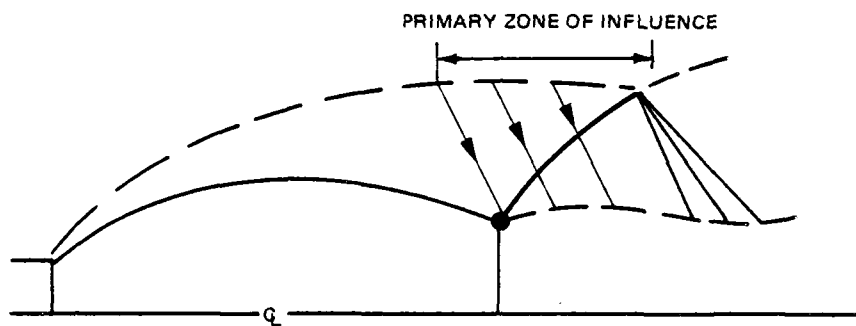
(a) QUIESCENT BACKGROUND
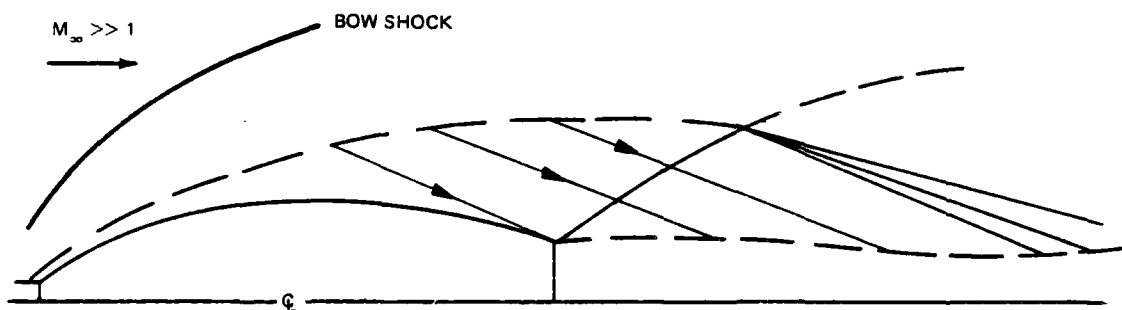
(b) HIGHLY UNDEREXPANDED PLUME IN A HYPERSONIC STREAM

2193-058D

Fig. 8-4 The Boundary Zone of Influence on the Mach Disc Flow
for Two Types of Flow

The effect of viscous mixing along the Mach disc streamline introduces additional complexity and new features in the solution. Within the scope of one dimensional analysis it is possible to introduce mixing effects in a global sense. It is realistic to employ this approximation at present because the actual detailed two dimensional flow field is a complex transonic flow with turbulent mixing and transverse pressure gradients which would be difficult to accurately model. In the model adopted here the influence of the mixing is to introduce a mechanism that increase the total pressure in the subsonic flow. Mixing also changes the flow inclination that the supersonic flow sees along the dividing streamline through a displacement effect. This effect is not incorporated in the present model. The sonic throat condition is no longer $\theta = 0$ but it has a small negative value. The increasing value of p_0 with distance results in increasing flow Mach number even at constant static pressure. Equations (8-6)-(8-10) show the relationship of the mixing terms in the interaction equation (8-6) and the total pressure equation (8-7). The Mach disc flow has lower velocity and lower total pressure than the outer supersonic flow so that $\hat{f}$ is negative and σ_1 is positive. A solution curve with mixing is sketched in Figure 8-5. The main difference to note in this solution compared to the inviscid solution (Fig. 8-3) is that p_0 and p^* are increasing with distance. The sonic throat is again located at the point where the pressure (p_s) evaluated by setting $\theta = \theta^*$ (using the function f) is equal to p^*. In this case, however, the value of θ^* is not known a priori and must be determined as part of the solution.
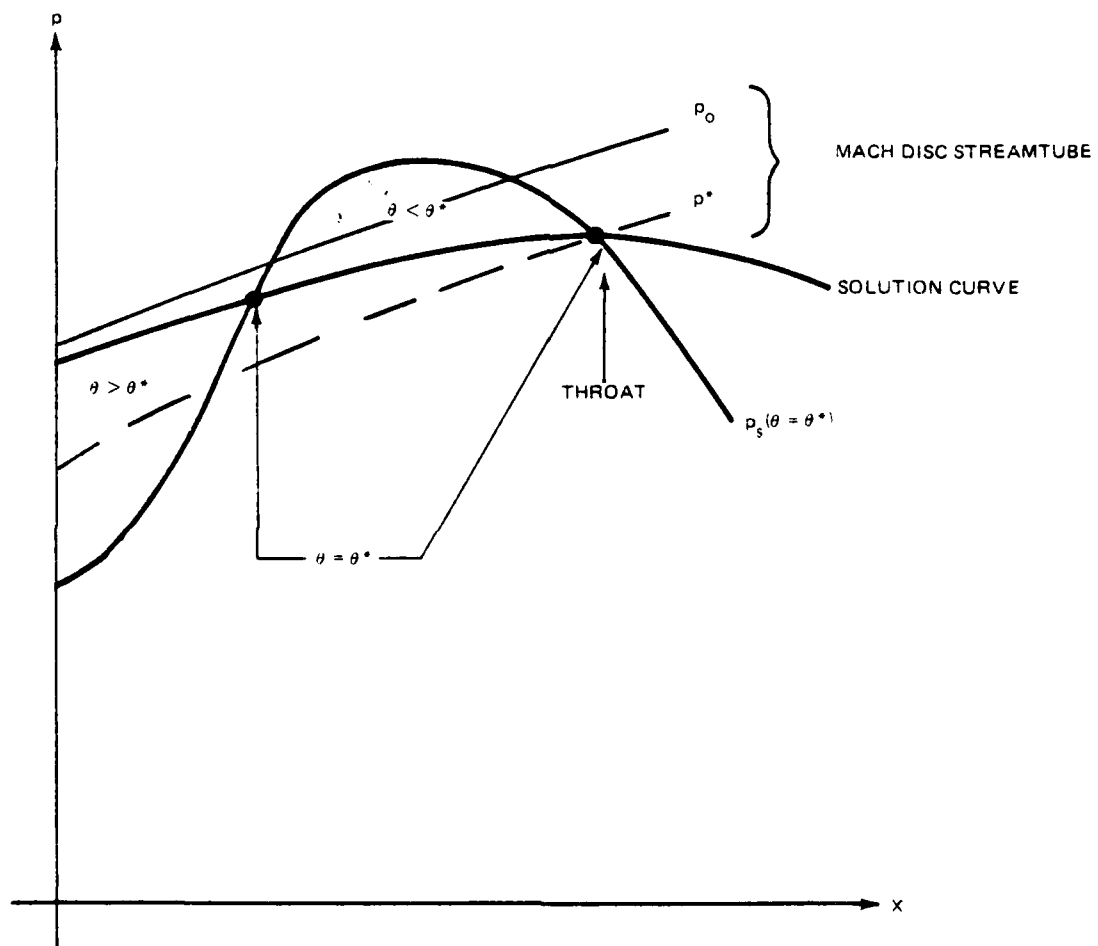
Fig. 8-5 Solution Curve for Viscous Mach Disc Flow

2193-059D

The numerical integration procedure for the solution of the interaction equation is based on integrating the equation (8-6) backward starting at the sonic throat. Several integration schemes have been employed with virtually equal success. The numerical integration procedure for the inviscid case is outlined first. The extension to the viscous case follows naturally and is detailed at the end of this chapter. The starting solutions at the throat are derived and their numerical implementation is discussed. The solution proceeds using the following sequence of steps:

(In the followng discussion superscript (i) denotes iteration number and $y^{(i)}$ denotes the subsonic streamtube height computed as a result of the estimated value by $y^{(i)}$.)

1) Compute y^* and estimate $M^{(1)}$, $y^{(1)}$

2) Determine the location of the throat x^* and the flow gradients there.

3) Solve the interaction equation for θ (x) by integrating backwards from the point x^*, y^* where $\theta = 0$

4) Determine $Y^{(i)}$ by integrating the above solution for θ .

5) Combine the estimated values of $y^{(i)}$ and the computed values of $Y^{(i)}$ to achieve the next estimate for the Mach disc streamtube $y^{(i+1)}$

6) Repeat the steps (3) - (5) until the solution converges.

The details for each step are outlined in the following paragraphs.

Step 2   The solution of the interaction equations has a classical saddle point singularity at the sonic throat. This can be verified by assuming that the Mach number in the neighborhood of the throat is given by $M^2 = 1 + a (x - x^*)$ and investigating the nature of the interaction equation near $x = x^*$.

Considering the relationship between pressure and Mach number for the Mach disc flow

$$\frac{1}{EM^2}\frac{dM^2}{dx} = \frac{-2}{\gamma M^2}\frac{1}{p}\frac{dp}{dx}$$

$$E = 1 + \frac{\gamma-1}{2}M^2$$

Substitute $M^2 = 1 + a\,(x - x^*)$, $\quad \frac{1}{p}\frac{dp}{dx} = (\theta' - f')/h(m)\quad$ and $\theta = b(x - x^*)$ to get a relationship between the Mach number gradient a and the dividing streamline angle gradient b.

$$b = -\frac{\gamma}{\gamma+1}h^*\,a + f'^*$$

In order to be self consistant the subsonic flow must also satisfy the one dimensional Mach number area relationship

$$\frac{1-M^2}{EM^2}\frac{dM^2}{dx} = -\frac{2}{A}\frac{dA}{dx} = \frac{-4\theta}{y}$$

Again using the expansions for M and θ near the throat a second relationship between a and b can be derived

$$\frac{a^2 y^*}{\gamma+1} = 2b$$

Combining these two relationships results in a single quadratic equation

$$a^2 y^* + a\,(2\gamma h^*) = 2\,(\gamma + 1)\,f'^*$$

Step 3 The interaction equation (8-6) is integrated from one node point to the next. The value of the function B is assumed known from a previous iteration step. If i denotes the iteration step and x_j is the value of x for mesh point j

$$\theta' - f' + B\theta = 0$$

$$\theta^{i+1}_{j+1} - \theta^{i+1}_{j} - (f_{j+1} - f_j) + \int_{x_j}^{x_{j+1}} B^i \theta^i dx = 0$$

$$(8-12)$$

The evaluation of the integral in equation (B-12) was achieved by either of two methods both of which are given below. In method 1 the trapezoidal rule is employed resulting in

$$\theta_j^{i+1} = \frac{\theta_{j+1}^{i+1}\,(1 + B_{j+1}^i\,\Delta x/2) - (f_{j+1} - f_j)}{(1 - B_j^i\,\Delta x/2)}$$

In the second method it is assumed that the function B has a singular behavior as follows

$$B(x) = \frac{B^*}{x^* - x} + \hat{B}(x)$$

where B^* is a constant which characterizes the singularity at x^*. This results in an integration formula

$$\theta_j^{i+1} = \frac{\theta_{j+1}^{i+1}\left[1 + \alpha B^{*i} + \hat{B}_{j+1}^i\,\Delta x/2\right] - (f_{j+1} - f_j)}{1 - \beta B^{*i} - \hat{B}_j^i\,\Delta x/2}$$

where

$$\alpha = (x^* - x_j)/(x_{j+1} - x_j)\,\ell n\left[(x^* - x_j)/(x^* - x_{j+1})\right] - 1$$

$$\beta = 1 - (x^* - x_{j-1})/(x_{j+1} - x_j)\,\ell n\left[(x^* - x_j)/(x_{j+1} - x_j)\right]$$

Step 4 A simple trapezoidal integration formula is used to integrate backwards the point $x = x^*$, $y = y^*$ using the solution for θ.

$$\frac{dy}{dx} = \tan\theta \approx \theta$$

$$y = y^* + \int_{x^*}^x \theta\,dx$$

Denoting the value by Y

$$Y_j^{i+1} = Y_{j+1}^{i+1} - (\theta_{j+1}^{i+1} + \theta_j^{i+1})\,(x_{j+1} - x_j)/2$$

Step 5 Based on the new value of θ_j^{i+1} at each mesh point an updated value for the Mach number on the supersonic side of the dividing streamline can be computed by inverting ψ_j^{i+1} for m_j^{i+1} using

$$\psi_j^{i+1} = \phi_j - \theta_j^{i+1}$$

Using this Mach number and the total pressure of the outer (supersonic) stream an updated value of static pressure can be computed. Combining this pressure and the total pressure of the subsonic streamtube at each point with the Mach number pressure relationship yields

$$\overline{M}_j^{i+1} = \left\{ \frac{2}{\gamma-1} \left[(p_o/p)^{\frac{\gamma-1}{\gamma}} - 1 \right] \right\}^{\frac{1}{2}}$$

Based on the computed value Y_j^{i+1} and the known value of y^* for the subsonic streamtube another estimate of the subsonic streamtube Mach number is computed

$$\widehat{M}_j^{i+1} = F (Y_j^{i+1}/y^*)$$

where the function F is used symbolically to denote the inverse of the Mach number - A/A^* relationship. (This equation is actually solved by a simple iteration.) Finally a new value of M is determined by combining the estimates $\overline{M}$ and $\widehat{M}$ using the underrelaxation formula

$$M_j^{i+1} = .25 \, \widehat{M}_j^{i+1} + .75 \, (M_j^i + \overline{M}_j^i)/2$$

The solution for the viscous case proceeds in exactly the same manner as outlined above for the inviscid streamtube case with the following modifications. The initial location of the sonic point cannot be made because the sonic throat angle θ^* is given by the formula

$$\theta^* = \gamma \widehat{f}^*/2$$

Since $\widehat{f}^*$ depends on the solution an initial estimate of the viscous solution is necessary to determine x^*. The equation for stagnation pressure p_o of the inner streamtube is achieved by straightforward integration, again based on the current iterate value of $\sigma_1 (x)$. In the inversion to determine $\widehat{M}_j^{i+1}$ the value of y^* must be computed for each station using the relationship $p_o A^* = $ constant for the inner flow .

Two test cases were employed to determine if the theory and computer code were operating satisfactorily. The first test case consisted of a known exact solution (inviscid) which the program was required to reproduce. The second test case was an actual Mach disc flow with substantial mixing effects. In the first case the computer code and theory reproduced the exact solution to a very close tolerance. In the second case, the code was used to analyze the flow pattern and achieved very good agreement with all reported measured quantities. However, the experimental results reported in Reference (8-4) were not complete enough to allow prediction of the Mach disc location.

The first test case was devised by prescribing a subsonic streamtube given by the equation

$$y = 1.36 + .36 \cos (.59169x - 2.1664) \tag{8-13}$$

which is shown in Figure 8-6. The streamtube is assumed to choked at the throat where $y = 1.0$ the Mach number is unity. Using isentropic flow tables the Mach number distribution and pressure distribution in the streamtube were computed . The compatible outer supersonic flow is constructed as follows. A total pressure ratio (outer supersonic stream to inner subsonic stream) $p_{o2}/p_{o1} = 14.403$ was chosen. The outer static pressure is set equal to the inner subsonic streamtube pressure. The pressure and total pressure is known at each point on the slip line so that the Mach number can be computed $(m(x))$. The local slope of the streamtube

$$\theta = y' \quad = -.21301 \sin (.59169x - 2.1664)$$

is computed at each point and thus the function $f(x) = \theta + \nu$ can be computed on the supersonic side of the slip line. The Prandlt Meyer function ν is only a function of m and is computed at each point. This construction has defined a subsonic streamtube with a consistant value of $\theta + \nu$ resulting in matched pressure on the dividing streamline.

$$y = 1.36 + .36 \cos (.59169x - 2.166)$$
$$y' = -.21301 \sin (.59169x - 2.1664)$$
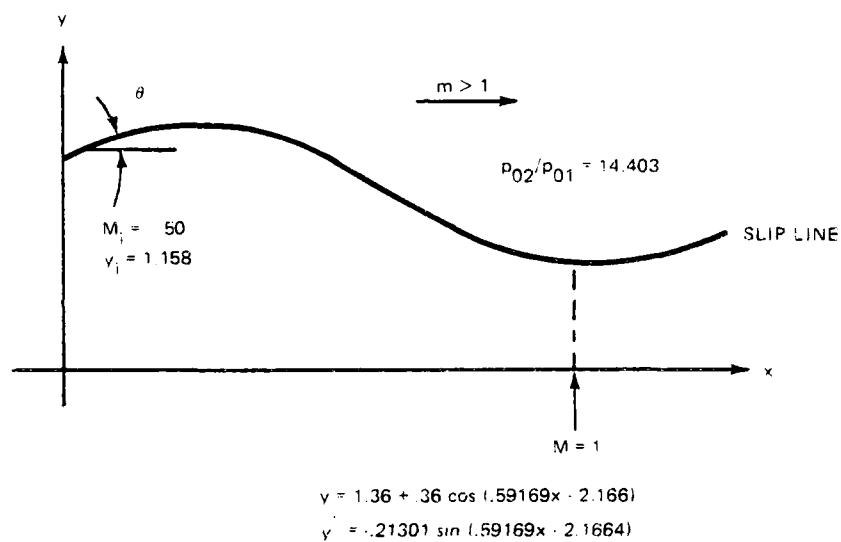
Fig. 8-6 Geometry of Subsonic Streamtube for Test Calculation

Based on the following input f(x), p_{o2}/p_{o1} = 14.403, m(x = 0) = .5, y (x = 0) = 1.158 the computer code is used to predict the slip line height y(x). If the program is working properly it should reproduce the streamtube given by equation (8-13). The computed solution can then be compared with the original equation to determine the accuracy and efficiency of the computer code. Tables 1 and 2 summarize these comparisons. Table 1 compares the exact original geometry and the computed numerical results. Columns three and four are the errors in the streamtube height and slope respectively. This calculation employed forty iterations and used method 2 for the integration scheme. The errors are at most 2 x 10^{-3} which is entirely acceptable in this case. (The function f(x) was only input to three decimal places.) For this calculation the pressure on the subsonic and supersonic side of the slip line are compared in Table 2. Column one is the accumulated difference (sum of the absolute values) in pressure difference along the slip surface. The total accumulated error is .0073 for the entire 37 points of the calculation. Thus on the average the difference in pressure at each mesh point is approximately .0002. This is well within the expected calculation accuracy.

The convergence of the solution is shown in Figure 8-7, where the Mach number of the subsonic streamtube is plotted for the iterations 1,2,3,5 and 10. Iteration 1 is the starting solution which in this case was chosen to be M = .25 everywhere but in the vicinity of the throat where the local throat solution was employed to get a good first approximation. The relaxation procedure showed very good properties in this case. The successive estimates for Mach number proceeds smoothly (but not monotonically) toward the final

Table 1 Comparison of Numerical Calculation and Exact Solution

J	x	$y - y_{exact}$ $\times 10^2$	$y' - y'_{exact}$ $\times 10^2$	y_{exact}	y'_{exact}
1	.00	-.0949	-.0176	1.158037	.17633
2	.25	-.0985	.0564	1.204165	.19202
3	.50	-.0648	.2847	1.253695	.20351
4	.75	-.0493	-.0842	1.305549	.21056
5	1.00	-.0706	-.0096	1.358591	.21301
6	1.25	-.1015	-.1594	1.411664	.21080
7	1.50	-.1082	.1811	1.463609	.20400
8	1.75	-.1058	-.0888	1.513290	.19273
9	2.00	-.1107	.1167	1.559624	.17726
10	2.25	-.1322	-.2269	1.601598	.15792
11	2.50	-.1741	-.0551	1.638295	.13512
12	2.75	-.1880	-.0112	1.668913	.10938
13	3.00	-.1873	.0519	1.692785	.08125
14	3.25	-.1744	.0754	1.709388	.05134
15	3.50	-.1546	.0955	1.718360	.02031
16	3.75	-.1373	.0452	1.719505	-.01116
17	4.00	-.1234	.0559	1.712798	-.04239
18	4.25	-.1065	.0588	1.698386	-.07270
19	4.50	-.0968	-.0139	1.676582	-.10141
20	4.75	-.0969	-.0273	1.647865	-.12791
21	5.00	-.1112	-.1430	1.612859	-.15162
22	5.25	-.0992	.1835	1.572332	-.17201
23	5.50	-.0679	.0013	1.527166	-.18865
24	5.75	-.0381	.1653	1.478350	-.20117
25	6.00	-.0160	-.0631	1.426948	-.20929
26	6.25	-.0036	.0819	1.374085	-.21285
27	6.50	.0274	.0859	1.320913	-.21175
28	6.75	.0502	.0201	1.268596	-.20603
29	7.00	.0459	-.1282	1.218274	-.19581
30	7.25	.0176	-.1674	1.171049	-.18131
31	7.50	.0186	.1129	1.127950	-.16285
32	7.75	.0556	.1274	1.089919	-.14084
33	8.00	.0614	-.1276	1.057787	-.11575
34	8.25	.0619	.0942	1.032257	-.08813
35	8.50	.0692	-.0625	1.013884	-.05859
36	8.75	.0565	-.0553	1.003071	-.02776
37	9.00	.0397	-.0854	1.000053	-.00367

Table 2 Comparison of Pressures on Either Side of the Slip Surface

| J	$\sum_{i=1}^{J} \Delta p \times 10^2$	$p_{subsonic}$	$p_{supersonic}$
1	.0145	.842616	.842761
2	.0324	.870053	.870231
3	.0522	.892628	.892827
4	.0748	.910797	.911023
5	.0983	.925232	.925472
6	.1223	.936721	.936962
7	.1462	.945849	.946088
8	.1700	.953059	.953297
9	.1932	.958691	.958923
10	.2162	.963049	.963279
11	.2388	.966365	.966590
12	.2610	.968865	.969087
13	.2829	.970659	.970878
14	.3045	.971839	.972055
15	.3259	.972460	.972674
16	.3472	.972546	.972760
17	.3686	.972106	.972320
18	.3903	.971118	.971335
19	.4124	.969525	.969746
20	.4347	.967241	.967464
21	.4573	.964141	.964367
22	.4808	.960097	.960331
23	.5046	.954893	.955131
24	.5286	.948238	.948479
25	.5526	.939761	.940001
26	.5764	.929029	.929268
27	.5993	.915578	.915807
28	.6206	.898747	.898960
29	.6393	.877762	.877949
30	.6545	.851860	.852012
31	.6673	.820728	.820857
32	.6765	.784111	.784203
33	.6777	.741203	.741215
34	.6791	.692629	.692642
35	.6874	.639292	.639209
36	.7033	.581848	.581689
37	.7279	.522517	.522270
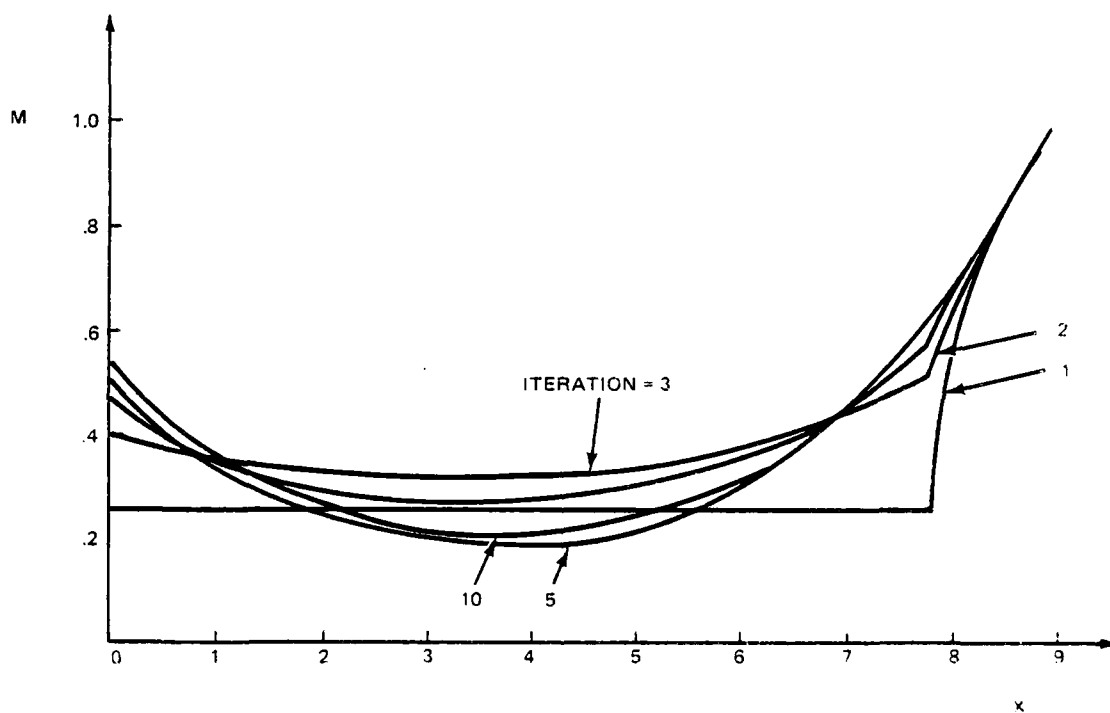
Fig. 8-7 Convergence of Mach Numbers for Inviscid Test Case

result which are shown in Figure 8-8. In this particular example the function f actually has a slight increase near x = 0 which is reflected in the initial increase in slope of the slip line ($\theta'(0) > 0$). Mach number decreases from its initial value of .5 to .2 at x = 4 with the associated increase in pressure to near stagnation pressure. In this region of very low Mach number the subsonic streamtube behaves very much like a constant pressure boundary. In mathematical terms the function B in the interaction equation is very small and to a good approximation the interaction equation reduces to $\theta - f' = 0$ with the solution

$$\theta = f - f(\theta = 0)$$

This property is displayed graphically in Figure 8-9 where θ and the difference $f - f(\theta=0)$ are plotted. In this type of flow the central role of the function f is very clear. Only near the sonic throat where B is order unity does the solution for θ differ markedly from $f - f(\theta = 0)$

The second test case employed the flow field in a supersonic diffuser as reported in Ref. 8-4. The geometry of the flow is shown in Figure 8-10. An incident shock approaches the diffuser axis. At z = 0 a Mach disc is formed at the intersection of the reflected and incident shock waves. There is a mixing layer between the supersonic stream and the flow which passed through the Mach disc (normal shock). In the mixing layer the flow Mach number smoothly passes from subsonic to supersonic. Therefore, the sonic line appears to eminate from the triple point and move almost horizontally at first before curving
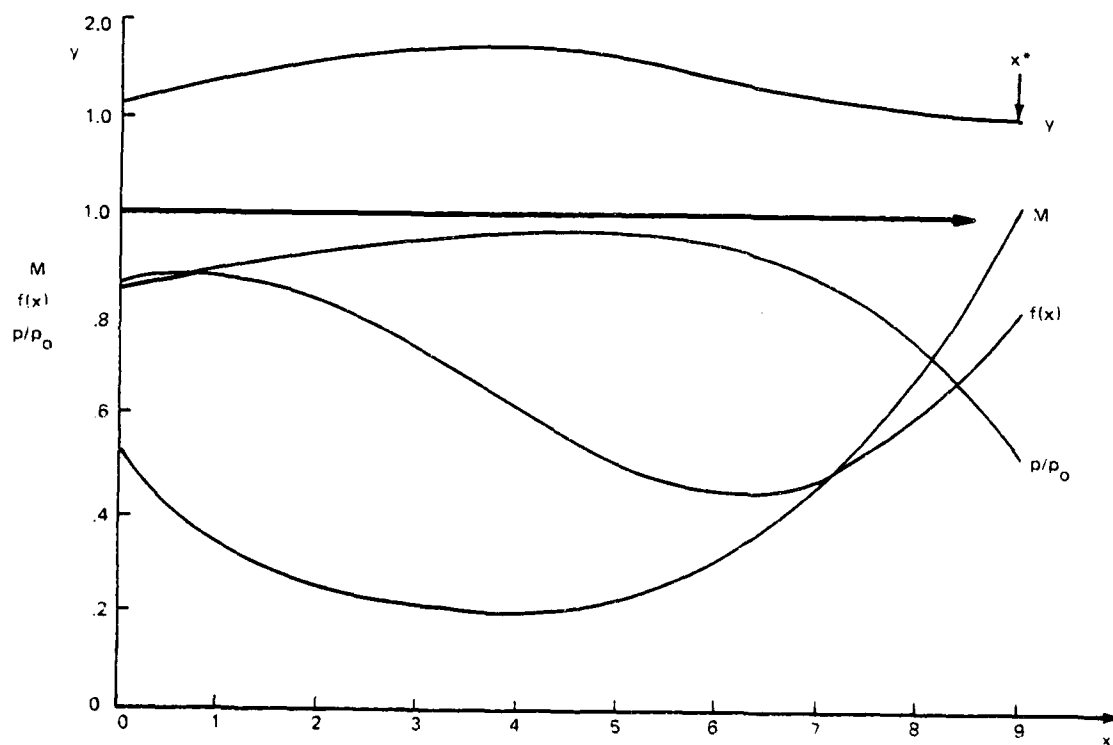
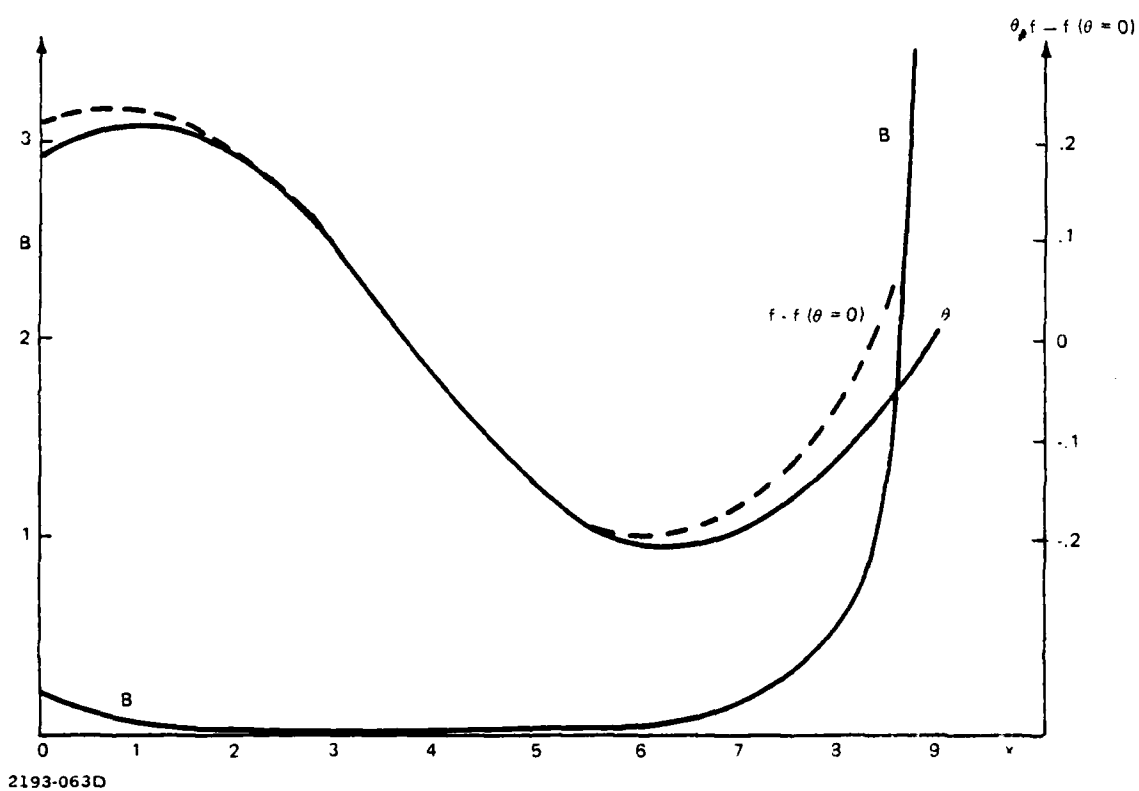Fig. 8-8 Solution Curves for Inviscid Test Case

2193-063D

Fig. 8-9 Solution Curve for the Coefficient B in the Interaction Equation and
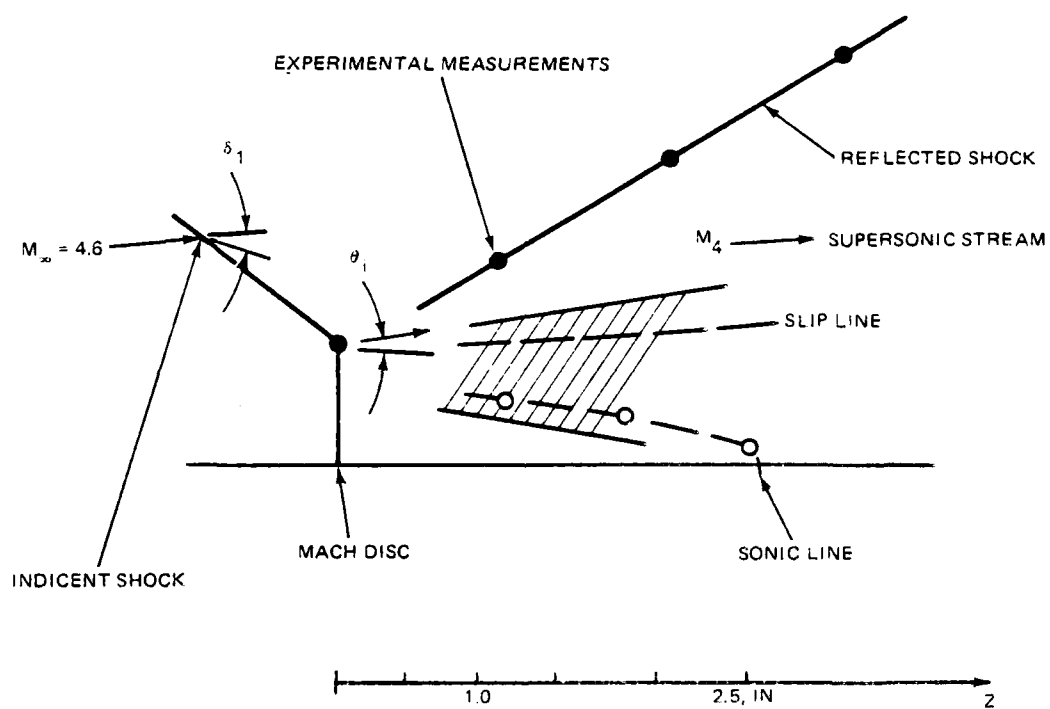Comparison of Solution and Approximate Function

Fig. 8-10 Flow Field for Test Case 2 · Viscous Mach Disc

downward and intersecting the axis. Reference 8-4 reports the profiles of
Mach number, total pressure and impact pressure at six stations downstream of
the shock triple point. Only the first three stations are relevant to this
study because the inner streamtube is supersonic downstream of these. It is
important to note that the exact location and size of the Mach disc were not
measured in the experiment and that the closest station to the triple point is
at $z = .5$ inches. It is pointed at in reference 8-4 that no attempt was made
to probe the exact for orientation of the shock configuration in the vicinity
of the triple point where the shock may be curved.

This flow field was studied using the present analysis as follows. Since
the details of the upstream flow field are unknown not enough information is
presented to attempt an a priori computation of the Mach disc location and
height. It is possible, however, to determine if the computer code gives
results consistant with various aspects of the experiment. In order to do this
the function $f(x) = \theta + \nu$ was computed using the experimentally observed
values for the Mach number on the supersonic side of the slip line and the
reported slip line geometry. From the published results the value of the
streamline slope was taken to be approximately zero. This was all possible
downstream of the first measured station which was at $z = .5$ inches. The
properties at the triple point and its precise location were not presented in
the reference. The triple point solution was constructed subject to the
constraint that the pressure downstream was given by the normal shock pressure
($M = 4.60$ upstream). This renders the Mach disc calculation a function of
only a single parameter - the deflection across the incident shock, for
example. It was determined that the Mach number M_4 (see Fig. 8-10)

8-29

downstream of the triple point (supersonic) was only a weak function of the initial deflection angle (δ_1) and equal to 1.89 which is entirely consistent with the experimental results. The initial flow angle downstream of the triple point (θ_i see Fig. 8-10) is a strong function of δ_1. Since the flow field is expanding downstream of the triple point the initial angle must be negative. The value θ_i was prescribed to be -3.5° and the solutions were not found to be inconsistant with this value.

With function f constructed above, the value of p_{02}/p_{01} based on the triple point solution and an estimated initial height of the Mach disc a series of solutions was computed. Only one series of computations are detailed here. Three values of the friction factor constant were employed -.01, -.005 and 0 (the inviscid case). Figure 8-11 shows the computed slip line location with two experimentally measured Mach number profiles together with the result of the computations for the one dimensional results. It is important to note that the slips line location quoted in reference 8-4, denoted by S are far outside of an estimate based on the Mach number profile. It is believed that this occurred because the authors extrapolated the stream-lines back to a triple point location they estimated based on a straight transmitted shock from z = .5 back to z = 0. In the present calculation the initial height of the Mach disc was chosen so that the slip line passed approximately through the center of the mixing layer (based on Mach number profile) at the z = .5 station. At both stations the one dimensional values of Mach number are reasonable averages of the measured profiles. Note that the one dimensional values have gone supersonic at the second station.
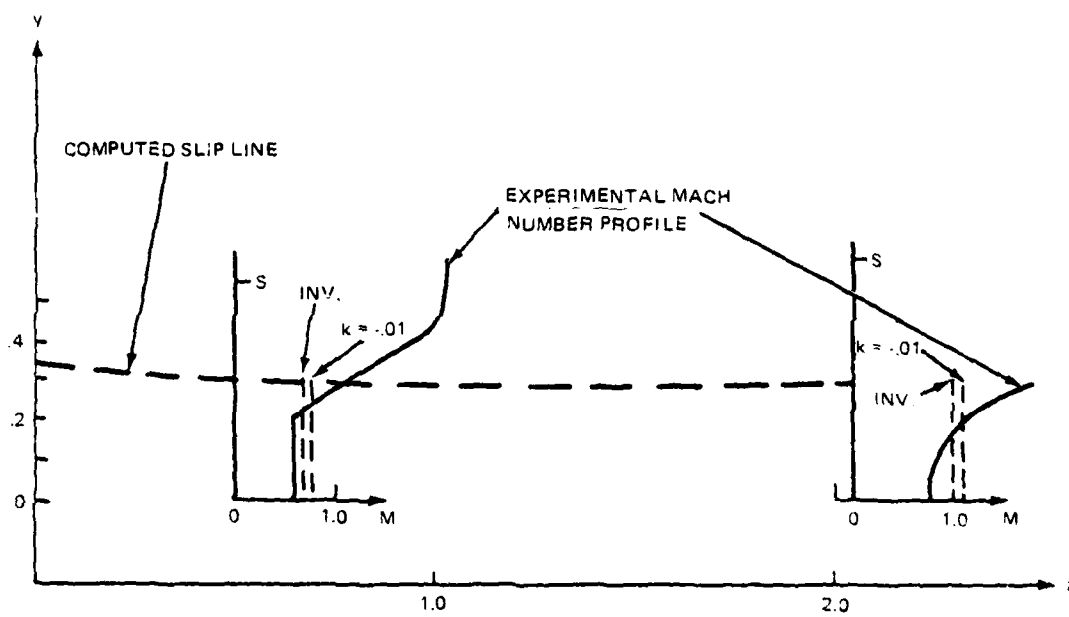
Fig. 8-11 Viscous Test Case - Computed Slip Line and Mach Numbers

Figure 8-12 presents the computed slip line location for the three cases and the Mach number calculations along with the experimental centerline values. The effect of viscosity is to move the throat upstream closer to the Mach disc. This is expected because mixing in these cases increase the average total pressure of the subsonic stream which increases the Mach numbers (by decreasing the local value of p/p_0). The experimental sonic line is shown in the figure. It is not possible from these results to conclude which value of friction factor is most appropriate. The measured centerline Mach numbers are below the calculated values in all cases which is to be expected based on the upward curvature of the dividing streamline .

Figure 8-13 shows the total pressure distribution for the three cases. The total pressure increment at the sonic point is 13 % and 8 % for the cases with friction constants k = -.005 and -.01 respectively. In this case the effect of mixing does not have a dramatic effect on the geometry of the flow field (Fig. 8-12). Friction moves the sonic point a noticeable amount, however, by far the largest force on the flow is the static pressure gradient. These conclusions cannot be carried over to the Mach disc in a plume because in that case the initial pressure gradient is compressive behind the Mach disc (f(x) decreases). Therefore, the static pressure gradient tends to decelerate the flow in opposition to the total pressure gradient which is driving Mach number in the opposite direction.
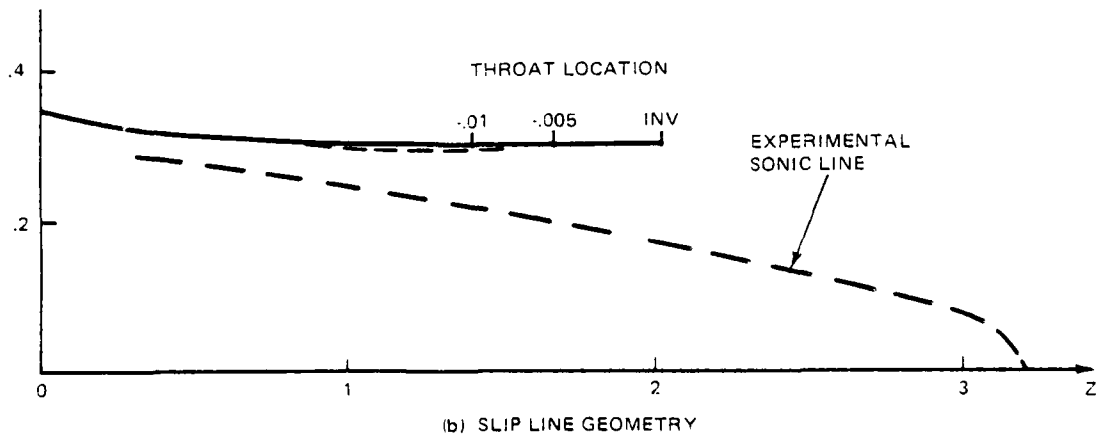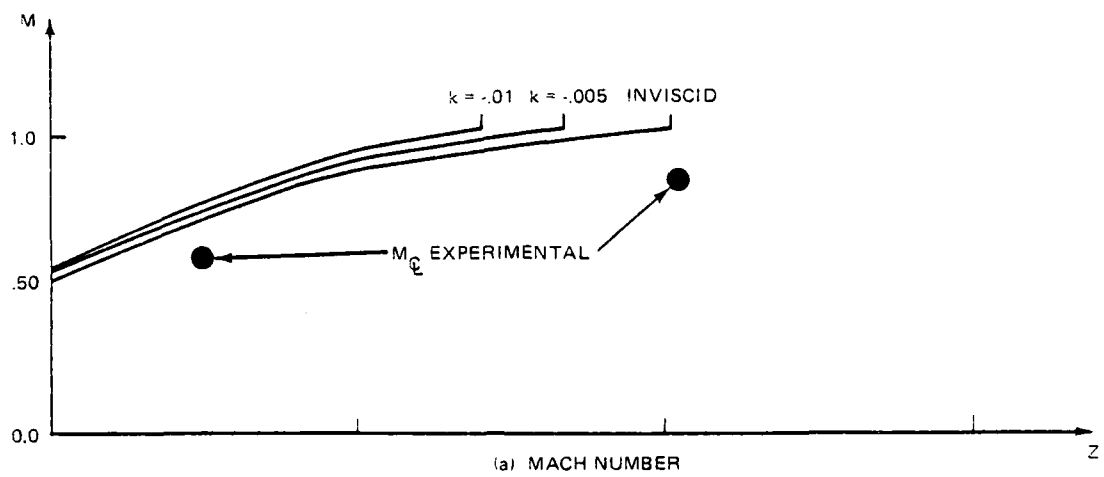
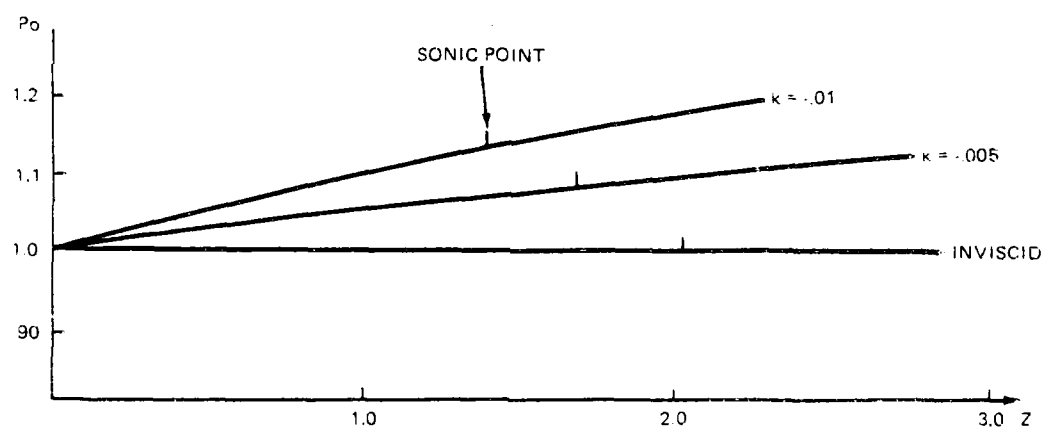Fig. 8-12 Comparison of Computed Results for Various Friction Factors

Fig. 8-13 Total Pressure Distribution for Various Friction Factors

NOTES FOR VISCOUS SOLUTIONS:

Throat solution - the Mach number gradient a at the throat is given by solving the equation

$$a^2(y\star) + a(2\gamma h\star - (\gamma+1)\gamma\hat{f}\star) = 2(\gamma+1)f'\star - \gamma(\gamma+1)\hat{f}'\star + 2\gamma(\gamma+1)\hat{f}\star h\star/y\star$$

The slope gradient b is then

$$b = f'\star - \gamma h\star a/(\gamma+1) + \gamma h\star\hat{f}\star/y\star$$

and the throat angle is

$$\theta\star = \gamma f\star$$

The friction factor $\hat{f}$ is related to the inner and outer Mach numbers by

$$M^2\hat{f} = 2k\left(\frac{T_o}{T_{ref}}\right)\left[\frac{m}{\sqrt{1 + \frac{-1}{2}m^2}} - \frac{M}{\sqrt{1 + \frac{-1}{2}M^2}}\right]^2$$

where $\hat{f} = 2\tau/\rho v^2$ and k and T_{ref} are parameters in the eddy viscosity formula for the shear layer.

REFERENCES

8-1 Abbett, M., "The Mach Disc in Underexpanded Exhaust Plumes,"
AIAA Paper No. 70-231, Jan. 1970.

8-2 Salas, M., "The Numerical Calculation of Inviscid Plume FLow
Fields, "AIAA 7th Fluid and Plasma Dynamics Conference, AIAA
Paper No. 74-323, June 17-19, 1974.

8-3 Shapiro, A.H. The Dynamics and Theromdynamics of Compressible
Fluid Flow, Ronald Press Co., N.Y. 1953.

8-4 Back, L.H. and Cuffell, R.F., "Viscous Slipstream Flow
Downstream of a Centerline Mach Reflection", AIAA Journal Vol 9
No. 10, Oct. 1971.

SECTION 9

CONCLUSIONS

The optical signature and thermochemical properties of rocket exhaust plumes are sensitive functions of the many parameters determining the plume flow field. The influence of the many inputs bearing on the plume signature is basically through the temperature and species fields. The plume is a hot mass of gas composed of a variety of optically active species. The precise determination of the optical signature is based on accurate fluid mechanical predictions leading to spatially resolved temperature, pressure and species concentration fields. Both chemical kinetic and radiative transport processes are driven by source or rate terms which are of the Arrenhius type. Therefore, the IR signature is very sensitive to temperature and this sensitivity increases as the level of plume temperature decreases. A model plume has been analyzed based on mathematical analysis taking advantage of this mathematical property. The direct quantitative relationship between temperature field and species field and local station radiation has been shown.

In the general case of multinozzle rocket plume flow fields the inviscid pattern is a complex three dimmensional flow containing several shock wave surfaces. The shock waves produce both near and far field temperature increases and so are central to (chemical activity and) optical signature predictions. While the shock wave structure is not the only fluid dynamic process involved in determining the temperature distribution it is involved in inviscid flow field calculation which is the primary skeleton on which is built the total flow field picture. Accurate prediction of the shock wave structure can be achieved only through detailed calculations which track the

shock surfaces. Methods which "capture" the shock waves would require machine memories and computer times which are far beyond what is presently available. A floating three dimensional "fitted shock" computer code was develped for the first time, which was capable of predicting a flow with a single shock surface. The program also tracked the singularity that occurs at the point where the impingement shock intersects the plume boundary. The floating shock program became far to complex to program for the case where there are more than a single shock and several triple points in the flow. A different approach was investigated which does not explicitly track the discontinuites. The idea was demonstrated on one dimensional unsteady flow to trace entropy discontinuities. This method in a simple way tracks a slip surface using a single grid point, where a "capturing method" smears the discontinuity over 10-15 grid points. The extension of these ideas to three dimensional flows is a project for the future.

Theoretical development of the quantitative description of three dimensional flows with interesection shock surfaces was achieved. The intersection of two three shock surfaces leads to a complex process. The resulting shock pattern depends not only on the strength of the two shock waves but also on their relative orientation. The study showed how a local analysis at the shock intersection line could be used to explain the shock transmission/ reflection configuration at the intersection line. The image of this intersection process in the hodograph plane (pressure/deflection) explains the requirement for transition from a regular reflection process to a Mach reflection process.

The flow field associated with the axisymmetric plume with a Mach disc has been analyzed using a new iteration scheme. The heart of this approach is the integration of the governing interaction equation starting from the sonic station and proceding upstream. This analysis which leads to the underlying interaction equation provides theoretical insight for the first time into the mechanisms governing the Mach disc location. The analysis also includes viscous mixing effects which have not as yet been studied in past investigations. The integration of this program with the SPF plume code is a project that should be undertaken in the future.

Future capabilities in prediction of three dimensional supersonic flows as complex as multinozzle exhaust will increase as both new algorithms are developed and computer capabilites increase. Algorithm development must be pursued to reduce the enormous computer logic necessary to track complex intersecting shock patterns. Significant computer speed and size developments could relax the requirements and alter the shape of the new algorithms. There is a great amount of work necessary in the fundamental understanding of three dimensional flows. There are a variety of complex conical processes such as the the transition of the shock intersection from regular to irregular and the shock lift off problem that must be studied, understood and cataloged in order to make progress and achieve prediction capabilities in complex three dimensional supersonic flows. These unit solutions are the three dimensional counter parts of the familiar two dimensional wedge shock solution and two dimensional Prandtl Meyer solutions that are used extensively as building blocks and initial conditions in two dimensional problems.

SECTION 10

PUBLICATIONS AND PRESENTATIONS

"Multinozzle Plume Flow Fields - Structure and Numerical Calculations", AIAA 10th Fluid and Plasma Dynamics Conference June 27-29, Paper No. 77-710.

"Three Dimensional Shock Wave Interactions" 17th Aerospace Sciences Meeting, Jan. 1979, Paper No. 79-0137.

"Critical Requirements for Mid Altitude IR Predictions", 11th JANNAF Plume Technology Meeting, May 1979.

"Multinozzle Plume Flow Fields - Structure and Modelling" 10th JANNAF Plume Physics Meeting, Sept. 1977.

"Intersection of Three-Dimensional Shock Surfaces" Paper BD3 31st Meeting of the American Physical Society (Division of Fluid Mechanics) Nov. 1978.

"A New Analysis for Mach Disc Calculations" (in preparation)